Title
Electronic excitations, phonons, and electron-phonon coupling in acenes

Author
Brown-Altvater, Florian

Publication Date
2019

Peer reviewed|Thesis/dissertation

Electronic excitations, phonons, and electron-phonon coupling in acenes

by

Florian Brown-Altvater

A dissertation submitted in partial satisfaction of the

requirements for the degree of

Doctor of Philosophy

in

Chemistry

in the

Graduate Division

of the

University of California, Berkeley

Committee in charge:

Professor Jeffrey B. Neaton, Co-chair
Professor Phillip L. Geissler, Co-chair
Professor Martin Head-Gordon
Professor Steven G. Louie

Summer 2019

Electronic excitations, phonons, and electron-phonon coupling in acenes

Abstract

Electronic excitations, phonons, and electron-phonon coupling in acenes

by

Florian Brown-Altvater

Doctor of Philosophy in Chemistry

University of California, Berkeley

Professor Jeffrey B. Neaton, Co-chair

Professor Phillip L. Geissler, Co-chair

In this dissertation, we present first principles electronic structure calculations of acene solids, achieving better understanding of their electronic and vibrational properties relevant to their optoelectronic function. The family of acene molecular crystals serves as a testbed for broader classes of organic crystalline semiconductors, which have come under increasing focus for their many favorable optoelectronic properties. Among them are relative ease of processing, strong and tunable absorption, and charge carrier mobilities sufficiently high for applications. Despite numerous computational and experimental efforts, the details of the underlying mechanisms of these optoelectronic processes are still actively disputed, especially concerning the role of electron-phonon coupling and its impact on the acene electric structure at finite temperatures. To further improve the efficiency of these systems, and to develop new materials that can overcome existing challenges, better understanding of the underlying principles and structure-function relationships that determine acene properties is thus needed.

Here, we calculate the charged and neutral electronic excitations of the acene crystal series within many-body perturbation theory (MBPT), based on van der Waals (vdW)–corrected density functional theory (DFT). We compare the performance of various functionals and vdW corrections in predicting the experimental lattice parameters and investigate the sensitivity of excited states to these structural parameters. Generally, low-lying charged and neutral excitations are well described by the MBPT methods used here, provided that optimized geometries close to experiment are used. The inclusion of vdW interactions to account for the weak intermolecular interactions in molecular crystals is thus found to be a prerequisite for the predictive and accurate calculation of excited state energies in these systems.

To investigate the effect of vibrational coupling at zero and finite temperatures in organic crystals, we calculate the phonon band structure and electron-phonon contributions to the electron self-energy for the case of the naphthalene crystal. We first provide a comprehensive analysis of the computed phonon band structure, comparing to neutron diffraction data. Again, vdW corrections are necessary to obtain phonon frequencies from DFT calcu-

lations that are in good agreement with experiment. Based on these results, we compute the electron-phonon self-energy in naphthalene using vdW-corrected DFT and MBPT to lowest order. This self-energy provides the contribution of phonons to the renormalization of band structure energies and to the scattering lifetimes of electronic states. The resulting renormalized band gap at room temperature, and the temperature-dependent mobilities of electron and hole charge carriers are in good agreement with experimental values. Finally, we explore an eigenvalue–self-consistent computational scheme for the electron-phonon self-energy that leads to the prediction of strong satellite bands in the quasiparticle band structure.

The methods presented in this dissertation are general and our conclusions are applicable to other molecular crystals, thus providing a template for future predictive calculations of optoelectronic properties of acenes and related systems, in which both structures and excited states are calculated entirely from first principles.

To my friend, partner, and love Cait.

Contents

List of Figures

List of Tables

Acknowledgments

This dissertation is the work of many, both aiding me with research questions and expanding my scientific horizon, and lending emotional support and sharing their lifes with me.

First and foremost my thanks go to Prof. Jeff Neaton, who infected me with his unbridled enthusiasm and optimism throughout these years. Thank you for your continuous support, especially when things got rough and slow; and for always taking time and being present in our meetings. Our conversations and discussions gave me the confidence and (bi-)weekly motivational boost that kept me going to the end. I am a better chem... ahem ... scientist because of you.

To Sahar Sharifzadeh (Chapter 3), Tonatiuh Rangel (Chapters 3 and 4), and Gabriel Antonius (Chapter 5), the postdocs that took me under their wings, for showing me the ropes, and pushing me out of my comfort zone. Thank you for always having an open ear, trying to teach me all you know, and for providing role models worth striving for. To my collaborators, Kristian Berland, Kyuho Lee, Per Hyldgaard, and Leeor Kronik (Chapter 3), Matteo Giantomassi, Claudia Draxl, Xavier Gonze, and Steven G. Louie (Chapter 5).

This work was supported in part by the US Department of Energy, Office of Basic Energy Sciences and of Advanced Scientific Computing Research through the SciDAC Program on Excited State Phenomena, and by the Chemical Sciences, Geosciences, and Biosciences Division in the Office of Basic Energy Sciences of the US Department of Energy. Computational resources were provided by the National Energy Research Scientific Computing Center, which is supported by the Office of Science of the US Department of Energy. Portions of this work took place at the Molecular Foundry, supported by the US Department of Energy, Office of Basic Energy Sciences.

To Samia and Michelle, for your friendship and support. Being an OG wasn't always easy, but at least it was fun being in it with you. You took me in as your co-conspirator despite my German quirks, made me feel like I belonged here, and helped put things in perspective, such as life or homework. To Stephanie for the unconditional and boundless happiness (and mischief) you radiate wherever you go. Science, and the rest of the world, is a brighter place because of you. To Jonah for countless red-couch-sessions. Equations always seemed less scary with you around. To all Neatonians, current and former, for creating such a welcoming, supportive family across group generations. To Meg, Marisa, and Arica, for your infinite patience. You are the solid rocks in the troubled waters of academia. And to the happy-hour-squad, for the many team-building opportunities (#TeamNeaton). To Michelle Douskey and the GSI Teaching and Resource Center for making me a better teacher.

Vielen Dank an Einsche, Flo, Luise, Jörg, Silke und Basti für eure langjährige Freundschaft, und eure Großzügigkeit meinem Humor und anderen Schwachstellen gegenüber. To all upstairs neighbors, especially Anand, Jacob, Anaïs, Julia, Tony, Valkyrie, and Evan, for your friendship, heavenly dinners, and general merriment. To the cast and crew of Critical Role, the Kensington Symphony Orchestra, the Berkeley Science Review design team, the UC Berkeley summer symphony, the Berkeley Adventurers League, East Bay Volleyball, `ravelry.com`, the National, State, and Regional Park Services, and many more, for the

countless opportunities to recharge, laugh, cry, create, enjoy, play, move, relax, get away from the desk, or just procrastinate.

An meine Familie und Verwandschaft auf beiden Seiten des Teiches. Ich schätze mich unheimlich glücklich, dass ich Teil dieser Sippe bin. Vielen Dank, dass ihr mich akzeptiert, wie ich bin, dass ihr meine Entscheidunged unterstützt und mir immer eure ehrliche Meinung kundtut, oder auch einfach mal Solidarität zeigt, je nach dem, was ihr gerade für richtig halted. To my families on both sides of the pond. I am fully aware of how lucky I am to be a part of this amazing tribe. Thank you for accepting me as I am, for supporting my life choices, and always giving me your honest opinion, or unconditional solidarity, depending on what you think is right at the moment. *Vor allem danke ich meinen Eltern Isolde and Werner, die immer für mich da sind, egal auf welchem Kontinent ich mich gerade befinde; die mich in der Weltgeschichte rumwandern lassen und es als Reisegelegenheit nutzen, anstatt mir vorzuhalten, dass ich mich nie daheim blicken lasse. Dank auch an meine Geschwister, die mich zu der Person gemacht haben, die ich heute immer noch werde, ob mit oder ohne Absicht.* To Linda, the wisest of mothers-in-laws, and the rest of my stateside family, for making me feel at home so far away from home.

Felix, vielen Dank für die Freude, die du in unser Leben bringst. Mit deinem Lachen zeigst du mir jeden Tag was im Leben wirklich wichtig ist.

Cait, there are not enough words to describe my gratitude towards you and the support that you have provided during this time. Thank you for enduring my complaints, for celebrating my achievements, for picking me up from the ground (or lying down beside me), for helping me defeat the soul-sucking monster, and for never giving up. You always stand by my side and sleep in my arms. You are joy to my heart and food for my soul. We continue to learn and grow together, even as these years have changed us both. We laugh together in good times and struggle side by side in difficult times. You respect and cherish me as an individual, a partner, and an equal, knowing that we do not complete, but complement each other. We made it through this chapter together, and I know that we are ready for whatever comes next. May we have many more adventures and grow old together.

Chapter 1

Introduction

This dissertation concerns the application of advanced electronic structure methods to understand observables and properties of organic crystals relevant to optoelectronic processes. Relatively cheap to process and mechanically flexible, organic semiconductors have come under increasing focus for their many favorable optoelectronic properties. Molecular materials are known for strong optical absorption and are key-components of dye-sensitized solar cells [1], for example, and novel excited-state phenomena, such as singlet fission [2–8]. With the development of new synthetic pathways and improved material design, molecules can be fine-tuned for specific applications by chemical substitution [9, 10] or morphological control [11, 12]. Maybe the biggest advantages over their inorganic colleagues are their abundance, relative low production cost [13–16], and simple processing techniques [13, 16–18]. All of these attributes make them great candidates for organic LEDs [17, 19–21], thin-film transistors [16, 22–26], photo-voltaic cells [9, 10, 27–29], RFID tags [13], and other applications.

In recent years, many organic systems have been reported to exhibit relatively high charge carrier mobilities,[1] up to $40\,\mathrm{cm^2V^{-1}s^{-1}}$ for holes and $11\,\mathrm{cm^2V^{-1}s^{-1}}$ for electrons [5, 18, 33–43]. However, more than half of the reported mobilities above $1\,\mathrm{cm^2V^{-1}s^{-1}}$ might be unreliable [44], since these values often are extracted based on ideal transistor models; and organic materials often possess non-linear current-voltage characteristics, which, when paired with these ideal models, can result in overestimated mobilities. Furthermore, device lifetime and chemical stability continue to be a challenge for many molecular semiconductors [45–48]. To further improve the efficiency of these systems, and to develop new materials that can overcome existing challenges, better understanding of the underlying principles and mechanisms that determine their properties is needed.

Organic semiconductors, just like inorganic ones, come in three forms: amorphous, liquid

[1] In comparison, hole and electron mobilities of silicon ($\sim$500 $\mathrm{cm^2V^{-1}s^{-1}}$, $\sim$1400 $\mathrm{cm^2V^{-1}s^{-1}}$) or gallium arsenide ($\sim$400 $\mathrm{cm^2V^{-1}s^{-1}}$, $\sim$8000 $\mathrm{cm^2V^{-1}s^{-1}}$) crystals are magnitudes higher [30]. However, amorphous silicon used in thin film transistors and solar cells shows mobilities around $5\,\mathrm{cm^2V^{-1}s^{-1}}$ [31], and the theoretical maximum for amorphous thin film transistors independent of material is estimated as 70/10 [32]. The reported mobility values for organic semiconductors are thus well within the range of application.

crystal, and crystalline. In this work we will focus our attention on the latter. Molecular crystals with extended π-systems are especially attractive for optoelectronic applications. The delocalized π-orbitals yield advantageous band gaps for light absorption, and provide charge transport pathways through intermolecular π-π interactions. In these crystals, the cohesive energy that holds the molecules together is usually dominated by van der Waals (vdW) interactions, including electrostatic interactions and London dispersion. One particular class of organic crystals, the acene family, lends itself to a systematic study. Only containing carbon and hydrogen, this family comprises the series of linearly fused benzene rings (Fig. 1.1). They are experimentally well characterized and known to possess carrier mobilities that are comparatively high for organic materials [40–43]. They also exhibit a propensity for unique excited-state transport phenomena, notably singlet fission (SF) [7, 8, 49–52]. SF has the potential to overcome the Shockley-Queisser limit and significantly boost the efficiency of solar cells [53]. The larger acenes in particular have received recent attention because SF was reported to be exothermic, or nearly so, for tetracene, pentacene, and hexacene [2–4, 36, 54, 55]. Thus, the family of acene crystals provide an important testbed for characterizing and understanding optoelectronic phenomena with a variety of experimental and theoretical methods.

In this work we calculate the electronic and vibrational properties of acenes at zero and finite temperature, using state-of-the-art density functional theory (DFT) and many-body perturbation theory (MBPT), and examine the accuracy of leading-edge approximations in predicting key observables of these systems. We also use those methods to better understand how these observables relate to the atomic and electronic structure. More specifically, we evaluate the performance of different approaches that include vdW interactions; investigate the structural dependence of the low-lying peaks in optical absorption spectra; scrutinize the phonon frequencies and displacements; and lay out in detail how phonons determine finite temperature effects and scattering.

1.1 Ground state properties

DFT has become the formalism of choice for electronic structure calculations of condensed matter systems, due to the balance between accuracy and computational cost for many common approximations. DFT reformulates the solution to the prohibitive many-body Schrodinger equation by solving for the electronic density via fictitious non-interacting electrons. The density gives access to the ground state wave function, and therefore to all ground state observables, that is, observables related to derivatives of the total energy. Thus, for example, we can extract the cohesive energy of crystals, or the vibrational frequencies by systematically displacing atoms and calculating the change in interatomic forces. While DFT is an exact theory of the total energy of a many-particle interacting system, as of yet no exact functional is known. Thus, in practice, DFT's success relies on the help of approximate functionals.

Over the years DFT functionals have seen continuous improvement. Notably, functionals

that explicitly include vdW interactions have seen vast improvements in the last decade and have been shown to yield good results for various materials, especially when weak or noncovalent interactions are at play [56, 57]. While the inclusion of vdW interactions in organic crystals is imperative to obtain accurate and predictive results, there is not yet one single approximation that works equally well for all materials. Therefore, in Chapter 3 we systematically compare the accuracy of the structural parameters and cohesive energies of the full acene series obtained with several vdW approaches. We thus lay the ground work for the subsequent chapters, where we use the vdW methods that yield the best agreement with experimental lattice parameters.

1.2 Electronic excited states

Charge carrier transport and optical absorption involves electronic excited states, which can be obtained with MBPT, using DFT wave functions as a starting point. In MBPT, we calculate the electron self-energy, that is to say, the interaction energy of a charge added to the system with the changes its presence caused in its environment and the other electronic and vibrational degrees of freedom in the system. To compute the electron-electron contributions to the self-energy we use the GW approach [58, 59], where G stands for the one-body Green's function and W for the screened Coulomb potential of the system. During optical absorption, an electron is excited into the conduction band, which leaves behind a positive charge, or hole, in the valence band. Therefore, in addition to the electron-electron self-energies of the electron and hole, the opposite charges interact with each other to form an electron-hole pair, also called exciton. This interaction is calculated with the two-particle Greens functions and Bethe-Salpeter equation (BSE) approach [60–62], making use of the GW approximation.

Both of these methods are being extensively used for periodic and isolated systems (see for example Refs. [63–69], and references therein), and are state-of-the-art for excited state calculations in the condensed phase [70]. Among organic crystals, acenes in particular have been the subject of several computational studies of the excited states, using wave-function-based methods on small molecular clusters [8, 71–76] and DFT/MBPT on periodic systems [77–88], as we do in this work. In Chapter 3 we evaluate the accuracy of these approximations relative to experiment across the acene family, specifically focusing on the effect of structural parameters on these observables. By comparing results obtained with experimental lattice parameters against fully relaxed unit cells, we illustrate the predictive power of *ab initio* calculations using vdW corrected functionals in combination with MBPT.

1.3 Electron-phonon coupling

The temperature dependence of the electronic structure, and thus, for example, the optical absorption or electric mobility, is first and foremost determined by the nuclei. Lattice

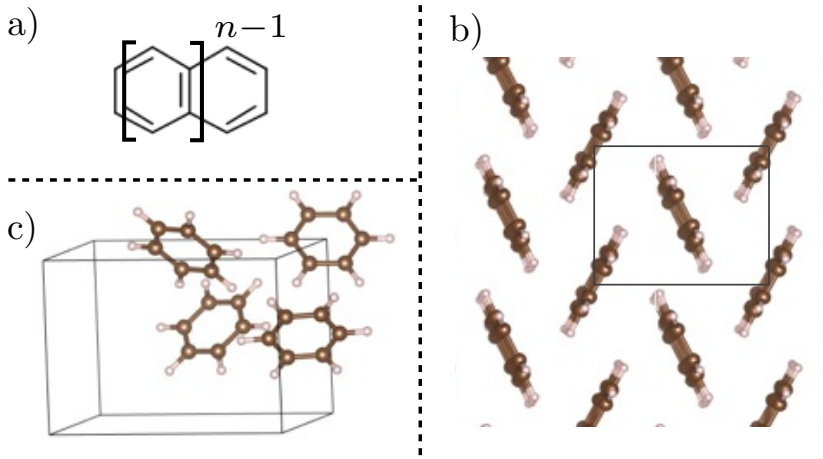

Figure 1.1: The acene family. a) General formula. b) Herringbone structure, taken up by most acenes in the solid state, with space group $P2_1/a$ for naphthalene and anthracene and $P\bar{1}$ for larger acenes. c) Benzene crystallizes in an orthorhombic unit cell with four molecules per unit cell, with space group *Pbca*.

vibrations scatter electronic states, which renormalizes their energies and introduces finite lifetimes. As the phonon occupation changes with temperature, so does the electron-phonon coupling and hence the electronic properties. Additionally, with higher temperatures the volume of the unit cell typically expands, changing intermolecular interactions and phonon frequencies, and hence also the electronic properties. We investigate both these effects from first principles using density functional perturbation theory (DFPT) and MBPT.

In Chapter 4 we calculate the vibrational spectrum of naphthalene across the Brillouin zone, i.e., the phonon band structure. By systematically displacing the atoms we obtain the resulting interatomic force constants that allow us to compute the phonon frequencies and displacement vectors. We then compare the frequencies with experimental values, and further discuss the merits of using a vdW-corrected functional by comparing its results to two conventional DFT functionals.

While this is a standard method for generating phonon dispersions, it is non-trivial to apply to organic crystals, due to their unit cell size and large range of interaction strengths, from weak London dispersion to strong covalent forces. Prior to the publication of our work in 2016, there were only few studies that have calculated the phonon frequencies of organic crystals using first principles methods [89–92], and only two have reported the phonon dispersion [91, 92]. An in-depth analysis of the performance of different DFT functionals and the dependence of phonon frequencies on structural parameters is thus warranted, and necessary as a basis for the subsequent calculation of the electron-phonon coupling.

In Chapter 5 we investigate the temperature dependence of the band gap and the electrical mobility of naphthalene. From DFPT we obtain the derivative of the self-consistent

potential with respect to the individual phonon modes. By integrating the overlap of this potential derivative with the DFT wave functions we obtain the electron-phonon coupling strength. From these electron-phonon couplings we can construct and evaluate the electron-phonon contribution to the electron self-energy. This approach simultaneously yields the renormalization and lifetimes of the electronic states from first principles. In contrast, most prior studies on the electron-phonon coupling in organic crystals employed semi-empirical frameworks or model Hamiltonians, and concentrate exclusively on the lifetimes [38, 93–105]. There are several *ab initio* studies that successfully tackle different aspects of the electron-phonon coupling [106–109]. However, they concentrate only on either the renormalization or the lifetimes [108, 109], or include only two electronic bands in the scattering process [106, 107] (which is appropriate for the lifetimes, but not for the renormalization). We extend these studies by providing a comprehensive analysis of the frequency-dependent electron-phonon coupling and self-energy in naphthalene. To the best of our knowledge we report the first *ab initio* temperature-dependent band gap of a molecular crystal, and calculate the hole and electron mobilities within Boltzmann transport theory. We analyze the effect of lattice expansion on electron-phonon coupling, and discuss the validity of using perturbation theory. This extensive analysis allows us to gain deep insights into the relationships between the structure of molecular crystals and electron-phonon coupling and its emerging temperature-dependent observables.

In summary this dissertation provides a comprehensive computational study of the excited states, vibrational properties, and temperature-dependent behavior of acene crystals in general, and naphthalene in particular.

Chapter 2

Theory and methods

2.1 DFT in solid state systems

2.1.1 Overview

We use density functional theory (DFT) as the starting point of all our calculations. DFT has become a main staple in computational physics and chemistry, and the basis on which many excited-state approaches build upon. While a brief overview of DFT is given here, I will refer the reader to the many good books and reviews in the literature, which are often also more specific to a certain field. (For an excellent introduction to DFT, see for example Ref. [110].)

Solving the adiabatic (or Born-Oppenheimer) many-body Schrödinger equation

$$\hat{\mathcal{H}}\Psi = \left[\sum_i \left(-\frac{\hbar^2}{2m}\nabla_i^2 + V_{\text{ext}}(\mathbf{r}_i)\right) + \sum_{i<j} U(\mathbf{r}_i, \mathbf{r}_j)\right] \Psi(\mathbf{r}_1, \mathbf{r}_2, \ldots, \mathbf{r}_N) = E\Psi(\mathbf{r}_1, \mathbf{r}_2, \ldots, \mathbf{r}_N), \tag{2.1}$$

which depends on the coordinates $\mathbf{r}_i$ of all electrons, is currently impossible to solve exactly for multi-electron systems, since it scales exponentially with N due to the electron-electron interaction in U. The external potential V_{ext} is system specific and due to the interaction of the electrons with the nuclei. The interaction between nuclei is omitted here for simplicity, but in general should be included.

DFT is grounded in a theorem by Hohenberg and Kohn, which proves that the (nondegenerate) ground state wave function Ψ_0 maps to one and only one ground state electronic density $\rho(\mathbf{r})$ [111], that is

$$\Psi_0(\mathbf{r}_1, \mathbf{r}_2, \ldots, \mathbf{r}_N) \Leftrightarrow \rho_0(\mathbf{r}). \tag{2.2}$$

Therefore, if we can calculate the ground state density, we have access to all ground-state observables as well. Furthermore, Hohenberg and Kohn showed that the density that minimizes the total-energy functional

$$E[\rho(\mathbf{r})] = T[\rho(\mathbf{r})] + U[\rho(\mathbf{r})] + \int \mathrm{d}\mathbf{r}\rho(\mathbf{r})V_{\text{ext}}(\mathbf{r}), \tag{2.3}$$

is the ground state density ρ_0. This problem would be much more tractable than the Schrödinger equation, as the density only depends on a three-dimensional variable $\mathbf{r}$, compared to the $3N$ variables of the wave function. However, the exact forms for the kinetic density functional T and the interacting potential U are as of yet unknown.

Shortly following Hohenberg and Kohn's seminal work, Kohn and Sham introduced a set of self-consistent equations that enabled practical applications of DFT [112]. They rewrite the interacting many-body problem in terms of a set of fictitious non-interacting wave functions ψ_i that reproduce the exact ground state density $\rho_0(\mathbf{r}) = \sum_i |\psi_i(\mathbf{r})|^2$ when summed up to the Fermi energy. The Kohn-Sham equations read

$$\left[-\frac{\hbar^2}{2m}\nabla^2 + V_{\mathrm{KS}}[\rho(\mathbf{r})]\right]\psi_i = \varepsilon_i\psi_i \tag{2.4}$$

where V_{KS} is defined as

$$V_{\mathrm{KS}}[\rho(\mathbf{r})] = \int \mathrm{d}\mathbf{r}\rho(\mathbf{r})V_{\mathrm{ext}}(\mathbf{r}) + \int \mathrm{d}\mathbf{r}'\frac{\rho(\mathbf{r}')}{\mathbf{r}-\mathbf{r}'} + V_{\mathrm{xc}}[\rho(\mathbf{r})]. \tag{2.5}$$

The interaction with the nuclei (first term) and the Hartree energy (second term) are straightforward to calculate. The exchange-correlation potential V_{xc} is where the proverbial skeletons in the closet are hidden. It is generally unknown, and the target of continued research and optimization.

The two popular approximations to V_{xc} in the physics of solids are the local density approximation (LDA) and the generalized gradient approximation (GGA). LDA approximates the exchange-correlation potential as

$$V_{\mathrm{xc}}^{\mathrm{LDA}}[\rho(\mathbf{r})] = \int \mathrm{d}\mathbf{r}\,\rho(\mathbf{r})\varepsilon_{\mathrm{xc}}^{\mathrm{hom}}(\rho(\mathbf{r})), \tag{2.6}$$

where $\varepsilon_{\mathrm{xc}}^{\mathrm{hom}}$ is the exchange-correlation energy of a homogeneous electron gas. Due to cancellation of errors in the exchange and correlation part of LDA, which are under- and overestimated, respectively, this seemingly crude approximation performs surprisingly well in practice for certain systems.

In addition to the local value of the density at $\mathbf{r}$, the exchange-correlation energy in GGAs is also a functional of the gradient of $\rho(\mathbf{r})$ [113]

$$V_{\mathrm{xc}}^{\mathrm{GGA}}[\rho(\mathbf{r})] = \int \mathrm{d}\mathbf{r}\,\varepsilon_{\mathrm{xc}}^{\mathrm{GGA}}(\rho(\mathbf{r}), \nabla\rho(\mathbf{r})). \tag{2.7}$$

Here we use the GGA developed by Perdew, Burke, and Ernzerhof (PBE) [114].

2.1.2 Dispersion corrected functionals

Because of the (semi)local nature of the LDA and GGA functionals they inherently neglect nonlocal interactions like van der Waals (vdW) forces. In many molecular crystals, the cohesive energy is exclusively due to vdW forces.

Great strides have been made over the past decade in the treatment of dispersive interactions within DFT (for example, see [57, 115] for overviews). Of the many approaches suggested, one commonly used method is the augmentation of existing (typically semilocal or hybrid) exchange-correlation functionals by pairwise corrections to the internuclear energy expression, which are damped at short range but provide the desired long-range asymptotic behavior [116–123]. The most widely used examples of this idea are Grimme's D2 [119] and D3 [121, 124] corrections and the Tkatchenko-Scheffler (TS) [120] correction scheme. A different commonly used approach, known as vdW-DF, includes dispersion interactions via an explicit nonlocal correlation functional [125–127]. Several vdW-DF versions are in use, starting with the original vdW-DF1 [128] functional. These include, e.g., an improved version, vdW-DF2 [129], making use of a more accurate semilocal exchange functional and an updated vdW kernel; the simplified yet accurate form of Vydrov and van Voorhis, VV10 [130]; and the more recently developed vdW-DF-cx functional [131], an update with improved performance for lattice constants and bulk moduli of layered materials and dense solids. In the following, we abbreviate vdW-DF1 as DF1, etc., for functionals in the vdW-DF class.

2.1.3 Pseudopotentials

To solve the Kohn-Sham equations, we require a basis set. In quantum chemistry these are typically atom centered. For extended systems with translational symmetry, such as considered here, plane waves are a more natural choice, because for periodic systems, one-particle eigenstates take the form

$$\psi(\mathbf{r}) = \mathrm{e}^{\mathrm{i}\mathbf{k}\cdot\mathbf{r}} u(\mathbf{r}), \tag{2.8}$$

named Bloch waves for Felix Bloch, who was one of the first to introduce these wave functions as solutions to periodic potentials [132, 133]. Here, $u(\mathbf{r})$ is a function with the same periodicity as our lattice, and $\mathbf{k}$ the reciprocal wave vector, a good quantum number in a periodic system. In extended systems, we typically express u as a sum over plane waves $\mathrm{e}^{\mathrm{i}\mathbf{G}\cdot\mathbf{r}}$, where $\mathbf{G}$ is a reciprocal lattice vector. The Kohn-Sham wave functions, expanded in such a basis set, are thus written

$$\psi_i(\mathbf{r}) = \sum_{\mathbf{G}} c_{i,(\mathbf{k}+\mathbf{G})}\, \mathrm{e}^{\mathrm{i}(\mathbf{k}+\mathbf{G})\cdot\mathbf{r}}, \tag{2.9}$$

with the basis set coefficients c. Since wave functions are smooth, and high oscillations are relegated to regions near the nucleus, we can truncate the infinite sum, and handle the oscillatory behavior near the nucleus approximately, as discussed below. The cutoff is specified by the kinetic energy cutoff E_{cut} defined as

$$E_{\mathrm{cut}} \geq \frac{\hbar^2}{2m}|\mathbf{G}+\mathbf{k}|^2. \tag{2.10}$$

Because plane waves form a complete basis set, we can systematically converge our calculations by increasing the cutoff energy, and thus the number of plane waves.

To further reduce the number of plane waves needed for an accurate description, we make use of pseudopotentials. The wave functions will oscillate strongest for strongly bound core electrons, close to the atomic core. This is a result of the larger electron density, the Pauli principle, and the orthogonality constraint. At the same time, the electronic properties we are interested in are mostly determined by valence electrons. Without losing much accuracy, we can thus replace the potential from core electrons up to a certain radius by a smooth, effective potential. This cutoff radius is somewhat arbitrary, and one can generate hard (small radius), soft, or even ultrasoft (large radius) pseudopotentials. With a larger cutoff radius, the wave functions will be smoother, we need fewer plane waves, and therefore can run faster and larger calculations. However, the resulting wave functions are further and further from the "true" wave function, and may lead to unphysical properties, particularly if the atoms are arranged in a way that the core regions overlap. In general, any new pseudopotential needs to be thoroughly tested against known standards.

2.2 Lattice vibrations

2.2.1 Theory

For Chapter 4 we calculate the vibrational spectrum of naphthalene within the adiabatic, harmonic approximation. In condensed-matter physics, collective vibrations, where all atoms vibrate at the same frequency, are called phonons. Each phonon is associated with a displacement vector ξ specifying the amplitude and direction of displacement of each atom in the crystal.

To calculate the frequency and accompanying displacement vector, we follow the standard derivation [134, 135] and expand the adiabatic potential around the equilibrium positions of the atoms as a Taylor series

$$V = V^0 + \sum_{j,\alpha} \frac{\partial V}{\partial r_j^\alpha} u_j^\alpha + \frac{1}{2} \sum_{\substack{j,\alpha \\ j',\alpha'}} \frac{\partial^2 V}{\partial r_j^\alpha \partial r_{j'}^{\alpha'}} u_j^\alpha u_{j'}^{\alpha'} + \ldots, \tag{2.11}$$

with $u_j^\alpha = r_j^\alpha - r_j^{\alpha,0}$ the small displacement of atom j along the Cartesian direction $\alpha = x, y, z$. Truncating at quadratic order yields the harmonic approximation.

Since we are not concerned about the absolute value of the potential, we can set $V^0 = 0$ as our reference energy. The first derivative of the potential, or the forces acting on the atoms, vanishes as well for systems in equilibrium. The first non-zero term is the second derivative of the potential, i.e., the force constant $K_{jj'}^{\alpha\alpha'}$, or change of force, of atom j in direction α, when atom j' is displaced in direction α'. Our adiabatic, harmonic potential thus reads

$$V = \frac{1}{2} \sum_{\substack{j,\alpha \\ j',\alpha'}} K_{jj'}^{\alpha\alpha'} u_j^\alpha u_{j'}^{\alpha'}. \tag{2.12}$$

$K_{jj'}^{\alpha\alpha'}$ is a $3n_{\text{tot}} \times 3n_{\text{tot}}$ matrix (n_{tot} = total number of atoms), and therefore impossible to manage for any extended system. To solve this equation efficiently, we can take advantage of the fact that $K_{jj'}^{\alpha\alpha'}$ obeys the same symmetries as our system, and is thus also translationally invariant for periodic systems. We first split the atom index j into the combined index (κ, ℓ), where κ specifies the lattice site, and ℓ the unit cell the atom resides in. The force constants between two sites κ and κ' now only depend on the distance between the respective unit cells, so $K_{jj'}^{\alpha\alpha'}$ becomes $K_{\kappa\kappa'}^{\alpha\alpha'}(\mathbf{R}_\ell - \mathbf{R}_{\ell'})$.

For the purpose of calculating the frequency spectrum, the atomic motion can be adequately described by the classical equation of motion of the form $F = ma$, Newton's second law. With Eq. (2.12) we can write

$$m_\kappa \frac{\partial^2 u_{\kappa,\ell}^\alpha}{\partial t^2} = -\frac{\partial V}{\partial u_{\kappa,\ell}^\alpha} = -\sum_{\kappa',\alpha',\ell'} K_{\kappa\kappa'}^{\alpha\alpha'}(\mathbf{R}_\ell - \mathbf{R}_{\ell'}) u_{j',\ell'}^{\alpha'}, \tag{2.13}$$

where m_κ is the mass of atom κ. The general ansatz for solving second-order differential equations is $u_{\kappa,\ell}^\alpha(t) = A\mathrm{e}^{-i\omega t}$. More specifically, we are looking for vibrational plane wave solutions, analogous to Bloch wave functions, of the form

$$u_{\kappa,\ell}^\alpha(t) = \frac{C_\kappa^\alpha}{\sqrt{m_\kappa}} \mathrm{e}^{\mathrm{i}\mathbf{q}\cdot\mathbf{R}_\ell - \mathrm{i}\omega t}, \tag{2.14}$$

where C_κ^α describes the amplitude and direction of the atomic displacement, and is also called the polarization vector. Substituting Eq. (2.14) in Eq. (2.13) we obtain the following coupled set of $3n_{\text{uc}}$ linear equations (n_{uc} = number of atoms in unit cell)

$$\omega^2 C_\kappa^\alpha = \sum_{\kappa',\alpha'} D_{\kappa\kappa'}^{\alpha\alpha'}(\mathbf{q}) C_{\kappa'}^{\alpha'}, \tag{2.15}$$

where we introduced the dynamical matrix $\mathbf{D}(\mathbf{q})$

$$D_{\kappa\kappa'}^{\alpha\alpha'}(\mathbf{q}) = \sum_{\ell'} \frac{K_{\kappa\kappa'}^{\alpha\alpha'}(\mathbf{R}_{\ell'})}{\sqrt{m_\kappa m_{\kappa'}}} \mathrm{e}^{\mathrm{i}\mathbf{q}\cdot\mathbf{R}_{\ell'}}, \tag{2.16}$$

which is the discrete, mass-weighted Fourier transform of the force constant matrix. Since we can choose our origin arbitrarily, we dropped the index ℓ, and denote the distance between unit cells simply with $\mathbf{R}_{\ell'}$. Any solutions to the coupled equations in Eq. (2.15) have to satisfy

$$\det\left(\mathbf{D}(\mathbf{q}) - \omega^2 \mathbf{I}\right) = 0. \tag{2.17}$$

By diagonalizing the dynamical matrix, we therefore obtain the squared frequencies as eigenvalues $\omega(\mathbf{q})$, and orthogonal polarization vectors as complex eigenvectors $\mathbf{C}(\mathbf{q})$, also called normal modes. Note that systems with instabilities can yield negative eigenvalues that yield

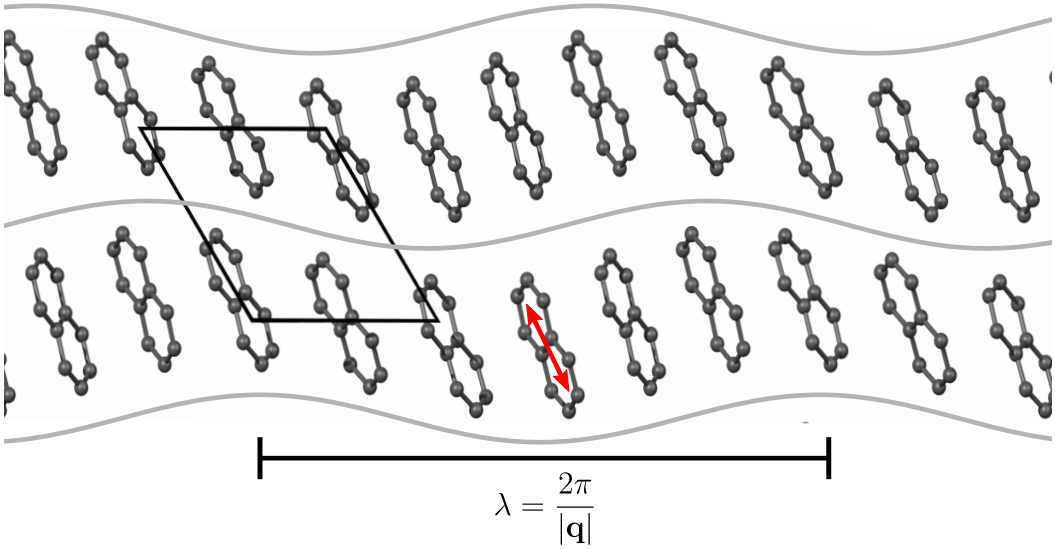

Figure 2.1: Example of a translational mode in naphthalene. This is the first acoustic mode at wave vector $\mathbf{q} = 2\pi/a(0.33, 0, 0)$, where almost rigid molecules vibrate along the c axis (red arrow). The displacement of equivalent atoms in different unit cells differs by the phase of $e^{i\mathbf{q}\cdot\mathbf{R}}$, creating a propagating wave (gray lines). The direction of this wave is given by $\mathbf{q}$ (in this case along x). Hydrogen atoms are omitted for simplicity.

imaginary frequencies, often, by convention, presented as negative frequencies. Furthermore, the (non-orthogonal) real space displacement vectors for any given wave vector $\mathbf{q}$ can be obtained as

$$\xi^{\alpha}_{\kappa,\ell}(t) = \mathrm{Re}\left[\frac{C^{\alpha}_{\kappa}(\mathbf{q})}{\sqrt{m_\kappa}} e^{i\mathbf{q}\cdot\mathbf{R}_\ell - i\omega(\mathbf{q})t}\right]. \tag{2.18}$$

One such displacement pattern of a translational phonon mode is shown in Fig. 2.1.

What did we gain by rewriting Eq. (2.13) in terms of the dynamical matrix? Instead of solving the equation of motion once for n_{tot} atoms (or n_{uc} times the number of unit cells N), we now can compute the dynamical matrix with only n_{uc} atoms times the number of $\mathbf{q}$-points, which is equivalent to N. While the former scales as $\mathcal{O}(N^3)$ due to matrix inversions, the latter scales only linearly as $\mathcal{O}(N)$. We will take a brief look at other advantages and disadvantages of either method in the following section.

2.2.2 Methods

Based on the previous section we can obtain the phonon frequencies and vectors either by calculating the real space force constant matrix directly, or via its Fourier transform, the dynamical matrix. Within DFT, the former is typically done using the finite difference (FD) approach, the latter using density functional perturbation theory (DFPT).

In the FD approach, we displace each atom in each Cartesian direction to obtain the resulting change of forces on each atom

$$K^{\alpha\alpha'}_{\kappa\kappa'}(\mathbf{R}_{\ell'} - \mathbf{R}_{\ell'}) \approx \frac{\Delta F^{\alpha}_{\kappa,\ell}}{\Delta u^{\alpha'}_{\kappa',\ell'}}. \tag{2.19}$$

The individual forces can be obtained based on the Hellmann-Feynman theorem [136, 137]. Great care has to be taken that the displacements are small enough to be in the linear regime, and that the forces are well converged. In DFT this means that the convergence criterium for the SCF cycles has to be orders of magnitude tighter than typically necessary for total energy calculations (see Appendix B.1 for convergence criteria). Once we have the force constant matrix, we can interpolate to any arbitrary **q**-point using Eq. (2.16), to obtain the phonon dispersion in reciprocal space.

The main advantage of the FD method is that anharmonic contributions are directly accessible. Displacing each atom by larger amounts allows the determination of higher-order coefficients of Eq. (2.11). Furthermore, any method or functional that can produce Hellmann-Feynman forces can be used to generate FDs. In contrast DFPT might not be readily implemented with every electronic structure code, or for every functional. This is the main reason we use FD in Chapter 4, because van der Waals–corrected functionals were not compatible with DFPT in Quantum ESPRESSO at that time.

The obvious disadvantage is that we have to use a supercell that is large enough to capture all interatomic interactions. Convergence with respect to supercell size can be checked by comparing the resulting frequencies $\omega(\mathbf{q})$ for increasing numbers of unit cells. Recently the use of non-diagonal supercells has been rediscovered for a more efficient calculation of phonons using FD [138]. (For a review including non-diagonal supercells, see [139].)

In DFPT we calculate the linear response of the electron density to individual atomic displacements. (For a detailed discussion of DFPT see [140].) Since this can be achieved in reciprocal space, we can calculate the dynamical matrix at any arbitrary **q**-point. In order to obtain a continuous phonon dispersion, we typically calculate the dynamical matrices on a regular **q**-grid, Fourier transform to obtain the real space interatomic force constants (Eq. (2.16)), and transform back, allowing us to interpolate to any arbitrary **q**-point. Equivalent to the supercell size, the number of **q**-point in our grid determines the accuracy of interpolation. Convergence here can be easily checked by comparing the frequencies explicitly calculated with DFPT at a **q**-point not on the regular grid with the interpolated values obtained for the same point.

With either method, the atomic coordinates need to be relaxed with very tight constraints, and with the same parameters that we then use for the subsequent phonon calculation. Numerical differences arising from different wave function cut offs, **k**-point grids, or even FFT (Fast Fourier Transform) grids can have a significant impact. Imaginary frequencies are common results, and are dreaded by anyone who ever ran phonon calculations. Small imaginary frequencies ($<10\mathrm{i}\,\mathrm{cm}^{-1}$) of the acoustic modes at Γ ($\mathbf{q} = 0$) are normal and usually the result of using discrete numerical methods, and can be avoided by imposing the acoustic

sum rule, i.e., the translational invariance. Larger imaginary frequencies, especially at $\mathbf{q} \neq 0$, are more difficult to handle, since they can have various origins. The most obvious one is unconverged parameters (like the SCF convergence parameter mentioned above). However, it can also point to a structural instability. This happens either when the ground state atomic coordinates are not relaxed sufficiently; or when the system is artificially constrained in a higher symmetry than it would naturally have at 0 K (see [141] for a prominent example of "physical" instabilities). This can be tested by freezing in the unstable phonon mode, i.e., moving the atoms along the displacement vector from Eq. (2.18) in either direction. If the energy goes down, it confirms the presence of a lower-energy structure. Performing this test for non-zero $\mathbf{q}$-points requires a supercell commensurate with the wave vector. This can result in very large calculations when dealing with small $\mathbf{q}$ vectors, or even be impossible if $\mathbf{q}$ is irrational. In order to confirm such instabilities, the only path may be to rule out unconverged parameters with absolute certainty.

Last but not least, ultimate validation for a phonon calculation comes from comparison with experiment, if data are available. Inelastic neutron scattering measures the reciprocal phonon dispersion [142] and therefore provides the most straightforward comparison. Unfortunately, it is not as straightforward to produce these spectra, so experimental phonon dispersions are not always available.

Much more common are infrared (IR) and Raman experiments. Using wavelengths from infra-red to UV, however, these techniques only capture phonons near the center of the Brillouin zone at Γ. The typical phonon wave vectors are much too short (on the order of lattice vectors) to be resolved by the long wavelength of the probe light (10^3–10^5 Å). Or inversely, since conservation of momentum is required, and the momentum of the photons is much smaller than that of the phonons, only phonons near $\mathbf{q} = 0$ interact with the photons. While this means we only need to calculate the phonons for a single unit cell, or equivalently for a single point $\mathbf{q} = 0$, a comparison between calculated and experimental frequencies has more degrees of freedom, as we lack the information of phonon dispersion.

This can be mitigated by taking advantage of the different selection rules for IR and Raman active modes, and the absorption intensities. Phonon modes that change the dipole of the system are IR active, while Raman-active modes change the polarizability. In centrosymmetric systems, such as the acenes studied here, phonon modes are *either* IR *or* Raman active, with IR modes breaking the inversion symmetry and Raman modes preserving it. The phonon displacements are readily available from computation, so calculated frequencies can be clearly designated as IR or Raman active.

Still, accurate mode assignment is far from trivial, and often somewhat arbitrary. Some modes show very low intensity in experimental spectra, or disappear in the noise, and others have so-called overtones, that can be mistaken for fundamental frequencies. The large number of phonon modes in organic crystals, and limited resolution in experimental spectra further muddy the waters. In our case we opted to assign any calculated frequency to the closest frequency of the same type (IR or Raman), making sure to assign any mode only once.

2.3 Many-body perturbation theory

2.3.1 Electron-electron and electron-phonon self-energy

For the accurate description of excited-state properties, such as the band gap, or charge carrier transport, we have to go beyond the mean-field Hamiltonian of DFT. To add corrections due, for example, to electron-electron correlation, or electron-phonon coupling, we extend Eq. (2.4) within the formalism of many-body perturbation theory (MBPT), which amounts to adding a term called the self-energy Σ

$$\left[-\frac{\hbar^2}{2m}\nabla^2 + V_{\mathrm{KS}}[\rho(\mathbf{r})] + \Sigma\right]\psi_i = \varepsilon_i\psi_i. \tag{2.20}$$

Equation (2.20) is an effective equation for a single electron or hole in a many-particle interacting system. The self-energy represents the nonlocal and energy-dependent interactions of an electron with the other electronic and vibrational degrees of freedom in the many-body system of interest, and the changes its presence causes in the associated environment. This correction is usually evaluated perturbatively. We can use this framework to study the effects of various processes. In this work we calculate the electron-electron and electron-phonon contributions to the electron self-energy using MBPT.

2.3.2 GW

Our first-principles MBPT calculations for charged excitations are based on the GW approximation. Practically speaking, GW calculations usually proceed perturbatively based on a DFT starting point, which for solids is usually computed using the Kohn-Sham equation within the LDA or GGA. The Kohn-Sham eigenvalues and eigenfunctions are used to evaluate approximately the self-energy operator Σ as
iGW, where G is the one-electron Green's function of the system and $W = \epsilon^{-1}v$ is the dynamically screened Coulomb interaction; v is the Coulomb potential and ϵ is the wave-vector- and frequency-dependent dielectric function [58, 59].
iGW is the first term in a many-body expansion of Σ in W. The DFT eigenvalues are then updated via first-order perturbation theory. This approach is known as the G_0W_0 approximation. This method is often very successful, but nevertheless it is somewhat dependent on the DFT starting point.

GW can be evaluated, in principle, self-consistently by different approaches [64, 143–148], mitigating the starting-point dependence by iterating over eigenvalues and wave functions. This effectively incorporates higher-order terms in Σ. Given the computational demands associated with acene crystals, in the following we limit our study to the diagonal part of Σ.

2.3.3 BSE

Given the GW-computed quasiparticle energies, as well as the static inverse dielectric function computed within the random phase approximation, we compute neutral excitation en-

ergies by solving the Bethe-Salpeter equation (BSE) [60–62]. We use an approximate form of the BSE, developed within a first-principles framework by Rohlfing and Louie [62], which involves solving a new eigenvalue problem obtained from an electron-hole interaction matrix. We generate solutions within the Tamm-Dancoff approximation (TDA) and limit our calculations to low-lying singlet and triplet excitations.

2.4 Electron-phonon coupling

2.4.1 AHC theory

We obtain the contribution of the electron-phonon coupling (EPC) to the electron self-energy using the Allen-Heine-Cardona (AHC) theory [149, 150]. The AHC theory employs second-order perturbation theory, within the adiabatic harmonic approximation, to calculate the change of the Kohn-Sham eigenenergies, denoted here as Σ^{ep}, further also called the electron-phonon self-energy. The displacement of phonon modes, even at 0 K due to zero-point motion, leads to coupling (or scattering) of electronic states. This coupling is responsible for the self-energy Σ^{ep}, which is a complex quantity, with a real and imaginary part. As such, it not only renormalizes the energies (real part), but also introduces finite lifetimes (imaginary part), and hence broadening of the states.

Within DFT we solve for the single-particle Kohn-Sham states

$$\left\langle n\mathbf{k}\middle| -\frac{\hbar^2}{2m_e}\nabla^2 + V_{\text{KS}}(\mathbf{r},\mathbf{R}_0)\middle| n\mathbf{k}\right\rangle = \varepsilon^0_{n\mathbf{k}}. \tag{2.21}$$

V_{KS} is defined in Eq. (2.5), and depends parametrically on the nuclear coordinates $\mathbf{R}$. We can expand the potential around the equilibrium position $\mathbf{R}_0$ of the atoms in a Taylor series with respect to small displacements along the phonon mode vectors U_ν

$$V_{\text{KS}}(\mathbf{r},\mathbf{R}) = \; V_{\text{KS}}(\mathbf{r},\mathbf{R}_0) \; + \; \frac{\partial V_{\text{KS}}}{\partial \mathbf{R}}\,\mathbf{U}_\nu \; + \; \frac{1}{2}\frac{\partial^2 V_{\text{KS}}}{\partial \mathbf{R}^2}\,\mathbf{U}_\nu^2 \; + \; \ldots \tag{2.22}$$

similar to how we calculated phonons. The main difference is that we calculate the changes in energy of each individual state $n\mathbf{k}$, instead of the change in total energy. Second, instead of looking at the perturbation of individually displaced atoms, we directly rotate the displacements into the orthogonal, uncoupled normal mode basis.

The first order correction

$$\varepsilon^1_{n\mathbf{k}} = \left\langle n\mathbf{k}\middle| \frac{\partial V_{\text{KS}}}{\partial \mathbf{R}}\middle| n\mathbf{k}\right\rangle \langle \mathbf{U}_\nu\rangle \tag{2.23}$$

vanishes since the expectation value of the mode displacement $\langle \mathbf{U}_\nu\rangle$ is zero. The second order correction

$$\varepsilon^2_{n\mathbf{k}} = \left[\sum_{m\mathbf{k}'} \frac{\left\langle n\mathbf{k}\middle| \frac{\partial V_{\text{KS}}}{\partial \mathbf{R}}\middle| m\mathbf{k}'\right\rangle \left\langle m\mathbf{k}'\middle| \frac{\partial V_{\text{KS}}}{\partial \mathbf{R}}\middle| n\mathbf{k}\right\rangle}{\varepsilon^0_{n\mathbf{k}} - \varepsilon^0_{m\mathbf{k}'}} + \left\langle n\mathbf{k}\middle| \frac{\partial^2 V_{\text{KS}}}{\partial \mathbf{R}^2}\middle| n\mathbf{k}\right\rangle\right] \langle \mathbf{U}_\nu^2\rangle \tag{2.24}$$

consists of two terms involving the first and second derivatives of the Kohn-Sham potential. They are called the Fan[1] and Debye-Waller (DW) term, respectively. Again, we neglect any higher-order terms.

The rigorous derivation of this energy correction in periodic systems via the Dyson equation can be found in Refs. [150–152], along with some historical context. The frequency dependent Fan term is thus given as

$$\begin{aligned}\Sigma^{\mathrm{Fan}}_{n\mathbf{k}}(\omega, T) = \sum_{\nu\mathbf{q}} \frac{1}{2\omega_{\nu\mathbf{q}}} \sum_{m} \left| \langle \psi_{n\mathbf{k}} \mid V^{(1)}_{\nu\mathbf{q}} \mid \psi_{m\mathbf{k}+\mathbf{q}} \rangle \right|^2 \\ \times \Big[\frac{N_{\nu\mathbf{q}}(T) + f_{m\mathbf{k}+\mathbf{q}}(T)}{\omega - \varepsilon^0_{m\mathbf{k}+\mathbf{q}} + \omega_{\nu\mathbf{q}} + i\eta\,\mathrm{sgn}(\omega)} \\ + \frac{N_{\nu\mathbf{q}}(T) + 1 - f_{m\mathbf{k}+\mathbf{q}}(T)}{\omega - \varepsilon^0_{m\mathbf{k}+\mathbf{q}} - \omega_{\nu\mathbf{q}} + i\eta\,\mathrm{sgn}(\omega)} \Big].\end{aligned} \tag{2.25}$$

The phonon modes are defined by indices ν, wave vector $\mathbf{q}$, energies $\omega_{\nu\mathbf{q}}$, and occupation factor $N_{\nu\mathbf{q}}$. Phonons couple electrons in state $n\mathbf{k}$ with state $m\mathbf{k}+\mathbf{q}$ and occupation factor $f_{m\mathbf{k}+\mathbf{q}}$ through the first derivative of the potential $V^{(1)}_{\nu\mathbf{q}}$ associated with the respective phonon's atomic displacement. The integrals $\langle \psi_{n\mathbf{k}} \mid V^{(1)}_{\nu\mathbf{q}} \mid \psi_{m\mathbf{k}+\mathbf{q}} \rangle$, or electron-phonon matrix elements further referred to as $g^{\nu\mathbf{q}}_{nm\mathbf{k}}$, determine the coupling strength between the electronic states and the phonons. The denominators give rise to poles at $\omega = \varepsilon^0 \pm \omega_{\nu\mathbf{q}}$, which are smoothed with a small smearing parameter η that is positive and real, to account for the finite $\mathbf{q}$-grid sampling.

The frequency independent DW term becomes

$$\Sigma^{\mathrm{DW}}_{n\mathbf{k}}(T) = \sum_{\nu\mathbf{q}} \frac{1}{2\omega_{\nu\mathbf{q}}} \langle n\mathbf{k} \mid V^{(2)}_{\nu\mathbf{q}} \mid n\mathbf{k} \rangle \big[2n_{\nu\mathbf{q}}(T) + 1 \big]. \tag{2.26}$$

The DW term still depends on the second derivative of the potential $V^{(2)}_{\nu\mathbf{q},\nu\mathbf{q}}$, which is arduous to calculate. Using the rigid-ion approximation, however, Eq. (2.26) can be written in terms of the first derivative of the potential [151, 153]. Thus, we can obtain all values from DFT and DFPT calculations.

Putting Eqs. (2.25) and (2.26) together, we can rewrite the second-order correction of Eq. (2.24) as

$$\Sigma^{\mathrm{ep}}_{n\mathbf{k}}(\omega, T) = \Sigma^{\mathrm{Fan}}_{n\mathbf{k}}(\omega, T) + \Sigma^{\mathrm{DW}}_{n\mathbf{k}}(T). \tag{2.27}$$

We changed the notation of the EPC energy from ε^2 to Σ^{ep} to highlight that it is now a complex energy, and to distinguish from otherwise purely real electronic eigenvalues and energies denoted with ε.

The renormalization of the electronic eigenvalues is given by the real part of Σ^{ep}. The imaginary part determines the broadening, or inverse lifetimes of the electronic states. The

[1] Sometimes also referred to Migdal or Fan-Migdal term.

temperature dependence of the self-energy arises through the temperature dependent occupation factors of the phonons N and electrons f. We can see that even at 0 K, the self-energy has a finite value. This leads to the so called zero-point renormalization (ZPR); and states other than the global conduction band minimum (CBM) and global valence band maximum (VBM) will be broadened at zero temperature.

There remain two challenges to calculate the self-energy efficiently. First, **q**-space has to be sampled more densely compared to a phonon calculation, which rapidly becomes the main obstacle for large systems. In this work, we interpolate the phonon coupling potential in real space, following the approaches of [154, 155]. It is standard practice to interpolate the phonon frequencies of a regular **q**-grid onto arbitrary **q**-points by means of a Fourier transform of the dynamical matrices to real space, and back to reciprocal space. Applying the same principle here, we first calculate the potential derivative with DFPT on a coarse **q**-point grid and interpolate to a finer grid via Fourier transform. We first define the long-range component of the phonon potential

$$V^{L}_{\kappa j}(\mathbf{q},\mathbf{r}) = i\frac{4\pi}{\Omega}\sum_{\mathbf{G}\neq-\mathbf{q}}\frac{e^{i(\mathbf{q}+\mathbf{G})\cdot(\mathbf{r}-\tau_\kappa)}(\mathbf{q}+\mathbf{G})_{j'}\cdot Z^{*}_{\kappa,j'j}}{(\mathbf{q}+\mathbf{G})\cdot\epsilon^{\infty}\cdot(\mathbf{q}+\mathbf{G})}, \tag{2.28}$$

where ϵ^{∞} is the static long-ranged dielectric matrix without the lattice contribution to the screening, and $Z^{*}_{\kappa,j'j}$ is the Born effective charge tensor. These quantities are computed from DFPT by including the response of the system to a macroscopic electric field. The long-ranged component of the phonon potential represents the dipole potential created by displacing the Born effective charges of each atom, and becomes the dominant contribution to the potential in the limit $\mathbf{q}\to 0$. Next, we perform a Fourier transform of the short-range component of the phonon coupling potential, starting from the coarse **q**-point grid,

$$W_{\kappa j}(\mathbf{r}-\mathbf{R}_l) = \sum_{\mathbf{q}} e^{i\mathbf{q}\cdot\mathbf{R}_l}\left(V^{(1)}_{\kappa j}(\mathbf{q},\mathbf{r}) - V^{\mathrm{L}}_{\kappa j}(\mathbf{q},\mathbf{r})\right) \tag{2.29}$$

where $W_{\kappa j}(\mathbf{r}-\mathbf{R}_l)$ represents the short-range component of the perturbative potential associated with the displacement of atom κ in the unit cell l along the Cartesian direction j. The interpolated phonon potential for an arbitrary point $\tilde{\mathbf{q}}$ is then

$$V^{(1)}_{\kappa j}(\tilde{\mathbf{q}},\mathbf{r}) \approx \sum_{l} W_{\kappa j}(\mathbf{r}-\mathbf{R}_l)e^{-i\tilde{\mathbf{q}}\cdot\mathbf{R}_l} + V^{\mathrm{L}}_{\kappa j}(\tilde{\mathbf{q}},\mathbf{r}). \tag{2.30}$$

This interpolation scheme reproduces the electron-phonon coupling matrix elements with accuracy better than 1 %, as shown in Fig. C.4 in the Appendix.

The second challenge lies in the sum over electronic states m in Eq. (2.25), which converges slowly with the number of bands included. We evaluate this sum explicitly using all valence bands, and conduction bands up to 5 eV above the CBM. Above this cut-off the sum over infinite bands is replaced by a Sternheimer equation, and their contribution to the self-energy is treated statically [156, 157]. Furthermore, this contribution is evaluated on the coarse **q**-grid, since the denominator of the self-energy in Eq. (2.25) is never small for these bands, and is thus a smooth function of **q**.

Chapter 3

Electronic structure of acenes

The work presented in this chapter has been published as part of Ref. [158]. I contributed to the structural relaxations of the unit cells, comparing results for conventional and van der Waals corrected functionals.

Predicting the structure and excited-state properties of molecular crystals presents a challenge for electronic structure theory, as standard approximations to density functional theory (DFT) do not capture long-range van der Waals (vdW) dispersion interactions and do not yield excited-state properties. In this chapter, we use a combination of DFT including vdW forces, using both nonlocal correlation functionals and pairwise correction methods, together with many-body perturbation theory (MBPT) to study the geometry and excited states, respectively, of the entire series of oligoacene crystals, from benzene to hexacene. We find that vdW methods can predict lattice constants within 1 % of the experimental measurements, on par with the previously reported accuracy of pairwise approximations for the same systems. We further find that excitation energies are sensitive to geometry, but if optimized geometries are used MBPT can yield excited-state properties within a few tenths of an eV from experiment.

3.1 Introduction

Theoretical studies of excited-state properties of acene crystals have often been performed with small molecular clusters, using wave-function-based methods [8, 71–76], or with extended systems, using density functional theory (DFT) and many-body perturbation theory (MBPT) [77–88]. These calculations have often yielded excellent agreement with experiment and new insights into excited-state properties of acene crystals.

As shown in Fig. 1.1, acene crystals consist of aromatic monomers packed in ordered arrangements. Their constituent monomers possess strong intramolecular covalent bonds, but weak intermolecular dispersive interactions govern the crystal structure. Because the approximate exchange-correlation functionals most commonly used in DFT calculations do

not account for dispersive interactions, the above-mentioned theoretical calculations have nearly always made use of experimental data for intermolecular distances and orientation. This limits predictive power because experimental lattice parameters can be scarce or conflicting. In particular, different polymorphs of the same material may exist, sometimes even coexisting in the same sample [82, 88, 159–165].

Fortunately, the last decade has seen rapid development of DFT-based methods that can capture dispersive interactions and several studies have demonstrated that addressing these interactions allows for predicting accurate geometries and cohesive energies of molecular solids in general and acenes in particular (see, e.g., Refs. [82, 90, 166–177]). Specifically, Ambrosch-Draxl et al. [82] have suggested that a combination of dispersion-inclusive DFT methods, which they found to predict lattice parameters in agreement with experiments for acene crystals, followed by MBPT calculations can be used to explore quantitative differences in optical properties of pentacene polymorphs. Their work suggests that a broader study of the entire acene family with MBPT methods, especially their recent refinements, would be highly desirable.

In this chapter, we combine dispersion-inclusive DFT and MBPT to study the geometry and excited states of the entire series of acene crystals, from benzene to hexacene. In each case, we compare the computed geometry, electronic structure, and optical excitations with experiment. To account for long-range van der Waals (vdW) dispersive interactions, we use primarily nonlocal vdW density functionals (vdW-DFs), but also employ Grimme's D2 pairwise corrections [119] and compare our results where possible with previously reported data computed with the Tkatchenko-Scheffler (TS) [120] pairwise correction approach [89, 169]. We find that the new consistent-exchange (cx) vdW density functional (vdW-DF-cx) [131, 178] can predict acene lattice parameters within 1 percent of low-temperature measurements, as can the TS method. For optimized acene crystal structures, our MBPT calculations within the *GW* approximation using the Bethe-Salpeter equation approach lead to electronic band structures, and low-lying singlet and triplet excitations in good quantitative agreement with experiments. Interestingly, we find that low-lying excited states are sensitive to crystal geometry, particularly so for singlets, which are significantly more delocalized than triplets. This chapter constitutes a survey and validation study of both crystal structure and excited-state electronic structure for this important class of molecular crystals. Furthermore, it highlights the structural sensitivity of the electronic energies and the need to include vdW forces for accurate predictive modeling of excited states.

3.2 Results and discussion

3.2.1 Lattice geometry and cohesive energy

We begin our discussion by considering the effect of the chosen DFT approximation on the crystal geometry and cohesive energy. Experimental unit-cell volumes for the acene crystals are compared in Fig. 3.1(a) with volumes calculated using the LDA, PBE, PBE-D2, PBE-TS

(from Refs. [89, 169]), DF1, DF2, and DF-cx approaches. A similar comparison for cohesive energies is given in Fig. 3.1(b), where we calculated the cohesive energy via the standard relation

$$E_{\mathrm{coh}} = E_{\mathrm{gas}} - \frac{1}{N} E_{\mathrm{solid}} \tag{3.1}$$

where E_{gas} is the total energy of an isolated monomer, E_{solid} is the total energy of the solid phase unit cell, and N is the number of molecules per unit cell in the solid. A complete set of structural data, along with error estimates, is given in Appendix A.2. For tetracene, its polymorph 1 (P_1) also called the high-temperature polymorph [179, 180], referred to as TETCEN in the Cambridge Structural Database (CSD) [181], is considered. This crystal is known to undergo a pressure-assisted transition to a different high-pressure or low-temperature polymorph (P_2) [161, 182–186], the study of which is beyond the scope of this work. This low-temperature polymorph has been successfully described within the TS method in Ref. [89]. For pentacene, three well-known polymorphs are considered, using experimental structures available in the CSD [181]. These are as follows:

Figure 3.1 shows, as expected, that standard (semi)local functionals do not result in good agreement with experimental results. PBE significantly overestimates lattice constants and underestimates cohesive energies. This can be attributed directly to the lack of treatment of dispersive interactions in PBE [172]. LDA lattice constants are underestimated by ∼3 %, but this binding is spurious, rather than reflecting a successful treatment of dispersive interactions [172]. The spurious binding is attributable to the insufficient treatment of exchange [193, 194].

Turning to explicit vdW functionals, Fig. 3.1(a) clearly shows that DF1 overestimates lattice constants essentially as much as LDA underestimates them. This is because DF1 is based on the exchange of revPBE [195], a variant of PBE with exchange that is too repulsive for the systems studied here. At the same time, Fig. 3.1(b) shows that it still overestimates binding energies. We note that cohesive energies of acene crystals have been calculated with DF1 prior to this work [82, 166, 169], with differing conclusions. While DF1 results for E_{coh} are in agreement with experiment to better than 5 % in Refs. [82, 166], Ref. [169] reports DF1 results that deviate from experiment by as much as ∼17 %. These differences can be partially explained by the different choices these studies made for the experimental reference data. Some differences remain even if we use the experimental values of Ref. [90], in which the contributions due to vibrations are carefully taken into account, throughout. Despite having carefully ruled out lack of convergence in our calculations, the average percentage error (see Table A.1 in Appendix A.2) in E_{coh} is then somewhat larger in this study, being 16 %, 10 %, and 9 % in the data of our work, Ref. [169], and Ref. [82], respectively. For the lattice parameters, however, we find good agreement (within 2 %) with those reported previously.

Figure 3.1(a) clearly shows that DF2 improves geometries with respect to DF1, in agreement with the findings in Ref. [169], with further improvement gained from DF-cx. Specifically, lattice constants are within 2 % and 1 %, respectively, of experiment. Fortuitously, DF2 values for the lattice parameters are similar to the thermally expanded lattice param-

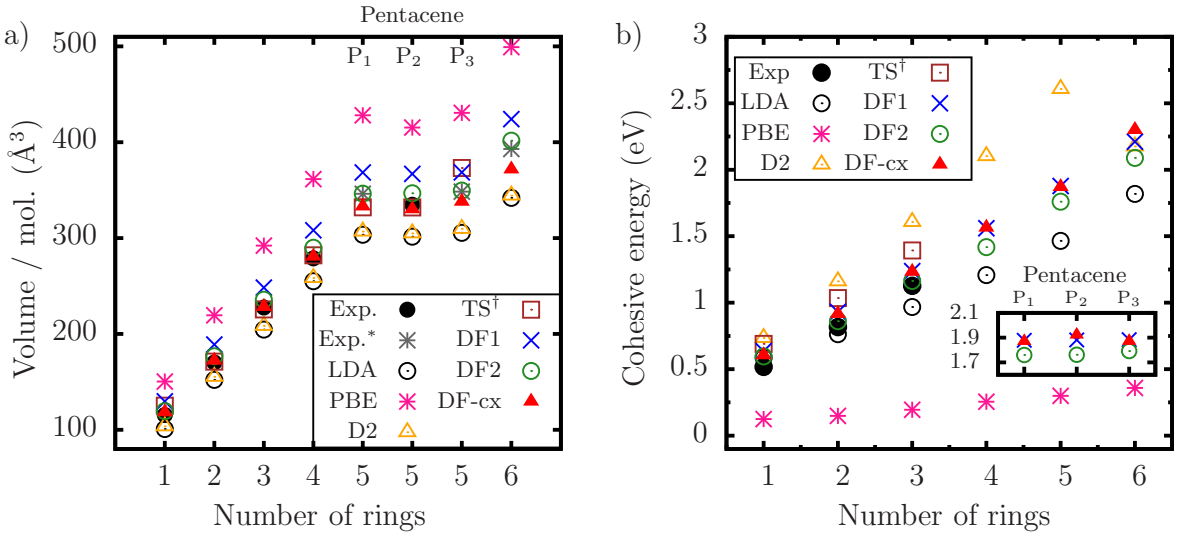

Figure 3.1: (a) Volume per molecule for the acene crystals, calculated using different approximations within DFT: LDA (black empty circles), PBE (pink stars), DF1 (blue crosses), DF2 (green empty circles), DF-cx (red filled triangles), PBE-D2 (orange empty triangles), and PBE-TS (brown squares). These are compared to low-temperature experimental data, for $T \geq 16\,\mathrm{K}$ from Refs. [187–189] and extrapolated to 0 K as indicated in Appendix A.2 (in black filled circles). For two pentacene polymorphs and hexacene, only experimental data at $T \geq 90\,\mathrm{K}$ is available [179, 190, 191] (in dark gray stars). (b) Cohesive energies E_{coh} for the acene series, obtained with the same set of approximations as in (a). Experimental E_{coh} (black filled circles) are obtained from enthalpies of sublimation ([192], see text). Inset: calculated E_{coh} for three pentacene polymorphs. † PBE-TS cohesive energies are taken from Ref. [90] and PBE-TS volumes from Refs. [89, 169].

eters obtained at room temperature. This is attributable to a cancellation of errors, as we model the structure at 0 K. Recent work [176] reported that a DF2 variant, called rev-vdW-DF2 [196], predicts lattice constants for benzene, naphthalene, and anthracene that are in remarkable agreement with low-temperature experiments (within 0.5%). For tetracene and P_2 pentacene, good agreement with room-temperature experiments is found [176], but the reported volumes overestimate structures extrapolated to 0 K by ∼2 % for pentacene P_2 and 8 % for tetracene.

For cohesive energies, Fig. 3.1(b) shows that neither DF2 nor DF-cx improve meaningfully upon DF1 cohesive energies. Specifically, the values obtained for DF2 are in excellent agreement (within 0.05 eV) with those reported in Ref. [169], as is the conclusion regarding lack of improvement over DF1. Interestingly, rev-vdW-DF2 reduces the error in cohesive energies with respect to experiments by half [176].

Turning to pairwise correction methods, Fig. 3.1(a) shows that lattice vectors calculated with D2 and TS corrections, added to underlying PBE calculations, are within 3 % and

1 % of experimental data, respectively, whereas cohesive energies are within 30 % to 40 % of experiment. Thus, they perform as well as DF methods in terms for geometries prediction but somewhat worse for cohesive energies.

To summarize, both the latest pairwise approaches and the latest DF methods can provide lattice parameters in outstanding agreement with experimental data (within ∼1 %) across the acene series, illustrating the predictive power of vdW methods and allowing for an excellent geometrical starting point for MBPT calculations. However, errors in cohesive energy are still on the order of 10 % to 30 %. In future work, it would be interesting to examine whether techniques which add nonlocality beyond pairwise interactions, particularly the many-body dispersion method [90, 174], can reduce the error in the cohesive energy.

3.2.2 Effects of structure on charged and neutral excitations

Having discussed the need for adequate treatment of vdW interactions for predicting geometry we now turn to the question of the sensitivity of the calculated excitations to structural parameters.

We start by considering charged excitations obtained within the *GW* approximations and assessing their dependence on the geometry obtained from LDA, GGA, the three van der Waals functionals (DF1, DF2, and DF-cx) used in section 3.2.1, and experiment. The **k**-point averaged G_0W_0-calculated fundamental gap Δ_g, along with the valence band width (vbw) and the conduction band width (cbw), for each of the geometries, is given in Table 3.1. (Here, the bandwidth is defined as the width in eV of the lowest π^* or highest π manifold of bands.) Hexacene is excluded here and below as G_0W_0 does not yield physically reasonable results. While we are not aware of an experimental fundamental gap value, the G_0W_0 value we compute is smaller than the singlet excitation energy calculated with BSE, and therefore certainly underestimates the fundamental gap. We attribute this mainly to a starting point issue, which can be overcome by using self-consistent *GW* (see Ref. [158]).

As shown in section 3.2.1, and in more detail in Appendix A.2, lattice parameters increase with functional in the following sequence: LDA/DF-cx/DF2/DF1/PBE. Interestingly, Table 3.1 shows that Δ_g follows the same trend, while vbw and cbw follow the opposite trend. These trends can be rationalized as follows: the larger the lattice parameters, the smaller the intermolecular hybridization and the smaller the bandwidth. Naturally, the smaller the hybridization, the larger the band gap. However, quantitatively the change in bandwidths explains only part of the gap increase with increasing lattice parameters. A second effect is that the solid-state gap is renormalized from the much larger molecular gap because the neighboring molecules serve as a dielectric medium whose response creates a polarization field that reduces the gap [198]. As discussed in detail in Refs. [81, 83, 86, 87], this phenomenon, which is well captured by *GW* calculations, itself depends on the unit-cell volume. This is because a larger intermolecular separation reduces the polarization field and therefore the renormalization, thereby increasing the gap.

Finally, we note that although the *GW* gaps calculated from the experimental geometries are within 0.1 eV (0.2 eV for benzene) of those obtained with DF2 lattice parameters, it

Table 3.1: Effect of structure on the **k**-point averaged fundamental gap Δ_g, along with the valence bandwidth (vbw) and the conduction bandwidth (cbw), all calculated in the G_0W_0 approximation. All values were obtained from lattice parameters fully relaxed within the LDA, PBE, DF1, DF2, and DF-cx functionals, as well as from experimental parameters [180, 187, 189, 190, 197]. All energies are in eV.

	G_0W_0 using lattice-parameters from						Exp.
	LDA	PBE	DF1	DF2	DF-cx	Exp.	
Benzene							
Δ_g	6.6	7.9	7.3	7.1	7.1	7.3	7.6-8.0
vbw	0.7	0.2	0.4	0.5	0.5	0.4	
cbw	0.7	0.4	0.5	0.5	0.5	0.5	
Naphthalene							
Δ_g	4.9	6.0	5.6	5.5	5.3	5.5	5.0-5.5
vbw	0.7	0.2	0.4	0.5	0.5	0.5	
cbw	0.7	0.2	0.3	0.3	0.4	0.3	
Anthracene							
Δ_g	3.6	4.5	4.3	4.1	4.0	4.0	3.9-4.2
vbw	0.6	0.2	0.3	0.4	0.4	0.3	
cbw	1.0	0.3	0.5	0.6	0.7	0.6	
Tetracene							
Δ_g	2.4	3.6	3.1	2.9	2.7	2.9	2.9-3.4
vbw	0.7	0.1	0.3	0.4	0.6	0.4	
cbw	0.9	0.3	0.5	0.7	0.8	0.7	
Pentacene P_3							
Δ_g	1.5	2.9	2.3	2.1	1.8	2.2	2.2-2.4
vbw	1.2	0.3	0.6	0.7	0.9	0.7	
cbw	1.1	0.3	0.6	0.7	0.9	0.7	

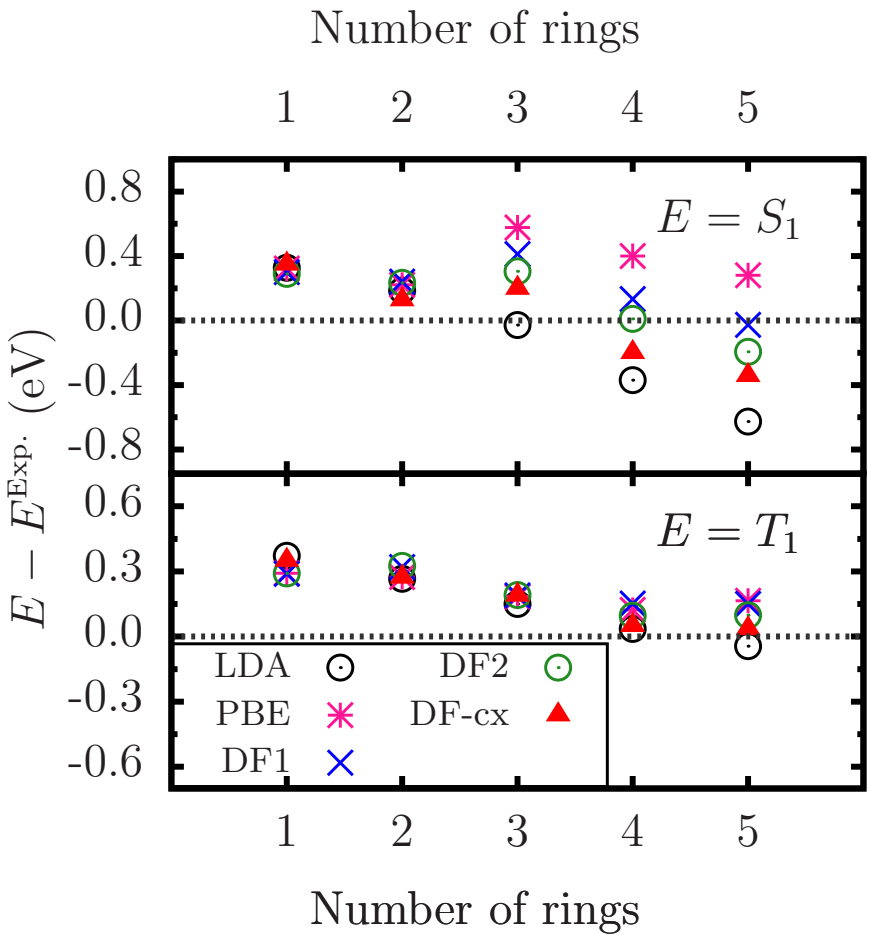

Figure 3.2: Effect of structure on the lowest singlet (S_1) and triplet (T_1) excitation energies, calculated in the G_0W_0-BSE approximation, given as deviation from experimental data taken from Refs. [199–205] and references therein. All computed values were obtained from lattice parameters fully relaxed within the LDA (black empty circles), PBE (pink stars), DF1 (blue crosses), DF2 (green empty squares), and DF-cx (red triangles) functionals, and are given as differences from experimental values. All energies are in eV.

should be taken into account that this is due to the accidental agreement of zero-temperature DF2 volumes with room-temperature experimental values (see section 3.2.1).

We now turn to the discussion of structure on neutral excitations. G_0W_0-BSE-calculated low-lying excitations, based on the same geometries used in Table 3.1 above, are given in Fig. 3.2 and in Table 3.2. Importantly, no significant temperature dependence of low-lying excitation energies is observed experimentally [206, 207], which facilitates the comparison to experimental excitation energies measured at higher temperatures.

Clearly, the dependence of T_1 excitation energies on geometry is quite minimal (± 0.1 eV at most across the entire acene series). The same is true for the S_1 excitations in the

Table 3.2: Effect of structure on the lowest singlet (S_1) and triplet (T_1) excitation energies, calculated in the G_0W_0-BSE approximation. All computed values were obtained from lattice parameters fully relaxed within the LDA, PBE, DF1, DF2, and DF-cx functionals, as well as from experimental values. All energies are in eV. For comparison, experimental values, taken from Refs. [199–205] and references therein, are also given. Also given are the mean absolute error (MAE) defined as $\sum_i^{N_m} |X_i - X_i^{\mathrm{Exp}}|/N_m$, with X_i being the excitation energy, the maximum absolute error (MAXE), and the mean absolute percentage error (MA%E) defined as $\sum_i^{N_m} |X_i - X_i^{\mathrm{Exp}}|/X_i^{\mathrm{Exp}}/N_m \times 100$.

		G_0W_0-BSE using lattice-parameters from						Exp.
		LDA	PBE	DF1	DF2	DF-cx	Exp.	
Benzene								
	S_1	5.1	5.0	5.0	5.0	5.0	5.0	4.7
	T_1	4.2	4.0	4.1	4.0	4.1	4.1	3.7
Naphthalene								
	S_1	4.1	4.2	4.2	4.2	4.1	4.2	3.9
	T_1	2.9	2.9	2.9	2.9	2.9	2.9	2.6
Anthracene								
	S_1	3.1	3.6	3.5	3.4	3.3	3.4	3.1
	T_1	2.0	2.0	2.1	2.0	2.0	2.0	1.9
Tetracene								
	S_1	2.0	2.9	2.5	2.4	2.2	2.4	2.4
	T_1	1.3	1.4	1.4	1.4	1.3	1.4	1.3
Pentacene P_3								
	S_1	1.3	2.1	1.9	1.7	1.5	1.7	1.9
	T_1	0.8	0.9	0.9	0.9	0.8	0.9	0.9
S_1	MAE	0.3	0.4	0.2	0.2	0.3	0.2	
	MA%E	12	12	7	7	10	7	
	MAXE	0.6	0.5	0.4	0.3	0.4	0.4	
T_1	MAE	0.2	0.2	0.2	0.2	0.2	0.2	
	MA%E	8	9	10	7	6	8	
	MAXE	0.5	0.4	0.4	0.3	0.4	0.4	

smaller acenes (benzene and naphthalene), but the dependence on geometry increases with acene size. For pentacene, it is already quite significant, with the S_1 excitation values changing by 0.9 eV by switching from the LDA to the PBE geometry. As before, agreement with experiment is much improved by using DF-based geometry, with best results obtained using DF2 and DF-cx (with differences between the two being too small to be physically meaningful), based on which S_1 energies are found to be within 4–5 % of experimental values. The remaining discrepancy may be due to terms not included in these calculations, such as zero-point and finite-temperature effects associated with lattice vibrations, as well as the remaining limitations of the GW-BSE approach in general and its approximations used here in particular.

The sensitivity of excitation energies to geometry, or lack thereof, is directly related to the degree of spatial localization of these states. For large acenes, notably pentacene, singlet states have been shown to extend over several molecules [77, 84, 85, 200, 208]. The degree of delocalization is larger for smaller unit-cell volumes, an effect related to the increased intermolecular hybridization [209]. Delocalization decreases the excitation energy, which is therefore larger the smaller the unit cell is. For short acenes, this is a much smaller effect and indeed no significant structure dependence is observed. Triplets, however, are always predominantly localized on a single monomer [208, 209], explaining their weak dependence on the geometry.

Finally, we note that the calculated neutral excitation energies are not strongly affected by temperature, at least as reflected by the crystal structure used in our calculations. For benzene, naphthalene, and anthracene, the calculated singlet and triplet energies do not depend significantly on geometry. For the larger acenes, singlet energies change by at most 0.15 eV, while triplet energies change by even less, when varying the volume by ∼3 % (similar to thermal expansion at room temperature). This agrees with the experimentally observed absence of significant temperature dependence of low-lying excitation energies [206, 207].

3.3 Conclusion

In summary, we have studied the structure and the effects of structure on the excited-state properties of the series of acene-based crystals, from benzene to hexacene, from first-principles using vdW-corrected DFT and MBPT. Both vdW-DF and pairwise correction methods were found to predict lattice parameters in excellent agreement with experimental data. We find that DF1 overestimates volumes but DF2 improves over DF1, consistent with the general trends for these functionals. DF-cx further improves lattice parameters, with a residual discrepancy of >1 %. Furthermore, the relatively simple TS pairwise approach performs as well as the best DF methods.

For acenes in the solid state, charged excitations are generally well described by the G_0W_0 method, but partial self-consistency, in the form of the eigenvalue–self-consistent GW method, is needed for hexacene, likely owing to the PBE starting point employed in this study. The results are found to be sensitive to the geometry used owing to a combination

of intermolecular hybridization and polarization-induced level renormalization. Neutral low-lying singlet and triplet excitation energies are generally well described using the G_0W_0-BSE method. They are generally less sensitive to structure, except for the important case of singlet excitations in larger acenes. There, large structural sensitivity is found owing to significant delocalization of the singlet state.

The results in this chapter reveal the importance of an accurate account of dispersive interactions as a prerequisite to predictive calculations of excited-state properties in the acene crystals. Furthermore, we laid out routes for predictive calculations, in which both structures and excited states are calculated entirely from first principles, for broader classes of molecular solids. Lastly, the remaining discrepancies with experiment and sensitivity to structural parameters suggest that zero-point and finite-temperature effects from electron-phonon coupling could have significant contributions to the excited states. We explore phonons in the following Chapter 4, and their coupling to electronic states in Chapter 5 on the example of naphthalene.

Chapter 4

Lattice vibrations of naphthalene

The work presented in this chapter has been published as Ref. [210].

Phonon scattering can be an important facilitator and dissipation mechanism in charge separation and carrier transport processes. In this chapter, we carry out density functional theory (DFT) calculations of the structure and the full phonon dispersion of crystalline naphthalene, a well-characterized acene crystal for which detailed neutron-diffraction measurements, as well as infrared and Raman spectroscopy, are available. We evaluate the performance, relative to experiments, of DFT within the local density approximation (LDA); the generalized gradient approximation of Perdew, Burke, and Ernzerhof (PBE); and a recent van der Waals (vdW)–corrected nonlocal correlation (vdW-DF-cx) functional. We find that the vdW-DF-cx functional accurately predicts lattice parameters of naphthalene within 1 %. Intermolecular and intramolecular phonon frequencies across the Brillouin zone are reproduced within 7.8 % and 1 %, respectively. As expected, LDA (PBE) underestimates (overestimates) the lattice parameters and overestimates (underestimates) phonon frequencies, demonstrating their shortcomings for predictive calculations of weakly bound materials. If the unit cell is fixed to the experimental lattice parameters, PBE is shown to lead to improved phonon frequencies. This study provides a detailed understanding of the phonon spectrum of naphthalene, and highlights the importance of including vdW dispersion interactions in predictive calculations of phonon frequencies of molecular crystals and related organic materials.

4.1 Introduction

Organic materials based on small molecules have shown great promise for optoelectronic applications due to high electron mobilities [5, 34–37] and favorable energetics that can lead to efficient singlet fission [2, 3, 6–8, 211], among others. However, despite significant promise, understanding and control of the underlying mechanisms is still lacking [28, 37]. As those processes are often subject to scattering from phonons, leading to phonon-assisted transport and dissipation [37, 212], for example, a detailed, quantitative understanding of the

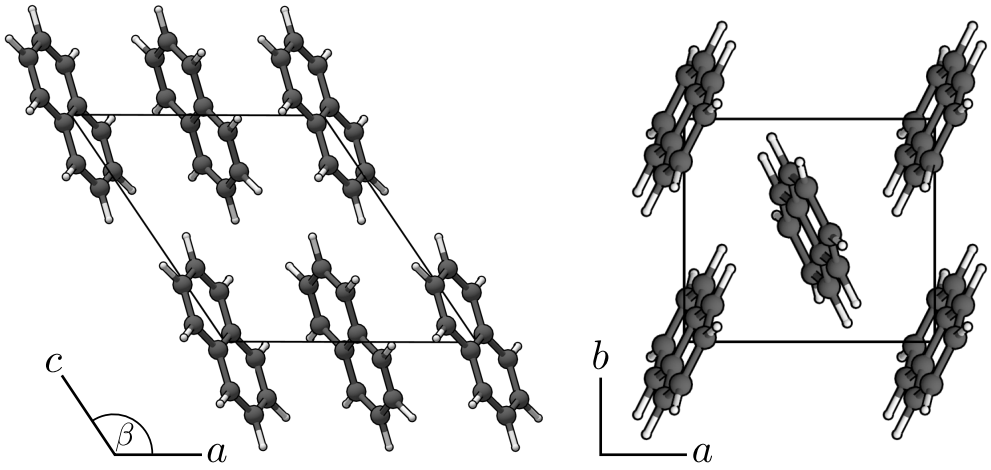

Figure 4.1: Naphthalene is the smallest acene that crystallizes in a herringbone structure. There are two molecules in the monoclinic unit cell with space group $P2_1/a$, each situated at inversion centers.

vibrational spectra—and in particular, the phonon spectra of extended molecular crystals—is integral to future efforts to better harness these materials for optoelectronic applications. Prior *ab initio* studies of organic crystals, based on DFT and many-body perturbation theory, have focused predominately on electronic and optical properties [77–88]. Such excited-state properties are sensitive to local geometry and molecular packing, as seen in Chapter 3, and a principal challenge to theory is that long-range dispersive vdW-type interactions play a significantly larger role for the cohesive energies (and therefore the geometries) of sparse molecular crystals compared to their inorganic counterparts [82, 166, 172].

Among molecular crystals, the acene family is well-suited for detailed study of vibrational and optoelectronic phenomena. Their relatively simple molecular and crystal structures—and variable size range, from benzene to hexacene—has facilitated significant experimental as well as computational investigation of the phonon spectra. Naphthalene is the smallest monomer member with the herringbone crystal structure, typical of acenes (Fig. 4.1). Further, there is a plethora of experimental vibrational spectra available for both gas and solid crystalline phase, allowing a detailed comparison between calculated and experimental values. The first extensive Raman and infrared (IR) studies of solid naphthalene were reported by Nedungadi [213] and Pimentel and McClellan [214]. Since then, numerous experiments have been performed to understand and assign the vibrational spectra [215–224], in particular Natkaniec et al. [219], who used coherent inelastic neutron scattering to map out phonon dispersion curves of deuterated naphthalene along several directions in the Brillouin zone.

Prior computational work on the phonon spectrum of solid naphthalene used semi-empirical force-field methods, with parameters fit from experiments, for generation of both zone center frequencies [225–229] and wave vector-dependent dispersion [218, 230–233], greatly aiding in the interpretation of the naphthalene phonon spectra. More recently,

the vibrational modes of gas-phase naphthalene—in particular, infrared and Raman active modes—as well as the zone-center modes of crystalline naphthalene have also been reproduced successfully with *ab initio* methods [223, 229, 234–238], although the mode assignments depend somewhat on the level of theory and functional [223, 238]. Finally, Schatschneider et al. [89] and Reilly and Tkatchenko [90] used vdW-corrected DFT to obtain the zero-point energy and vibrational contribution (integrated over the Brillouin zone) to the lattice energy of several acenes, respectively, using the Tkatchenko-Scheffler pairwise approach; however, these studies did not provide any details of the phonon spectrum.

Two *ab initio* phonon band structures of acene crystals have been reported prior to the publication of this work [91, 92]. The full phonon dispersion of tetracene has recently been calculated using the local density approximation (LDA), capitalizing on the tendency of LDA to overbind to partially compensate for the lack of vdW-corrections [92]. Band structures of solid naphthalene calculated at different pressures have been presented by Fedorov et al. [91] using the DFT-D3 approach [121] but without any detailed comparison with experiment. Considering the fundamental importance of phonons in organic crystals, there remains a need to assess and understand the efficacy of existing approaches for calculating phonon dispersions over the entire Brillouin zone in vdW-bound solids, particularly in the context of a well-characterized system such as naphthalene.

In this chapter, we compute the phonon dispersion of solid naphthalene within DFT using LDA, the generalized gradient approximation of Perdew, Burke, and Ernzerhof (PBE), and the recently developed nonlocal density functional vdW-DF-cx [131]. We provide the first detailed comparison between computed and measured phonon spectrum of a molecular crystal across the Brillouin zone, assessing our results against neutron scattering experiments on perdeuterated naphthalene, as well as IR and Raman spectra of solid perprotonated naphthalene. In addition to yielding excellent lattice parameters as shown in Chapter 3, the results in this chapter show that vdW-DF-cx is able to reproduce the full experimental phonon dispersion with high accuracy. Lacking any long-range correlation, PBE overestimates the unit cell volume by 29 %, and, as a result, significantly underestimates phonon frequencies relative to experiment. Notably, upon constraining the lattice parameters to experimental values, PBE yields good agreement, suggesting that it may reproduce phonon spectra for other organic crystals with known experimental geometry. LDA, in contrast, overbinds the naphthalene crystal as expected, resulting in a primitive cell volume that is 10 % smaller than experiment and significantly overestimated phonon frequencies.

4.2 Results and discussion

4.2.1 Lattice parameters

We calculate and compare the phonon dispersion using the three functionals, LDA, PBE, and PBE-vdW-DF-cx. For relaxed lattice parameters of all three functionals we use the values obtained in Chapter 3, which are given again in Table 4.1 for reference. We distinguish

Table 4.1: Experimental and calculated lattice parameters for naphthalene [158]. Lattice constants a, b, c are in Å, unit cell volume Ω in Å^3, and angle β in degrees.

	Exp. [181]	DF-cx	LDA	PBE
a	8.08	8.06	7.74	9.13
b	5.93	5.91	5.76	6.31
c	8.63	8.75	8.37	8.99
β	124.7	124.4	125.5	122.1
Ω	340.4	344.4	304.0	438.9

phonon frequencies obtained at experimental and relaxed lattice parameters by denoting results using experimental lattice parameters with "@Ω_{exp}", lattice parameters relaxed with LDA with "@Ω_{LDA}", etc.

4.2.2 Intermolecular modes

We divide the discussion of our results into two parts. In this section, we first discuss the intermolecular modes at lower frequency, comparing the performance of different density functionals to experiment. Then in section 4.2.3, we concentrate our analysis on the intramolecular modes at higher frequencies calculated with DF-cx and compare our results to IR and Raman measurements. In accord with prior work [91, 219, 229], we find that the phonon band structure shows a gap of roughly 40 cm^{-1} between the intermolecular and intramolecular modes. While we do confirm the observation of Coropceanu et al. [229] that all translational modes show slight internal bending motion, the mixing between inter- and intramolecular modes is very small and can be neglected for the purpose of classification.

In Fig. 4.2 we show the phonon band structures of d8-naphthalene, in an energy window below 150 cm^{-1} focused on the intermolecular modes, calculated with the vdW-nonlocal functional DF-cx, and with LDA and PBE. Given that PBE leads to a large overestimate of the lattice parameters, we only provide the phonon dispersion for PBE calculated by constraining the lattice parameters to those of experiment. (Here, the designation "d8-naphthalene" refers to the fact that all eight of nuclei associated with the eight hydrogen atoms on each naphthalene molecule consist of both a proton and a neutron; "d0-naphthalene" refers to all hydrogen nuclei consisting of a single proton.) The results are compared to experimental data obtained by neutron scattering of d8-naphthalene at 6 K [219].

At first glance, all three functionals reproduce the experimental curves quite well. The mean absolute percent deviation from experimental data points is 7.8 % for DF-cx, 5.8 % for PBE (at the experimental geometry), and 12.3 % for LDA. These results are consistent with prior reports that PBE at experimental lattice parameters and LDA with relaxed parameters

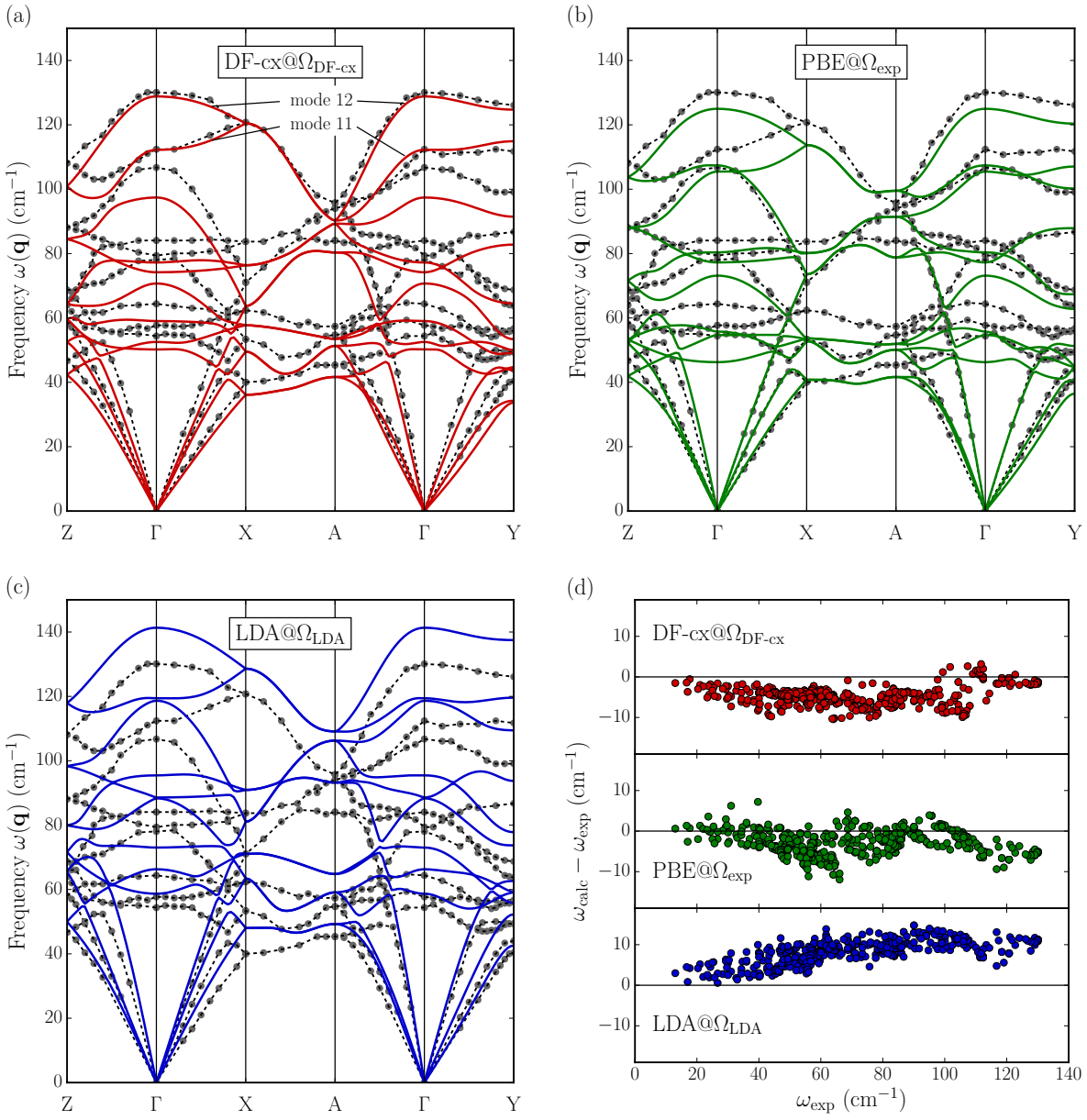

Figure 4.2: Calculated phonon dispersion (solid lines), shown and analyzed in a frequency range dominated by intermolecular modes, and compared with neutron scattering experiments of d8-naphthalene at 6 K [219] (grey circles; dashed lines to guide the eye). While DF-cx@$\Omega_{\text{DF-cx}}$ (a) and LDA@Ω_{LDA} (c) use optimized lattice parameters, PBE@Ω_{exp} results are (b) shown as computed with experimental parameters. The level agreement is quantified by plotting the difference between the calculated and the experimental values as a function of the latter (d). For the intermolecular modes DF-cx@$\Omega_{\text{DF-cx}}$ shows a mean absolute percent deviation of 7.8 %, PBE@Ω_{exp} 5.8 %, and LDA@Ω_{LDA} 12.3 %.

Table 4.2: Intermolecular mode frequencies of d8-naphthalene at Γ. Experimental values are taken from neutron scattering experiments and compared to frequencies calculated with DF-cx, PBE, and LDA using experimental as well as relaxed lattice parameters (all values in cm^{-1}). Modes are ordered to best correspond to the symmetries reported experimentally. Mean absolute error (MAE) in cm^{-1} and mean absolute percent error (MA%E) are also given.

mode	symmetry (type)	Exp. [219]	DF-cx		LDA		PBE	
			$@\Omega_{\text{DF-cx}}$	$@\Omega_{\text{exp}}$	$@\Omega_{\text{LDA}}$	$@\Omega_{\text{exp}}$	$@\Omega_{\text{PBE}}$	$@\Omega_{\text{exp}}$
4	B_g (libr.)	54.37	50.20	54.27	58.69	23.90	18.88	46.26
5	A_u (trans.)	57.71	52.54	55.08	66.29	49.39	25.90	55.75
6	A_g (libr.)	64.38	59.03	68.08	73.02	43.74	21.09	54.68
7	B_u (trans.)	78.05	70.70	71.43	88.32	65.20	49.03	73.14
8	B_g (libr.)	79.39	74.19	80.64	88.58	54.90	43.04	77.25
9	A_g (libr.)	84.06	77.23	83.51	95.46	57.31	45.30	80.37
10	A_u (trans.)	106.74	97.42	99.33	118.65	75.32	47.78	107.39
11	A_g (libr.)	112.41	112.23	112.02	119.42	76.09	38.67	105.48
12	B_g (libr.)	130.09	128.83	130.55	141.33	94.93	48.72	124.98
MAE			4.83	2.37	9.52	27.18	51.28	4.41
MA%E			5.96	2.77	10.84	30.13	55.38	5.37

can yield good agreement for naphthalene (at the zone center) and tetracene (throughout the zone), respectively [92, 229].

A major drawback of the PBE functional for naphthalene is that it requires prior knowledge of the experimental lattice parameters. If the naphthalene unit cell is optimized with PBE, the calculated volume is overestimated by 29 % (Table 4.1). Similar overestimates have been noted by Byrd et al. [239] for more polar molecular crystals. The calculated frequencies at this grossly overestimated volume decrease dramatically, as can be seen in Table 4.2. Thus, using PBE to calculate phonon frequencies of organic crystals can only be efficacious for systems with known lattice parameters.

Despite being a purely local functional, LDA is known to lead to lattice parameters in agreement with experiment for certain vdW materials due to a cancellation of errors [193, 194]. For naphthalene, the cancellation is apparently incomplete and the LDA optimized unit cell volume is 10 % smaller than experiment (Table 4.1), a significant underestimate that leads in turn to an overestimate of the phonon frequencies. Thus, in general, the LDA is insufficient for quantitative prediction of phonon band structures of vdW bound

organic crystals. Interestingly, and unlike PBE, using experimental lattice parameters with LDA results in frequencies far below the experimental values (Table 4.2). Evidently, the PBE gradient corrections restore repulsive short-range intermolecular interactions missing in LDA, leading to agreement with experiment at the experimental lattice parameters.

DF-cx, on the other hand, predicts the naphthalene unit cell volume within 1 % [158] while reproducing the experimental intermolecular frequencies within 7.8 %. Although the total deviation is slightly larger than for PBE, the scatterplot in Fig. 4.2 shows that the DF-cx frequencies below 100 cm^{-1} are shifted by a more or less constant factor, while PBE errors are more randomly distributed over the range of intermolecular modes, indicating that DF-cx reproduces the qualitative structure of the phonon dispersion much better.

This superior performance of DF-cx for phonons is further evident when comparing the calculated bandwidths of the two lowest optical bands. While PBE and LDA display a pronounced minimum and maximum for the first and second optical bands centered on Γ along Z → Γ → X, DF-cx reproduces the saddle point-like dispersion reported in experiment. Additionally, along the high-symmetry line X → A, the slope of the lowest band calculated with DF-cx matches the experimental spectrum, whereas both PBE and LDA, incorrectly, predict a minimum. Clearly these soft intermolecular modes, where the influence of nonlocal vdW dispersive forces would be expected to be most significant, have the largest dependence on the chosen functional, and LDA and PBE exhibit the largest discrepancies. Overall, DF-cx, which accounts for vdW-dispersion forces, is more predictive and performs significantly better than either PBE or LDA for these low-lying naphthalene intermolecular modes across the Brillouin zone.

We now comment further on the systematic underestimation of the frequencies of the first ten bands for DF-cx. If this were simply due to an overall underestimate of intermolecular forces, we would expect all frequencies to be uniformly red-shifted. However, the two highest bands (modes 11 and 12) along Γ → X and along Γ → Y show excellent agreement (see Fig. 4.2). What distinguishes these two modes from the others? These are librational modes with the libration axes roughly along the length of the molecules and parallel to the *c*-axis. (See Fig. 4.3 for a visualization of the displacement vectors at Γ.) The nature of the libration in modes 11 and 12 is such that the atom-atom distances between molecular layers remain relatively constant compared to the other modes. The two modes are thus dominated by interactions within the *ab*-plane. Now, if we inspect the lattice parameters in Table 4.1 more closely, we see that the 1 % volume difference is mainly caused by an elongated *c*-axis, while *a* and *b* are much closer to experimental values. The longer *c*-axis results in weaker interactions along that direction and overall lower frequencies for displacements with largest amplitudes between layers, explaining the different behavior of modes 11 and 12 (which have minimal amplitude along *c*) compared to the rest.

Further support for this explanation can be found at the high-symmetry points Z and A, where DF-cx underestimates the frequencies of the two highest intermolecular mode bands relative to experiment. The coupling of those two modes at Z leads to a shift of the rotational axes to the edge of the molecule. The displacement pattern associated with these modes could be described as a flapping motion, similar to a flag on a pole in the wind, and leads to

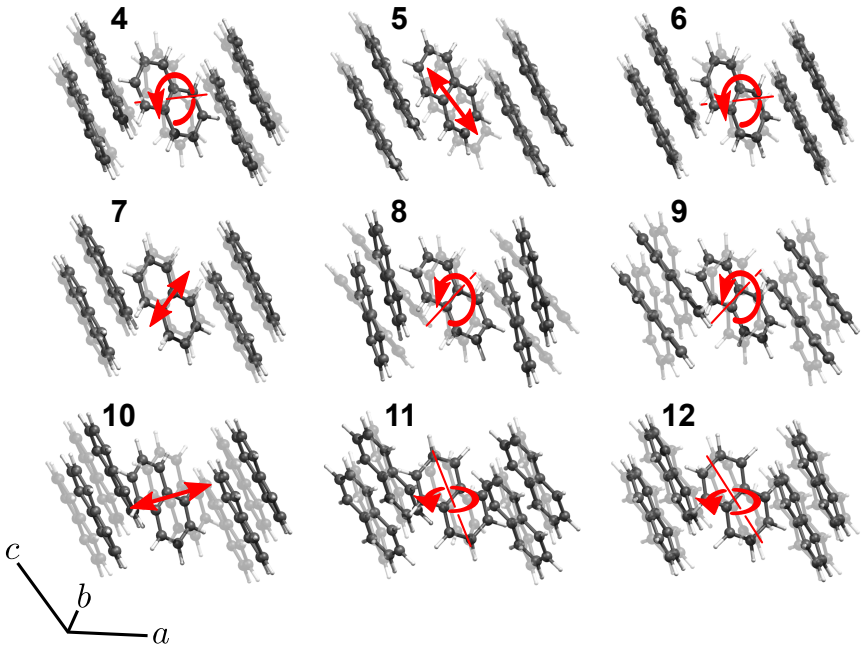

Figure 4.3: The nine intermolecular optical modes of crystalline naphthalene. Modes 5, 7, and 10 are translational modes roughly parallel to c, b, and a respectively. The other modes are librational modes with rotational axes roughly along a (4, 6), b (8, 9), and c (11, 12).

atomic displacements much further into the interlayer gap (and heightened sensitivity to c). In contrast, at X, the rotational axes remain centered on the molecules, and these calculated frequencies exhibit the same excellent agreement with experiment as observed at Γ. Finally, at the high-symmetry point A, we observe near-degeneracy between the four modes 9-12. The mixing between the two librational modes 11 and 12 with the translational mode 10 along a, and a librational mode with rotation axes along b, again leads to mode displacement patterns with higher amplitudes between molecular layers and an underestimate relative to experiment. In sum, we can associate the underestimation of frequencies of many of the intermolecular modes by DF-cx directly to the overestimate of the c-axis parameter relative to experiment.

We can quantify this analysis further by comparing the frequencies calculated with experimental lattice parameters (DF-cx@Ω_{exp}) to the corresponding frequencies of DF-cx@$\Omega_{\text{DF-cx}}$. Indeed, most zone center frequencies are shifted upwards to give much better agreement with experiment, as can also be seen by the much-improved mean average and percent deviation (Table 4.2). The mode frequencies are notably sensitive to a small a change in lattice parameters, essentially 1 % along one axis. For example, in case of mode 6 we get an increase of 15 %, and overall decrease the mean percent deviation by more than a factor of two.

We note that the frequencies of mode 7 and 10, translational modes along the b and a axes, respectively, are largely unaffected by the change in lattice parameters, and continue

to deviate from experiment in both cases by 7–10 %. This remaining disagreement with experiment may at least partially be associated with limitations of DF-cx. In addition, there are still uncertainties regarding experimental and calculated lattice parameters. The crystals used in the neutron diffraction experiments (d8-naphthalene) might exhibit small differences from the d0-naphthalene structure measured by Capelli et al. [187], which we use in this work. In fact, d8-naphthalene is known to exhibit small quantitative differences in lattice parameters relative to its perprotonated counterpart, resulting in a difference in volume of about 0.5 % at room temperature [240, 241]. As this volume difference might be a finite-temperature effect, its implications are not directly transferable to our low temperature study, though. On the other hand, our calculated relaxed lattice parameters do not take into account finite-temperature effects or zero-point anharmonic expansion, which could increase the calculated cell volume even at 0 K [242–244]. Considering the impact on the phonon dispersion caused by the ∼1 % change in volume, as shown above, such small differences in cell volume could account for the remaining discrepancies between DF-cx and experiment.

In conclusion, accurate determination of lattice parameters is central for the *ab initio* calculation of intermolecular phonon frequencies in vdW-bound crystals. As we have shown, DF-cx outperforms the conventional functionals LDA and PBE, and is able to reproduce qualitatively and quantitatively the dispersion of intermolecular modes across the Brillouin zone of solid naphthalene.

4.2.3 Intramolecular modes

We now turn our discussion to the intramolecular modes above 150 cm^{-1}. The three functionals used here give very similar internal coordinates, within 0.015 Å, or 1 % for bond lengths and 0.3°, or 0.2 % for angles (see Table B.1 in the Appendix for all relaxed coordinates). As a result, all functionals predict very similar frequencies for intramolecular modes, agreeing to within 2.5 % (Table B.2 and Fig. B.1 in the Appendix); in contrast, intermolecular frequencies (discussed above) differed from DF-cx by 6.3 % to 25 % for LDA, and 2.9 % to 10 % for PBE. Thus, in what follows, we limit ourselves to the analysis of DF-cx results. In order to compare with experiments on d0-naphthalene, we present both deuterated and non-deuterated naphthalene results. Figure 4.4 shows both full isotopic band structures side by side for comparison. To illustrate the isotope shifts of individual modes, we connect the frequencies corresponding to the two eigenvectors with the largest projection with black lines. For all frequencies and corresponding shifts see Table B.3 in the Appendix.

Interestingly, hydrogenation leads to isotope shifts $\omega_\mathrm{H}/\omega_\mathrm{D}$ with a rather large spread, from 0.998 to 1.394, and results in considerable reordering of the normal modes. Notably, for the two C-C stretch modes at around 1390 cm^{-1}, we predict a rather unexpected decrease in frequency by about 3 cm^{-1} for d0- compared to d8-naphthalene. This can be explained by additional strain on the bond angles, as the more inert deuterium atoms do not displace as much with the carbon atoms. The modified displacement pattern leads to an effective increase in the force constant which more than negates the effect of the higher mass. Additionally, the almost constant shift of 1.35 for all high-frequency C-H stretch modes at around

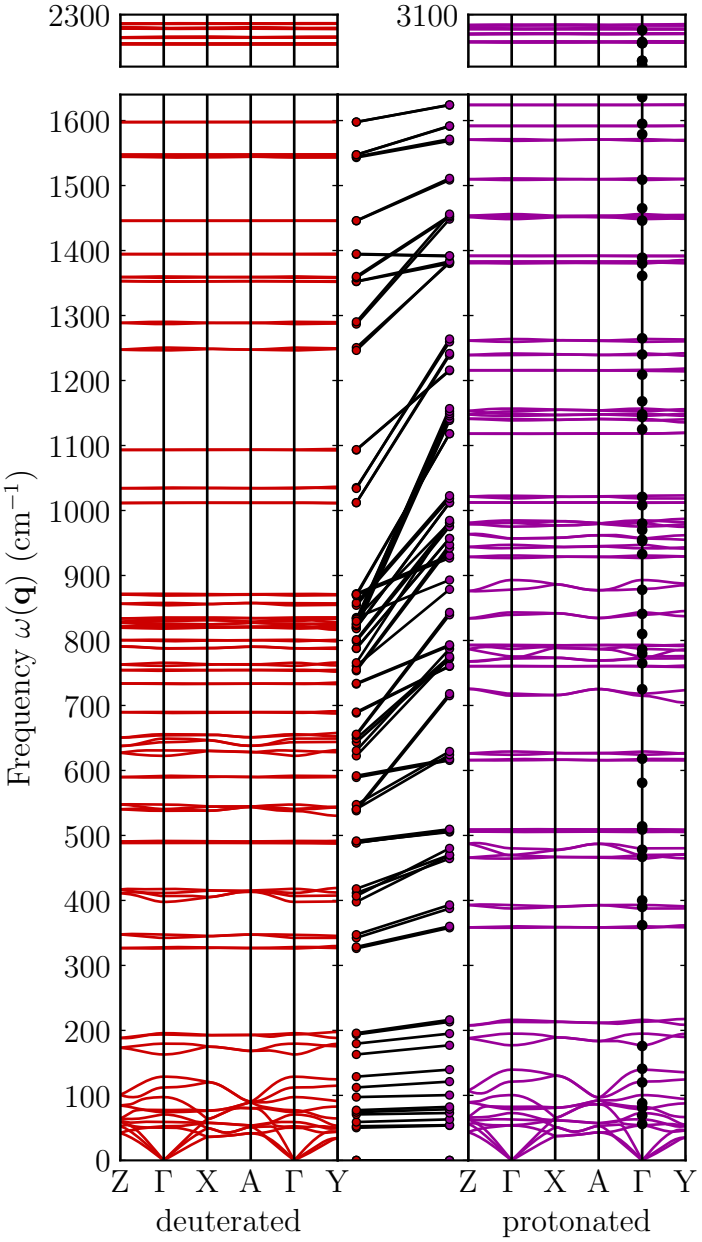

Figure 4.4: Comparison between phonon dispersion curves calculated with DF-cx of d8- and d0-naphthalene. The black lines in the center illustrate the shift of zone center frequencies (dots) by connecting the two modes with the highest projection between eigenvectors. The black circles along Γ in the perprotonated spectrum on the right are experimental IR and Raman frequencies of solid naphthalene [216]. The intermolecular frequencies below 150 cm^{-1} were measured at 4 K, the intramolecular frequencies at room temperature. For the distinction between IR and Raman active modes, see Table B.2.

$2275\,\mathrm{cm}^{-1}$ and $3075\,\mathrm{cm}^{-1}$, respectively, corresponds almost exactly to the expected shift of $\sqrt{m_\mathrm{D}/m_\mathrm{H}} = 1.36$.

Finally, we compare calculated DF-cx zone-center frequencies of d0-naphthalene with experimental IR and Raman frequencies measured and reported by Suzuki et al. [216]. (All frequencies are listed in Table B.2 in the Appendix. For visual comparison, we indicate the experimental values with black circles along the Γ-point in the spectrum in Fig. 4.4). Overall, the agreement between theory and experiment is excellent, resulting in a mean absolute deviation of 1 %. Discrepancies between experimental and calculated values can have several origins. The IR and Raman measurements were performed at room temperature, which lead to increased anharmonic contributions, generally lowering the measured frequencies relative to those computed within a harmonic approximation. Another complication is the assignment of experimental frequencies. Overtones and combination bands in a dense spectrum may be challenging to distinguish from fundamental frequencies. This can obfuscate mode assignments, as can be nicely seen in the large table assembled by Lielmezs et al. [221]. To help with the future comparison with these data, we list all calculated frequencies and their respective symmetries in the Appendix in Table B.2.

4.3 Summary and outlook

In this chapter, we calculated the full phonon dispersion of d8- and d0-naphthalene with density functional theory. We evaluated results obtained with three different density functionals, namely LDA, PBE, and vdW-DF-cx. Comparing the resulting dispersion of the intermolecular modes to the experimental data obtained with neutron scattering, we highlighted the necessity of using a vdW-corrected approach to accurately predict the phonon spectrum. More specifically, we find that PBE fails to predict bulk lattice parameters for naphthalene that result in reasonable frequencies relative to experiment. However, using experimental lattice parameters, PBE can lead to relatively accurate phonon dispersion (although qualitative discrepancies remain for intermolecular modes). LDA underestimates the unit cell by 10 % and consistently overestimates the frequencies; unlike PBE, LDA performs significantly worse at experimental lattice parameters. DF-cx, on the other hand, captures both the ground-state geometry of the crystal as well as the phonon dispersion, both quantitatively and qualitatively. The small discrepancies with respect to experiment are likely due to modest differences between the predicted lattice parameters and experiments, as well as any differences between the experimental structures of d0- and d8-naphthalene.

Further, we presented calculations of the full phonon dispersion of both d8- and d0-naphthalene, and compared the **Γ**-point frequencies of d0-naphthalene to experimental values obtained by IR and Raman spectroscopy. Being less sensitive to long-range intermolecular interactions and lattice parameters, excellent agreement with intramolecular mode frequencies was obtained by all three functionals.

This study demonstrates that including vdW interactions in the functional is crucial in order to obtain predictive structural and vibrational properties for weakly-bound organic

crystals and related materials like naphthalene. DF-cx, while already performing well, is only one of many existing and potential vdW approaches, and crystalline naphthalene is one of the simplest organic crystals. Our study provides further insight into the vibrational properties of these materials across the Brillouin zone, and is a starting point for benchmarking other vdW methods with naphthalene and known molecular crystals. Lastly, the good agreement with experiment also validates the use of the harmonic approximation for the phonon calculation, and sets the stage for the calculation of the electron-phonon coupling in the next chapter.

Chapter 5

Band-gap renormalization, carrier mobilities, and the nature of electron-phonon coupling in naphthalene

Organic molecular crystals feature strong electron-phonon interactions which are expected to be crucial in determining their electronic properties at zero and finite temperature. In this chapter we summarize our first principles calculations based on density functional theory (DFT) of the electron-phonon interaction in naphthalene crystals, and the contributions of phonons to the renormalization and temperature dependence of the fundamental band gap, and the resulting scattering lifetimes of electronic states near the band edges. The phonon renormalization of the GW-corrected band structure predicts a fundamental band gap of 5 eV for naphthalene at room temperature, in good agreement with experiments. From our calculated phonon scattering lifetimes of the electronic states, we obtain the temperature-dependent electrical mobilities of electrons and holes which are in good agreement with experimental measurements at room temperatures. Finally, we present an energy self-consistent computational scheme for the electron-phonon self-energy, which leads to the formation of strong satellite bands in the electronic band structure. We show that a one-shot calculation of the self-energy can reproduce the self-consistent scheme, if the on-the-mass-shell approximation is used, i.e., if the self-energy is evaluated at the bare DFT energies.

5.1 Introduction

Much attention has been drawn to the effect of electron-phonon coupling (EPC) on the electronic and transport properties of molecular materials [101, 103, 245]. Along with contributions from the lattice expansion and disorder, the EPC is responsible for the temperature-

dependent renormalization of the electronic energies. It also generates scattering and decay channels that result in finite lifetimes for electronic states and limits charge carrier mobilities. The finite lifetimes result in a broadening of the electronic bands that can be seen in photoemission spectroscopy.

The vast majority of prior theoretical studies of temperature effects in organic crystals focus on the electronic lifetimes and use various approaches to calculate the mobilities [38, 93–95, 97–106, 109]. Fully *ab initio* studies that explicitly calculate the renormalization of solids are usually limited to few-atom systems [149, 150, 246–249], or small molecules [108]; these methods have not been applied to larger-molecule structures like naphthalene. One study that calculated both the broadening and renormalization of pentacene crystals, used a tight-binding model parametrized by many-body perturbation theory (MBPT) calculations [250]. The study reported unusual quasi-discontinuities in the band structure caused by EPC that have been corroborated by experimental results, showing "kinks" in the electronic dispersion [250, 251]. In another study, Vukmirović et al. [107] evaluated the EPC matrix elements for two pairs of bands in naphthalene using first-principles methods. They found weak EPC, validating the use of second order perturbation theory (a claim that we challenge), and strengthening the argument for band-like charge carrier transport. Lee et al. [109] use an approach within the same theoretical framework as applied here to calculate the temperature-dependent hole mobility.

In this chapter, we compute from first principles the temperature dependence of the electronic structure and transport properties of naphthalene crystals. We use the dynamical Allen-Heine-Cardona theory to compute both the real and imaginary parts of the electron-phonon coupling self-energy. With this quantity, we can predict the temperature renormalization of the band gap, and obtain the hole and electron mobilities within the self-energy relaxation-time approximation. We discuss the details of the calculated frequency-dependent self-energy, and identify features that should apply to other molecular solids, such as the approximate independence of the self-energy on the electron wave vector $\mathbf{k}$. We find that in naphthalene, the band dispersion, phonon frequencies, and the renormalization energies are of the same order of magnitude, which challenges the validity of perturbation theory in this system. We address this issue by exploring a self-consistent computational scheme for the self-energy, and show that a single calculation of the self-energy can reproduce the self-consistent results of the band gap renormalization and electrical mobilities, provided that the on-the-mass-shell approximation is used, i.e., if the self-energy is evaluated at the bare eigenvalues.

5.2 Results and discussion

5.2.1 Lattice parameters

As discussed in previous chapters, relaxing lattice parameters and atomic coordinates with van der Waals corrected functionals or pair-wise dispersion corrections results in excellent

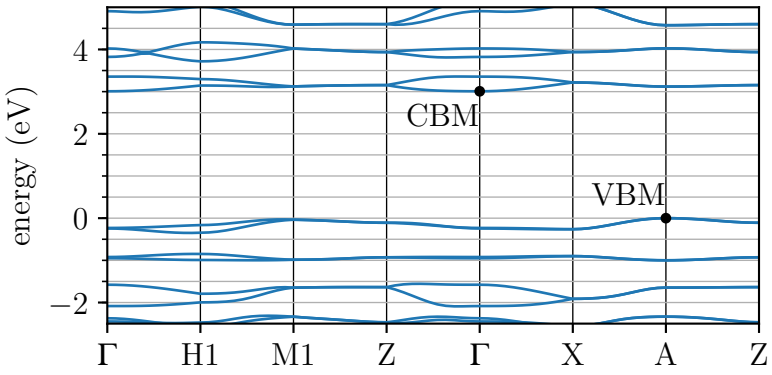

Figure 5.1: Electronic band structure of naphthalene calculated with DFT. The locations of the conduction band minimum (CBM) and valence band maximum (VBM) are indicated with black dots.

agreement with low-temperature experiments. Here we use the Grimme D3 pair-wise vdW correction method [121, 124] with PBE, which results in a relaxed unit cell volume Ω within 0.4 % of the experimental value measured at 5 K[1]We use this relaxed unit cell for most of the following calculations, and refer to it as Ω_{DFT}.

To simulate thermal lattice expansion, we use fixed experimental lattice parameters obtained at 295 K[1], and relax the internal atomic coordinates using PBE-D3. The volume of this room temperature structure is about 6 % larger than that of the low-temperature structure. The main expansion occurs in the *ab* plane, and through a decreased tilt of the monoclinic cell (see Table C.1 in the Appendix for all unit cell parameters). Any calculations that use this experimental lattice are labeled with $\Omega_{295\mathrm{K}}$.

5.2.2 Electronic and phonon band structures

The electronic band structure of naphthalene is characteristic for a small molecule crystal: it possesses a large band gap combined with flat, well separated bands (Fig. 5.1). DFT yields an indirect gap of 3.01 eV between the valence band maximum (VBM) at A and the conduction band minimum (CBM) at Γ. The weak intermolecular interactions between the molecules leads to small bandwidths, up to about 0.4 eV. Furthermore, because naphthalene has two molecules per unit cell, the electronic bands double up in so-called Davydov pairs [252, 253]. In the vicinity of the band gap, these Davydov pairs are separated from each other by about 0.4 eV. This separation drastically reduces mixing of states from different Davydov pairs. The wave functions of solid naphthalene are therefore mostly invariant throughout the Brillouin zone, and closely resemble linear combinations of gas-phase-like molecular orbitals.

[1]The experimental crystal structures are available at the Cambridge Structural Database [181]. The identifiers for the structures measured at 5 K and 295 K are NAPHTA31 and NAPHTA36, respectively, and published in association with [187].

Dispersion and interband interaction increase for bands below −2 eV as the spacing between electronic levels decreases, and for bands above 4.5 eV as the wave functions become more diffuse.

For the phonon frequencies, we obtain excellent agreement with experiments across the Brillouin zone using PBE-D3 (see Appendix C.3), similar to our previous results with the vdW-DF-cx functional in Chapter 4. Since we analyzed the vibrational properties of naphthalene in depth in this earlier work, we will give only a brief overview of the main features here. In naphthalene, intermolecular modes (<20 meV) can be clearly distinguished from intramolecular modes (20–400 meV). Intermolecular modes are translational and librational modes of rigid molecules, while for intramolecular modes, the phonon displacement vectors resemble linear combinations of gas phase vibrations.

We emphasize that, despite the clear separation between inter- and intramolecular modes, we treat all phonon modes on the same footing. While hopping transport models often use the rigid molecule approximation [229, 254, 255], it has been shown that the mixed inter- and intramolecular low-frequency modes can have large EPC contributions, especially for larger molecules like rubrene [256].

Upon thermal lattice expansion the spacing between molecules becomes larger. The lowered interaction leads to softening of the intermolecular modes, decreasing the lowest frequencies by up to 40 %. In contrast, intramolecular frequencies, which depend on the covalent interatomic forces, are computed to change very little, as shown in the Appendix in Fig. C.3.

5.2.3 Temperature-dependent renormalization of the electronic energies

We obtain the temperature-dependent corrections to the band structures of naphthalene from the real part of the electron-phonon self-energy

$$\varepsilon_{n\mathbf{k}}(T) = \varepsilon^0_{n\mathbf{k}} + \mathrm{Re}\left[\Sigma^{\mathrm{ep}}_{n\mathbf{k}}(\varepsilon^0_{n\mathbf{k}}, T)\right], \tag{5.1}$$

where $\varepsilon^0_{n\mathbf{k}}$ is the bare DFT eigenvalue with band index n and wave vector $\mathbf{k}$, and $\varepsilon_{n\mathbf{k}}$ is the renormalized energy. The self-energy $\Sigma^{\mathrm{ep}}_{n\mathbf{k}}$ is calculated according to the procedure laid out in section 2.4, and the computational details are given in Appendix C.1.

The temperature dependence of the VBM, CBM, and indirect band gap is shown in Fig. 5.2. The zero-point renormalization (ZPR) of the DFT band gap is calculated to be −0.23 eV, and is equally caused by the decrease of the CBM (−0.12 eV) and increase of the VBM energies (0.11 eV). This large correction reduces the DFT-PBE gap from 3.01 eV to 2.78 eV.

Increasing the temperature to 300 K, the band gap at unit cell volume Ω_{DFT} is predicted to be reduced by an additional −0.12 eV. The rate of change of the gap at this temperature is 0.05 eV/100 K, and increases only slightly to the linear limit of 0.064 eV/100 K at temperatures beyond 500 K.

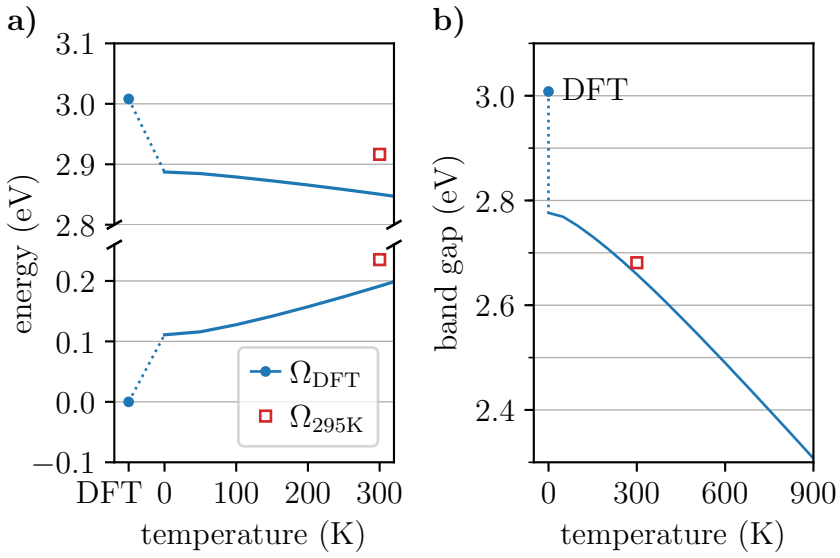

Figure 5.2: a) Renormalization and temperature dependence of the band edge states at Γ and A, with Ω_{DFT}. The dotted lines indicate the ZPR, connecting the bare eigenvalues calculated with PBD-D3 (circles) with the renormalized energies at 0 K. The renormalized energies for $\Omega_{295\mathrm{K}}$ (squares) at 300 K are plotted for comparison. b) ZPR (dotted) and temperature dependence (solid) of the indirect band gap of naphthalene for Ω_{DFT}. The red square shows the renormalization at 300 K using $\Omega_{295\mathrm{K}}$.

The DFT gap for the experimental room temperature structure at the enlarged volume $\Omega_{295\mathrm{K}}$ is widened, as expected, to 3.12 eV, an increase of 0.11 eV compared to Ω_{DFT}. The renormalization calculated at 300 K brings it down to 2.71 eV. Hence, we conclude that the two contributions to the renormalization we compute—the lattice expansion and the electron-phonon interaction—are not independent, additive terms. The EPC shows considerable volume dependence, with the renormalization increasing by 17 % from −0.35 eV at Ω_{DFT} to −0.41 eV at $\Omega_{295\mathrm{K}}$. This can be explained by a narrowing of the electronic bands upon lattice expansion and hence an increase in the electronic DOS. The increased DOS creates more scattering channels on the scale of the phonon energies, and thus an overall larger self-energy. Altogether, the volume expansion of $\Omega_{295\mathrm{K}}$ leads to two contributions to the renormalization of opposite sign, resulting in a band gap at 300 K that is only 70 meV smaller than the value at 0 K.

A complete description of the fundamental band gap is achieved by first correcting the DFT band gap with many-body perturbation theory to properly describe the electron-electron interaction, then adding the EPC corrections to account for the electron-phonon interaction. In Chapter 3 we show that the *GW* method, which accounts for the electron-electron interaction, increases the indirect DFT band gap of naphthalene by about 2.3 eV, thus bringing the DFT+*GW* band gap of the expanded room temperature structure to 5.4 eV. Adding the electron-phonon coupling renormalization computed at 300 K, we obtain

a fundamental gap of 5.0 eV, in excellent agreement with the experimental room temperature value of 5 eV [257].

5.2.4 Electrical mobilities

We compute the electrical mobilities of the electrons (μ^e) and the holes (μ^h) in the self-energy relaxation time approximation [258] with the expression

$$\mu_\alpha^{\mathrm{e,h}}(T) = \frac{-e}{\rho_{\mathrm{e,h}}\Omega}\sum_n \int \frac{d\mathbf{k}}{\Omega_{\mathrm{BZ}}} \frac{\partial f_{n\mathbf{k}}(T)}{\partial \varepsilon_{n\mathbf{k}}} |v_{n\mathbf{k},\alpha}|^2 \tau_{n\mathbf{k}}(T) \tag{5.2}$$

where α is the Cartesian direction of the applied electric field and the current, $\rho_{\mathrm{e,h}}$ is the carrier density of the electrons or the holes, Ω and Ω_{BZ} are the volumes of the unit cell and the Brillouin zone, $v_{n\mathbf{k},\alpha}$ is the velocity of the electronic state $n\mathbf{k}$ along direction α, and the sum over bands is restricted to conduction bands for μ^{e} and valence bands for μ^{h}. The lifetimes $\tau_{n\mathbf{k}}$ are obtained from the imaginary part of the electron-phonon self-energy

$$\tau_{n\mathbf{k}}^{-1}(T) = \frac{2}{\hbar}\,\mathrm{Im}\left[\Sigma_{n\mathbf{k}}^{\mathrm{ep}}(\varepsilon_{n\mathbf{k}}^0, T)\right]. \tag{5.3}$$

To evaluate Eq. (5.2) we use the Wannier90 package [259] to interpolate our computed electronic eigenvalues and velocities to a $60\times60\times60$ $\mathbf{k}$-grid. Calculating the EPC on this fine mesh is prohibitively expensive. We find, however, that the frequency-dependent self-energy for the bands around the gap is nearly independent of $\mathbf{k}$ (see Appendix C.6 for a detailed analysis). We therefore obtain the lifetimes $\tau_{n\mathbf{k}}$ on the dense $\mathbf{k}$-grid by interpolating the self-energy $\Sigma_{n\mathbf{k}'}^{\mathrm{ep}}$ of a single point $\mathbf{k}'$ using the approximation

$$\tau_{n\mathbf{k}}^{-1}(T) \approx \frac{2}{\hbar}\,\mathrm{Im}[\Sigma_{n\mathbf{k}'}^{\mathrm{ep}}(\varepsilon_{n\mathbf{k}}^0, T)]. \tag{5.4}$$

To minimize the error of this approximation, we choose $\mathbf{k}'$ to be at A for the hole, and Γ for the electron mobility, the locations of the VBM and CBM, respectively.

The calculated temperature-dependent hole and electron mobilities are shown in Fig. 5.3. Overall, the agreement with experiment is excellent at room temperature, and moderate to good at low temperature. This indicates that electronic band transport limited by phonon scattering accounts for much of the electrical mobility. It is also apparent that the lattice expansion plays an important role in obtaining accurate values, as the agreement greatly improves in most cases when using the room temperature unit cell with $\Omega_{295\mathrm{K}}$. To more accurately predict the power law (or the slope) of the experimental mobilities, the calculations need to be repeated using experimental lattice parameters obtained at different temperatures. This has been shown to lead to good agreement of the power law exponents [109]. Another reason for the disagreement with experiment is the contribution of polaronic effects and the physics of a hopping transport mechanism, which is missing from our first-principles approach. In particular, at temperatures above 100 K, the experimental electron mobilities

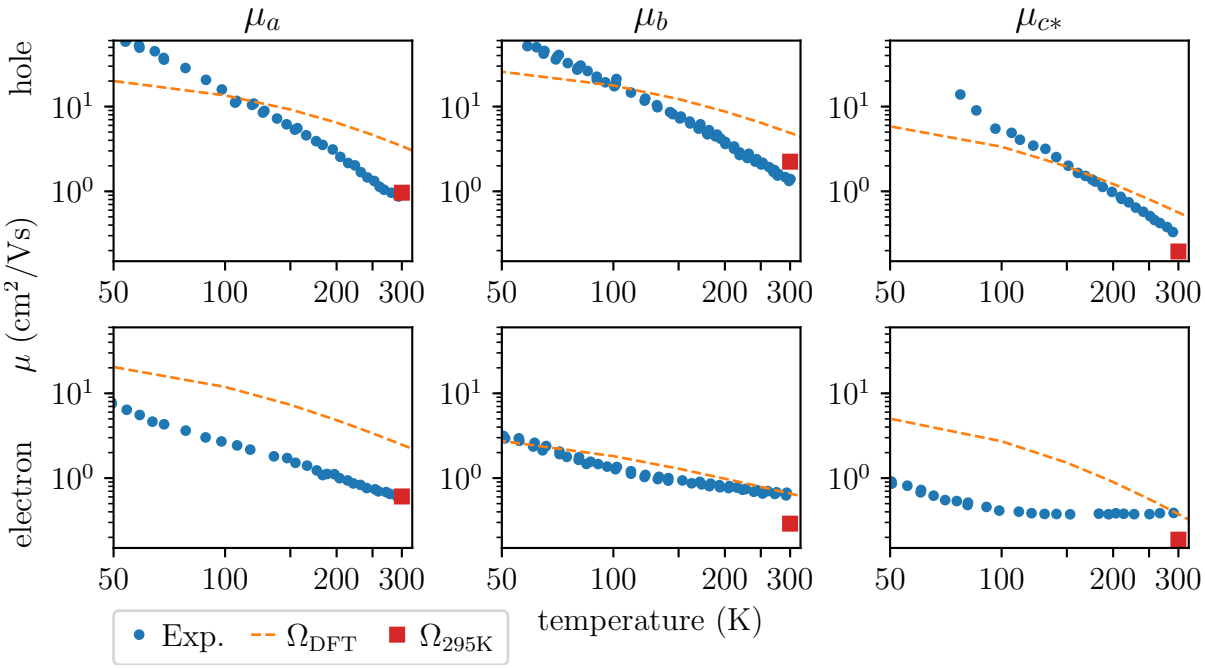

Figure 5.3: Calculated temperature-dependent hole (top) and electron (bottom) mobilities in comparison with experiment (blue dots) [260]. The calculated mobilities at 300 K using experimental room temperature ($\Omega_{295\mathrm{K}}$) lattice parameters (red squares) agree very well with the experimental values. For reference we also show the temperature dependence of the mobilities for the relaxed structure (Ω_{DFT}, orange dashed).

in the b and c^* direction show a decreased temperature dependence, commonly attributed to the transition to hopping transport [96, 261–263].

To gain insight into the mobilities, we decompose them into energy-resolved contributions by approximating Eq. (5.2) in the following way

$$\mu_\alpha^{\mathrm{e,h}} \approx \frac{-e}{\rho_{\mathrm{e,h}}} \int \mathrm{d}\varepsilon \, D(\varepsilon) f'(\varepsilon) v_\alpha^2(\varepsilon) \tau(\varepsilon), \tag{5.5}$$

where $D(\varepsilon)$ is the density of states (DOS), $f'(\varepsilon)$ is the derivative of the Fermi-Dirac distribution with respect to energy, and we define the average squared velocity function

$$v_\alpha^2(\varepsilon) = \frac{1}{D(\varepsilon)} \sum_n \int \frac{d\mathbf{k}}{\Omega_{\mathrm{BZ}}} (v_{n\mathbf{k},\alpha})^2 \delta(\varepsilon - \varepsilon_{n\mathbf{k}}) \tag{5.6}$$

and the average lifetime function

$$\tau(\varepsilon) = \frac{1}{D(\varepsilon)} \sum_n \int \frac{d\mathbf{k}}{\Omega_{\mathrm{BZ}}} \tau_{n\mathbf{k}} \delta(\varepsilon - \varepsilon_{n\mathbf{k}}). \tag{5.7}$$

The bounds of the integral in Eq. (5.5) go from $-\infty$ to the Fermi energy ε_F for holes, and from ε_F to $+\infty$ for electrons, and we add a small Gaussian smearing of 5 meV to evaluate the Dirac delta functions in Eqs. (5.6) and (5.7).

Equation (5.5) approximates the energy-resolved contributions to the mobilities as the product of four functions of energy. We plot these functions for $\Omega_{295\mathrm{K}}$ in Fig. 5.4. At 300 K, the contributions to the mobilities extend up to about 0.1 eV above or below the band edges. Within this region, the DOS, velocity, and lifetime are generally not monotonic functions of energy, but show distinct features. This highlights the need for a more detailed theory for predictive calculations as we use here; in contrast, for example, to approximations of the mobility that only use the effective mass of the band extrema, or constant effective lifetimes. This is especially true for μ_b^e, where the main contribution to the mobility is situated near the peak of the DOS, almost 0.1 eV within the conduction band. Using this analysis, we can also explain why the electron mobilities are generally lower than the hole mobilities. Comparing the individual functions, we see that the velocities of electrons along the a and c^* directions are actually larger than for holes. However, the stronger electron-phonon coupling of the conduction band reduces the electron lifetimes by a factor of almost two compared to the hole lifetimes, more than negating the higher velocities. In general, this analysis shows the critical role the individual contributions play in quantitatively determining the mobility.

While the expression in Eq. (5.5) is of great practicality for computing the mobilities and visualizing the energy-resolved lifetimes and velocities, it also turns out to be an excellent approximation. The maximum relative error compared to Eq. (5.2) is below 10 %, and the mean absolute relative error below 5 %. Mobilities calculated with this approximation deviate less than 3.3 % (see Appendix C.7). In addition to being independent of $\mathbf{k}$, the frequency-dependent self-energy of the highest (lowest) two valence (conduction) is almost identical. This is because the wave functions, and hence the electron-phonon matrix elements, of Davydov pairs are so similar (see Appendix C.6). Within this $\mathbf{k}$- and n-independent approximation, the electron and hole lifetimes are only a function of energy, and the expressions in Eq. (5.2) and Eq. (5.5) become equivalent.

5.2.5 Self-consistent electron-phonon self-energy

Figure 5.5 shows the frequency-dependent self-energies of the valence and conduction band alongside the electronic DOS. We see a clear correlation. This is mainly due to the fact that the electron-phonon coupling matrix elements are relatively independent of $\mathbf{k}$ and n within a Davydov pair. The imaginary part of Eq. (2.25) then becomes proportional to the joint electronic and vibrational density of states, weighted by the coupling strength of each phonon. In agreement with previous studies [107, 109], we find that intramolecular modes around 0.19 eV have the strongest coupling (see Fig. C.6 in the Appendix). Correspondingly, the peaks of the imaginary part of the SE are shifted by about 0.19 eV compared to the peaks of the DOS.

We also note from Fig. 5.5 that the real part of the self-energy varies rapidly between 0 and 0.15 eV over the frequency range corresponding to the bandwidth, which is on the order

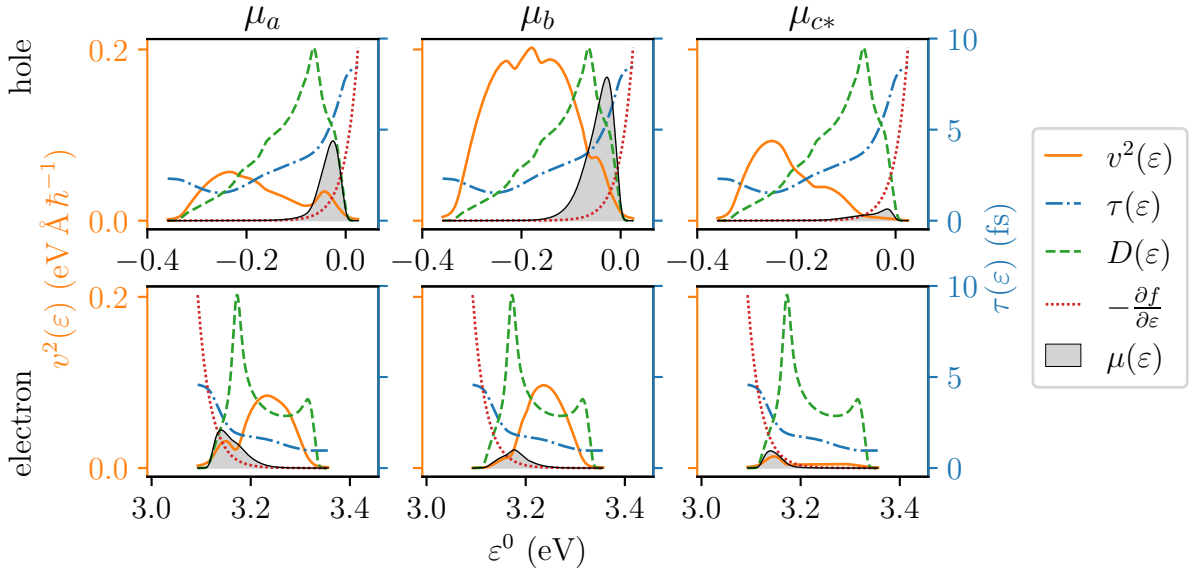

Figure 5.4: The energy-resolved decomposition of the mobility according to Eq. (5.5) of holes (top) and electrons (bottom) at 300 K and the experimental room temperature structure with Ω_{295K}. The velocity (orange solid) and the lifetime (blue dash-dot) are affiliated with the left and right y-axes respectively. The density of states $D(\varepsilon)$ (green dashed), the derivative of the Fermi-Dirac distribution (red dotted), and the mobility integrand (gray filled) are in arbitrary units, but share the same scale across all plots.

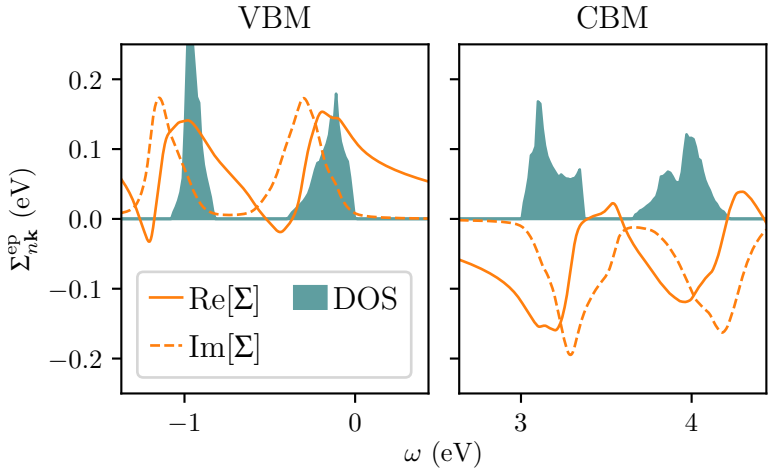

Figure 5.5: The real (solid) and imaginary part (dashed) of the electron-phonon self-energy of naphthalene, evaluated for the VBM at A (left) and CBM at Γ (right). The features of the self-energy correlate with the electronic DOS (filled).

of 0.4 eV. The renormalization of the bands will therefore significantly alter the shape and width of the DOS, upon which the self-energy depends. The magnitude of the self-energy corrections suggests that we should compute the self-energy self-consistently, by updating the electronic energies in Eq. (2.25) with the renormalized values.

Accordingly, we examine using an eigenvalue–self-consistent (evSC) cycle for the self-energy, whose iterative steps can be summarized as

$$\begin{aligned}
\varepsilon^1_{n\mathbf{k}} &= \varepsilon^0_{n\mathbf{k}} + \mathrm{Re}\left[\Sigma_{n\mathbf{k}}(\varepsilon^0_{n\mathbf{k}}, \varepsilon^0_{m\mathbf{k+q}})\right] \\
\varepsilon^2_{n\mathbf{k}} &= \varepsilon^0_{n\mathbf{k}} + \mathrm{Re}\left[\Sigma_{n\mathbf{k}}(\varepsilon^1_{n\mathbf{k}}, \varepsilon^1_{m\mathbf{k+q}})\right] \\
&\dots \\
\varepsilon^i_{n\mathbf{k}} &= \varepsilon^0_{n\mathbf{k}} + \mathrm{Re}\left[\Sigma_{n\mathbf{k}}(\varepsilon^{i-1}_{n\mathbf{k}}, \varepsilon^{i-1}_{m\mathbf{k+q}})\right],
\end{aligned} \tag{5.8}$$

where $\Sigma_{n\mathbf{k}}(\varepsilon^{i-1}_{n\mathbf{k}}, \varepsilon^{i-1}_{m\mathbf{k+q}})$ indicates the use of renormalized eigenvalues in the self-energy. We use the **k**-independence approximation to efficiently calculate the renormalized states $m\mathbf{k}$+**q** as

$$\varepsilon^i_{m\mathbf{k+q}} \approx \varepsilon^0_{m\mathbf{k+q}} + \mathrm{Re}\left[\Sigma_{n\mathbf{k}}(\varepsilon^{i-1}_{m\mathbf{k+q}})\right]. \tag{5.9}$$

This procedure converges the renormalized energies rapidly to within 2 meV for the bands around the gap (see Fig. C.9 in the Appendix).

Our method effectively includes all high-order non-crossing electron-phonon coupling diagrams in the self-energy. It does not, however, allow for multi-phonon satellite bands to form in the spectral function, as, for example, the cumulant expansion would [264]. A similar level of theory as evSC was previously achieved using a time propagation of the Green's function [265].

While the self-consistent calculation of the electron-phonon coupling self-energy offers a clear description of the quasiparticle temperature renormalization and lifetimes, one generally aims to compute these quantities from a one-shot calculation of the self-energy. Two different procedures are often used. In the on-the-mass-shell approximation [266], which we have used so far, the renormalized energies are computed according to Eq. (5.1) A different approach is to evaluate the self-energy at the quasiparticle energy, which corresponds to the peak of the spectral function, that is,

$$\varepsilon_{n\mathbf{k}}(T) = \varepsilon^0_{n\mathbf{k}} + \mathrm{Re}[\Sigma^{\mathrm{ep}}_{n\mathbf{k}}(\varepsilon_{n\mathbf{k}}, T)]. \tag{5.10}$$

In Table 5.1, we compare the two one-shot procedures against the self-consistent scheme. For the VBM and the CBM, the on-the-mass-shell approximation appears to better reproduce the self-consistent scheme, both for the real and imaginary part of the self-energy. The quasiparticle solution vastly overestimates the lifetimes of the band extrema (see Fig. C.11 in the Appendix).

Next, we examine the effect of the evSC approach through the spectral function, given by the imaginary part of the Green's function:

$$A_{n\mathbf{k}}(\omega) = \frac{1}{\pi} \frac{\left|\,\mathrm{Im}\left[\Sigma^{\mathrm{ep}}_{n\mathbf{k}}(\omega)\right]\,\right|}{\left[\omega - \varepsilon^0_{n\mathbf{k}} - \mathrm{Re}\left[\Sigma^{\mathrm{ep}}_{n\mathbf{k}}(\omega)\right]\right]^2 + \mathrm{Im}\left[\Sigma^{\mathrm{ep}}_{n\mathbf{k}}(\omega)\right]^2}. \tag{5.11}$$

Table 5.1: Comparison of the one-shot self-energy computed in the on-the-mass-shell approximation ($\Sigma(\varepsilon^0)$), the one-shot self-energy evaluated at the quasiparticle solution ($\Sigma(\varepsilon)$), and the eigenvalue–self-consistent self-energy (evSC).

	$\Sigma(\varepsilon^0)$	$\Sigma(\varepsilon)$	evSC
$\Delta\varepsilon_{\mathrm{VBM}}$ (0 K)	0.11	0.09	0.12
$\Delta\varepsilon_{\mathrm{CBM}}$ (0 K)	−0.12	−0.09	−0.12
τ_{VBM} (300 K)	8.70	38.47	7.91
τ_{CBM} (300 K)	4.73	21.16	6.42

It describes the probability of finding an electron in state $n\mathbf{k}$ at energy ω. The quasiparticle (QP) peaks of the spectral function appear at $\omega = \varepsilon^0 - \mathrm{Re}[\boldsymbol{\Sigma}^{\mathrm{ep}}(\omega)]$, which corresponds to the solution of Eq. (5.10). The spectral function allows us to compare both the renormalization (position of the QP peak) and the broadening (width and height of the QP peak) simultaneously.

Figure 5.6 shows both the one-shot and evSC spectral function, where we use the **k**-independence approximation to interpolate $A_{n\mathbf{k}}(\omega)$ across the Brillouin zone. We chose the self-energy at Γ as starting point for the interpolation, and checked that the choice of starting point does not alter the results significantly.

The QP bands of the evSC spectral function show a discontinuity at energies around 0.2 eV below the VBM and above the CBM, due to the spectral weight being transferred from the main quasiparticle peak to the satellite band. In contrast, the bands of the one-shot calculation are continuous, and the distinction between the main quasiparticle peak and the satellite remains clear in most cases. This band discontinuity (or splitting) happens when the real part of the self-energy has a slope $\gtrsim 1$. Then, the Dyson equation (5.10) may admit more than one solution in certain regions of the Brillouin zone. Such high slope in the self-energy is seen near the poles, located one phonon frequency away from the peaks of the DOS, as seen in Fig. 5.5 (the strongest coupling modes are ∼0.19 eV). A similar splitting has also been observed theoretically and experimentally in pentacene and rubrene crystals [250, 251, 267] as well as non-organic systems [268].

Finally, we evaluate the mobilities from the evSC self-energy at 300 K using $\Omega_{295\mathrm{K}}$ lattice parameters, taking into account the renormalized electronic eigenvalues and velocities. The results are listed in Table 5.2 in comparison with the values for the one-shot calculation and experiment. The evSC approach lowers the hole mobilities, bringing μ_a and μ_b to even better agreement with experiment. In contrast, evSC electron mobilities increase slightly compared to the one-shot calculation. By looking at the decomposition of the mobility via Eq. (5.5), we can attribute the decrease of the hole mobility to lower lifetimes, and the increase of the electron mobilities to higher lifetimes and velocities (see Fig. C.12 in the Appendix for the decomposition).

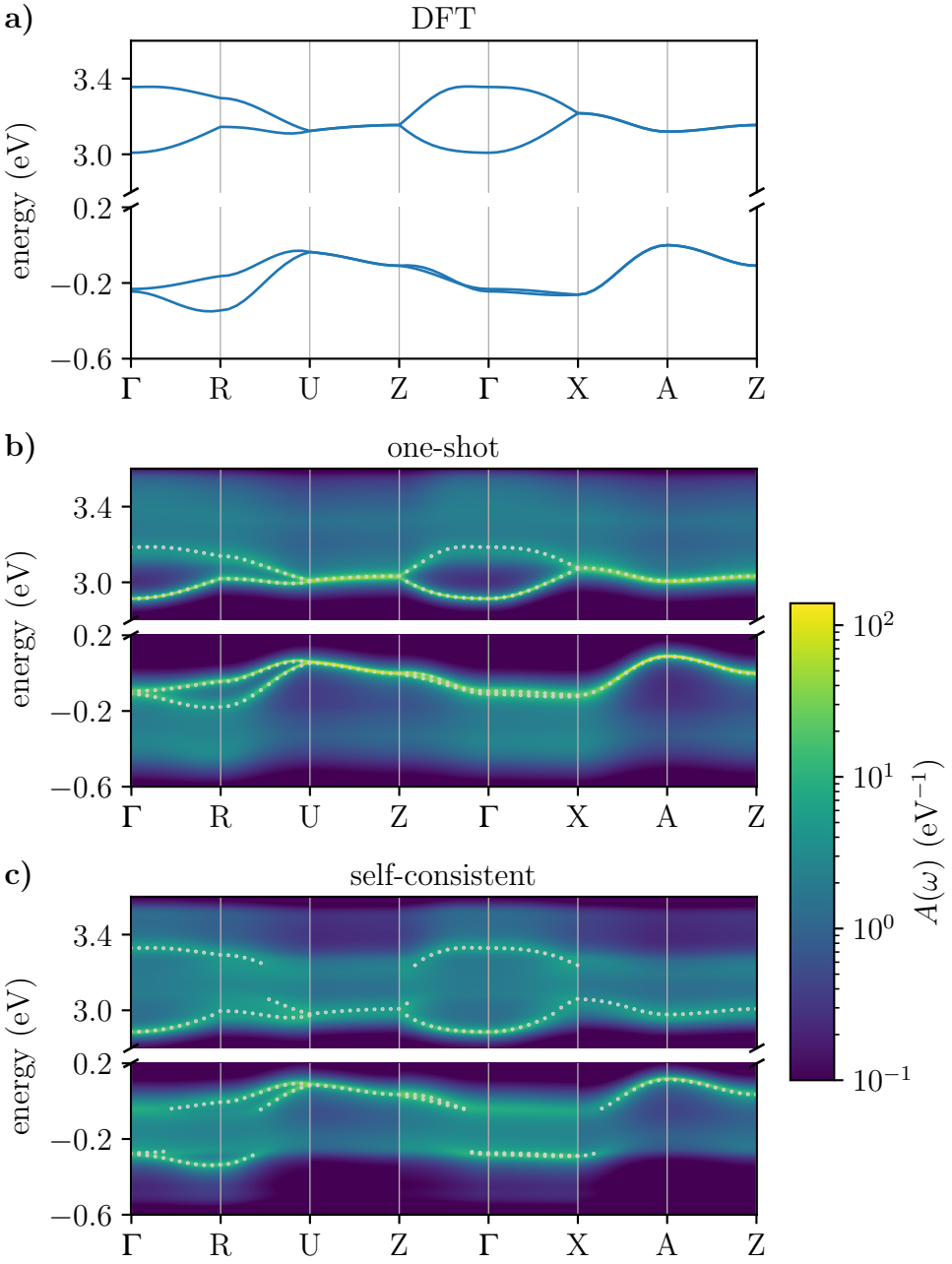

Figure 5.6: (a) The DFT-PBE-D3 band structure of naphthalene of the two highest valence, and two lowest conduction bands. (b) and (c) The spectral function of the full band structure calculated using the (b) one-shot and (c) self-consistent method. To highlight the renormalized band structure, the highest peak for each state $n\mathbf{k}$, i.e., the solution to Eq. (5.10) with the smallest imaginary part, is marked with a dot. While the one-shot spectral function displays a continues quasiparticle band-structure, the self-consistent result shows discontinuities.

Table 5.2: Mobilities calculated at 300 K with experimental lattice parameters ($\Omega_{295\mathrm{K}}$), using the one-shot and self-consistent (evSC) method, in comparison with experimental values. All values in $\mathrm{cm}^2/\mathrm{Vs}$.

	hole			electron		
	μ_a	μ_b	μ_{c^*}	μ_a	μ_b	μ_{c^*}
one-shot	1.20	2.73	0.24	0.67	0.31	0.21
evSC	0.90	2.19	0.18	1.18	0.59	0.31
Exp.	0.79	1.34	0.31	0.58	0.63	0.39

5.3 Conclusion

In summary, we used comprehensive *ab initio* calculations based on DFT to study the effect of electron-phonon interactions on the electronic structure of naphthalene crystals, as well as its electrical mobility. Both the temperature-dependent renormalization of the gap, and the hole and electron mobilities are in good agreement with experimental values, if the lattice expansion is taken into account. Because of the low dependence of the self-energy on $\mathbf{k}$ and n, we can visualize the contributions to the mobility at each band energy in terms of the density of states, average scattering time, and average velocity squared. This greatly facilitates the energy-resolved analysis of the mobility, and provides an efficient way to model charge carrier transport in organic systems.

Furthermore, we indirectly and approximately investigated the effect of higher-order electron-phonon coupling terms by calculating the self-energy self-consistently. The band gap renormalization and mobilities show only moderate differences between the one-shot and self-consistent calculations, as long as the on-the-mass-shell approximation is used. Both these properties depend mainly on the electronic states close to the band gap, which are only weakly affected by the evSC treatment. However, the electronic states further away from the band edges are strongly affected by the self-consistent treatment of the self-energy. The spectral function reveals a band splitting and band widening comparable to what has been observed experimentally in other molecular crystals.

Most of the qualitative results discussed in this work result directly from the weak interactions between molecules, a common feature of molecular crystals. This includes the $\mathbf{k}$-independence of the self-energy, and the band widths being on the same order of magnitude as the phonon frequencies. The methods and conclusions presented here likely apply to several other molecular crystals, and provide an efficient approach for the *ab initio* calculation of the electron-phonon self-energy and electrical mobility.

Chapter 6

Outlook

In this dissertation we use *ab initio* methods based on density functional theory to provide detailed insight into the complexity of the electronic and vibrational properties of organic crystals. We highlight the care that has to be taken to obtain accurate and predictive results, using van der Waals corrections for structural accuracy, different flavors of many-body perturbation theory for excited state energetics, and going beyond second-order perturbation theory for the electron-phonon self-energy. This work presents a comprehensive analysis of the renormalization and charge carrier mobility in acenes, within the adiabatic harmonic approximation.

There are several directions and new questions that emerge from our studies. How large are anharmonic contributions? Already 36 years ago, Jindal and Kalus [226] estimated anharmonic shifts of intermolecular phonons of up to 10 %, which is on the order of the deviation we see in our calculations. However, we generally underestimate the frequencies of the intermolecular modes, and anharmonic contributions would further lower the phonon frequencies. In contrast, the significant overestimation of high-energy C-H vibrations might be due to missing anharmonic contributions. As evident by our eigenvalue–self-consistent results, higher-order terms in the electron-phonon self-energy can have a strong impact in organic crystals. It has been shown that even if the phonons follow the harmonic description, the eigenvalues can deviate significantly [108], for example, leading to a 60 % reduction of the ZPR in lithium fluoride [157], which has a very flat valence band comparable to organic crystals. Different approaches have been developed and successfully applied to inorganic systems [139, 157, 269–271] to capture these higher-order effects.

While we study both the fundamental and optical gap in Chapter 3, we calculate the electron-phonon coupling using Kohn-Sham wave functions. Beyond anharmonicity, electron-electron effects need to be included to accurately describe experimental conditions. For one, use of the *GW* self-energy increases the band velocities of naphthalene by about 10 %, and hence leads to higher mobilities [109]. Even larger could be the influence on the electron-phonon coupling itself. Electron correlation via *GW* corrections substantially increases the EPC in graphene, graphite, and diamond [249, 272]. Based on our results in Chapter 5 this could further increase the electronic band width, but would also decrease the lifetimes.

While we thus expect a stronger renormalization and temperature dependence of the band gap, it remains to be seen, if these effects are on the same order of magnitude, and essentially cancel their contribution to the mobility.

Experimentally one of the most accessible observables is the optical absorption. Surprisingly, the optical gap in tetracene and pentacene increases with temperature [207, 273], the opposite of what we predict for the fundamental gap of naphthalene. This suggests that the volume expansion increases the exciton energies more than it increases the exciton-phonon coupling. Additionally, there is strong evidence that singlet fission in organic crystals can be affected or even driven by phonon scattering [274–277]. Frameworks to calculate exciton-phonon coupling from first principles have recently been developed [278–280], and we expect to see first results for organic crystals soon [281], shedding light on these important questions.

In this work we discussed in detail the mobility of naphthalene within the band transport framework, and how our results translate to other organic crystals. However, it seems clear that charge transport in molecular systems is situated somewhere between band and hopping transport, with the details being system-dependent and the exact mechanism still under active debate [103]. One challenge is to go beyond the Born-Oppenheimer approximation and include nonadiabatic dynamics. The biggest challenge, however, is to find an unbiased and predictive theory that seamlessly applies to the huge variety in molecular structures and crystal arrangements. This is instrumental for developing new efficient organic semiconductors, and improve existing devices. Most of the methods currently applied are computationally rather expensive, so broad benchmark across a variety of molecular systems would demand a vast amount of resources.

Lastly, very few calculations we are aware of are truly *ab initio*, as practically all use structural information from experiment. Indeed, predicting the crystal structure of organic crystals—or rather any complex material—is an ongoing challenge. However, this branch of research is rapidly gaining traction as the algorithms and energy predictions continue to improve, and more and more investigations are reported for these systems [282]. As we have seen in Chapters 3 and 4 the structure has a large effect on the electronic and vibrational property. Thus, being able to accurately predict new structures that can guide experimental efforts would be of utmost importance. Maybe one day we will be able to design molecular semiconductors from scratch that reach the efficiency of natural light harvesting proteins, the initial inspiration for this work. I hope this dissertation brought us one step closer.

Bibliography

[1] A. Hagfeldt, G. Boschloo, L. Sun, L. Kloo, and H. Pettersson, "Dye-sensitized solar cells," Chem. Rev. **110**, 6595 (2010).

[2] M. B. Smith and J. Michl, "Singlet fission," Chem. Rev. **110**, 6891 (2010).

[3] M. B. Smith and J. Michl, "Recent advances in singlet fission," Annu. Rev. Phys. Chem. **64**, 361 (2013).

[4] D. Lee, L. Greenman, M. Sarovar, and K. B. Whaley, "*Ab initio* calculation of molecular aggregation effects: A coumarin-343 case study," J. Phys. Chem. A **117**, 11072 (2013).

[5] J. E. Anthony, "Functionalized acenes and heteroacenes for organic electronics," Chem. Rev. **106**, 5028 (2006).

[6] X.-Y. Zhu, Q. Yang, and M. Muntwiler, "Charge-transfer excitons at organic semiconductor surfaces and interfaces," Acc. Chem. Res. **42**, 1779 (2009).

[7] D. N. Congreve, J. Lee, N. J. Thompson, E. Hontz, S. R. Yost, P. D. Reusswig, M. E. Bahlke, S. Reineke, T. Van Voorhis, and M. A. Baldo, "External quantum efficiency above 100% in a singlet-exciton-fission-based organic photovoltaic cell," Science **340**, 334 (2013).

[8] W.-L. Chan, T. C. Berkelbach, M. R. Provorse, N. R. Monahan, J. R. Tritsch, M. S. Hybertsen, D. R. Reichman, J. Gao, and X.-Y. Zhu, "The quantum coherent mechanism for singlet fission: Experiment and theory," Acc. Chem. Res. **46**, 1321 (2013).

[9] S. Li, L. Ye, W. Zhao, S. Zhang, S. Mukherjee, H. Ade, and J. Hou, "Energy-level modulation of small-molecule electron acceptors to achieve over 12% efficiency in polymer solar cells," Adv. Mater. **28**, 9423 (2016).

[10] W. Zhao, S. Li, H. Yao, S. Zhang, Y. Zhang, B. Yang, and J. Hou, "Molecular optimization enables over 13% efficiency in organic solar cells," J. Am. Chem. Soc. **139**, 7148 (2017).

[11] M. Mandai, K. Takada, T. Aoki, T. Fujinami, Y. Nakanishi, and Y. Hatanaka, "AFM observation for the change of surface morphology of TPD thin films due to thermal annealing," Synth. Met. **91**, 123 (1997).

[12] S. Caria, E. D. Como, M. Murgia, R. Zamboni, P. Melpignano, and V. Biondo, "Enhanced light emission efficiency and current stability by morphology control and thermal annealing of organic light emitting diode devices," J. Phys. Condens. Matter **18**, S2139 (2006).

[13] V. Subramanian, P. C. Chang, J. B. Lee, S. E. Molesa, and S. K. Volkman, "Printed organic transistors for ultra-low-cost RFID applications," IEEE Trans. Compon. Packag. Technol. **28**, 742 (2005).

[14] Y. Aleeva and B. Pignataro, "Recent advances in upscalable wet methods and ink formulations for printed electronics," J. Mater. Chem. C **2**, 6436 (2014).

[15] G. P. Rigas and M. Shkunov, "Solution processable semiconducting organic single crystals," Polym. Sci. Ser. C **56**, 20 (2014).

[16] Y. Xu, C. Liu, D. Khim, and Y.-Y. Noh, "Development of high-performance printed organic field-effect transistors and integrated circuits," Phys. Chem. Chem. Phys. **17**, 26553 (2015).

[17] A. P. Kulkarni, C. J. Tonzola, A. Babel, and S. A. Jenekhe, "Electron transport materials for organic light-emitting diodes," Chem. Mater. **16**, 4556 (2004).

[18] H. Minemawari, T. Yamada, H. Matsui, J. Tsutsumi, S. Haas, R. Chiba, R. Kumai, and T. Hasegawa, "Inkjet printing of single-crystal films," Nature **475**, 364 (2011).

[19] N. R. Armstrong, W. Wang, D. M. Alloway, D. Placencia, E. Ratcliff, and M. Brumbach, "Organic/organic' heterojunctions: organic light emitting diodes and organic photovoltaic devices," Macromol. Rapid Commun. **30**, 717 (2009).

[20] R. Meerheim, B. Lussem, and K. Leo, "Efficiency and stability of p-i-n type organic light emitting diodes for display and lighting applications," Proc. IEEE **97**, 1606 (2009).

[21] X. Yang, G. Zhou, and W.-Y. Wong, "Recent design tactics for high performance white polymer light-emitting diodes," J. Mater. Chem. C **2**, 1760 (2014).

[22] C. D. Dimitrakopoulos and P. R. L. Malenfant, "Organic thin film transistors for large area electronics," Adv. Mater. **14**, 99 (2002).

[23] C. R. Newman, C. D. Frisbie, D. A. da Silva Filho, J.-L. Brédas, P. C. Ewbank, and K. R. Mann, "Introduction to organic thin film transistors and design of n-channel organic semiconductors," Chem. Mater. **16**, 4436 (2004).

[24] A. Facchetti, "Semiconductors for organic transistors," Mater. Today **10**, 28 (2007).

[25] H. Sirringhaus, "25th Anniversary Article: Organic field-effect transistors: The path beyond amorphous silicon," Adv. Mater. **26**, 1319 (2014).

[26] X. Gao and Z. Zhao, "High mobility organic semiconductors for field-effect transistors," Sci. China Chem. **58**, 947 (2015).

[27] L. Dou, J. You, Z. Hong, Z. Xu, G. Li, R. A. Street, and Y. Yang, "25th Anniversary Article: A decade of organic/polymeric photovoltaic research," Adv. Mater. **25**, 6642 (2013).

[28] J.-L. Brédas, J. E. Norton, J. Cornil, and V. Coropceanu, "Molecular understanding of organic solar cells: The challenges," Acc. Chem. Res. **42**, 1691 (2009).

[29] B. Kippelen and J.-L. Brédas, "Organic photovoltaics," Energy Environ. Sci. **2**, 251 (2009).

[30] S. M. Sze and K. K. Ng, *Physics of semiconductor devices* (John Wiley & Sons, Nov. 3, 2006).

[31] J.-L. Lin, W.-J. Sah, and S.-C. Lee, "Amorphous-silicon thin-film transistors with very high field-effect mobility," IEEE Electron Device Lett. **12**, 120 (1991).

[32] K. A. Stewart, B.-S. Yeh, and J. F. Wager, "Amorphous semiconductor mobility limits," J. Non-Cryst. Solids **432**, 196 (2016).

[33] H. Dong, X. Fu, J. Liu, Z. Wang, and W. Hu, "25th Anniversary Article: Key points for high-mobility organic field-effect transistors," Adv. Mater. **25**, 6158 (2013).

[34] E. Menard, V. Podzorov, S.-H. Hur, A. Gaur, M. E. Gershenson, and J. A. Rogers, "High-performance n- and p-type single-crystal organic transistors with free-space gate dielectrics," Adv. Mater. **16**, 2097 (2004).

[35] J. Takeya, M. Yamagishi, Y. Tominari, R. Hirahara, Y. Nakazawa, T. Nishikawa, T. Kawase, T. Shimoda, and S. Ogawa, "Very high-mobility organic single-crystal transistors with in-crystal conduction channels," Appl. Phys. Lett. **90**, 102120 (2007).

[36] J. E. Anthony, "The larger acenes: versatile organic semiconductors," Angew. Chem. Int. Ed. **47**, 452 (2008).

[37] G. Schweicher, Y. Olivier, V. Lemaur, and Y. H. Geerts, "What currently limits charge carrier mobility in crystals of molecular semiconductors?," Isr. J. Chem. **54**, 595 (2014).

[38] S. Fratini, S. Ciuchi, D. Mayou, G. T. de Laissardière, and A. Troisi, "A map of high-mobility molecular semiconductors," Nat. Mater. **16**, 998 (2017).

[39] O. D. Jurchescu, J. Baas, and T. T. M. Palstra, "Effect of impurities on the mobility of single crystal pentacene," Appl. Phys. Lett. **84**, 3061 (2004).

[40] O. D. Jurchescu, M. Popinciuc, B. J. van Wees, and T. T. M. Palstra, "Interface-controlled, high-mobility organic transistors," Adv. Mater. **19**, 688 (2007).

[41] H. Klauk, M. Halik, U. Zschieschang, G. Schmid, W. Radlik, R. Brederlow, S. Briole, C. Pacha, R. Thewes, and W. Weber, "Polymer gate dielectric pentacene TFTs and circuits on flexible substrates," in Digest. International Electron Devices Meeting (2002), pp. 557–560.

[42] B. Stadlober, M. Zirkl, M. Beutl, G. Leising, S. Bauer-Gogonea, and S. Bauer, "High-mobility pentacene organic field-effect transistors with a high-dielectric-constant fluorinated polymer film gate dielectric," Appl. Phys. Lett. **86**, 242902 (2005).

[43] Y. C. Cheng, R. J. Silbey, D. A. da Silva Filho, J. P. Calbert, J. Cornil, and J. L. Brédas, "Three-dimensional band structure and bandlike mobility in oligoacene single crystals: A theoretical investigation," J. Chem. Phys. **118**, 3764 (2003).

[44] A. F. Paterson, S. Singh, K. J. Fallon, T. Hodsden, Y. Han, B. C. Schroeder, H. Bronstein, M. Heeney, I. McCulloch, and T. D. Anthopoulos, "Recent progress in high-mobility organic transistors: A reality check," Adv. Mater. **30**, 1801079 (2018).

[45] F. C. Krebs, J. Alstrup, H. Spanggaard, K. Larsen, and E. Kold, "Production of large-area polymer solar cells by industrial silk screen printing, lifetime considerations and lamination with polyethyleneterephthalate," Sol. Energy Mater. Sol. Cells **83**, 293 (2004).

[46] F. C. Krebs and K. Norrman, "Analysis of the failure mechanism for a stable organic photovoltaic during 10 000 h of testing," Prog. Photovolt. Res. Appl. **15**, 697 (2007).

[47] N. Grossiord, J. M. Kroon, R. Andriessen, and P. W. M. Blom, "Degradation mechanisms in organic photovoltaic devices," Org. Electron. **13**, 432 (2012).

[48] P. Cheng and X. Zhan, "Stability of organic solar cells: challenges and strategies," Chem. Soc. Rev. **45**, 2544 (2016).

[49] M. C. Hanna and A. J. Nozik, "Solar conversion efficiency of photovoltaic and photoelectrolysis cells with carrier multiplication absorbers," J. Appl. Phys. **100**, 074510 (2006).

[50] N. J. Thompson, M. W. B. Wilson, D. N. Congreve, P. R. Brown, J. M. Scherer, T. S. Bischof, M. Wu, N. Geva, M. Welborn, T. V. Voorhis, V. Bulović, M. G. Bawendi, and M. A. Baldo, "Energy harvesting of non-emissive triplet excitons in tetracene by emissive PbS nanocrystals," Nat. Mater. **13**, 1039 (2014).

[51] M. Tabachnyk, B. Ehrler, S. Gélinas, M. L. Böhm, B. J. Walker, K. P. Musselman, N. C. Greenham, R. H. Friend, and A. Rao, "Resonant energy transfer of triplet excitons from pentacene to PbSe nanocrystals," Nat. Mater. **13**, 1033 (2014).

[52] C. J. Bardeen, "Triplet excitons: Bringing dark states to light," Nat. Mater. **13**, 1001 (2014).

[53] A. Rao and R. H. Friend, "Harnessing singlet exciton fission to break the Shockley–Queisser limit," Nat. Rev. Mater. **2**, 17063 (2017).

[54] F. Cicoira, C. Santato, F. Dinelli, M. Murgia, M. A. Loi, F. Biscarini, R. Zamboni, P. Heremans, and M. Muccini, "Morphology and field-effect-transistor mobility in tetracene thin films," Adv. Funct. Mater. **15**, 375 (2005).

[55] E. Busby, T. C. Berkelbach, B. Kumar, A. Chernikov, Y. Zhong, H. Hlaing, X.-Y. Zhu, T. F. Heinz, M. S. Hybertsen, M. Y. Sfeir, D. R. Reichman, C. Nuckolls, and O. Yaffe, "Multiphonon relaxation slows singlet fission in crystalline hexacene," J. Am. Chem. Soc. **136**, 10654 (2014).

[56] T. Bučko, J. Hafner, S. Lebègue, and J. G. Ángyán, "Improved description of the structure of molecular and layered crystals: *Ab initio* DFT calculations with van der Waals corrections," J. Phys. Chem. A **114**, 11814 (2010).

[57] J. Klimeš and A. Michaelides, "Perspective: Advances and challenges in treating van der Waals dispersion forces in density functional theory," J. Chem. Phys. **137**, 120901 (2012).

[58] M. S. Hybertsen and S. G. Louie, "Electron correlation in semiconductors and insulators: Band gaps and quasiparticle energies," Phys. Rev. B **34**, 5390 (1986).

[59] L. Hedin, "New method for calculating the one-particle Green's function with application to the electron-gas problem," Phys. Rev. **139**, A796 (1965).

[60] G. Onida, L. Reining, R. W. Godby, R. Del Sole, and W. Andreoni, "*Ab initio* calculations of the quasiparticle and absorption spectra of clusters: The sodium tetramer," Phys. Rev. Lett. **75**, 818 (1995).

[61] G. Onida, L. Reining, and A. Rubio, "Electronic excitations: density-functional versus many-body Green's-function approaches," Rev. Mod. Phys. **74**, 601 (2002).

[62] M. Rohlfing and S. G. Louie, "Electron-hole excitations and optical spectra from first principles," Phys. Rev. B **62**, 4927 (2000).

[63] M. L. Tiago and J. R. Chelikowsky, "First-principles GW–BSE excitations in organic molecules," Solid State Commun. **136**, 333 (2005).

[64] M. Shishkin and G. Kresse, "Self-consistent GW calculations for semiconductors and insulators," Phys. Rev. B **75**, 235102 (2007).

[65] D. Jacquemin, I. Duchemin, and X. Blase, "0–0 Energies using hybrid schemes: Benchmarks of TD-DFT, CIS(D), ADC(2), CC2, and BSE/GW formalisms for 80 real-life compounds," J. Chem. Theory Comput. **11**, 5340 (2015).

[66] D. Jacquemin, I. Duchemin, and X. Blase, "Benchmarking the Bethe–Salpeter formalism on a standard organic molecular set," J. Chem. Theory Comput. **11**, 3290 (2015).

[67] M. J. van Setten, F. Caruso, S. Sharifzadeh, X. Ren, M. Scheffler, F. Liu, J. Lischner, L. Lin, J. R. Deslippe, S. G. Louie, C. Yang, F. Weigend, J. B. Neaton, F. Evers, and P. Rinke, "GW100: Benchmarking G_0W_0 for molecular systems," J. Chem. Theory Comput. **11**, 5665 (2015).

[68] X. Leng, F. Jin, M. Wei, and Y. Ma, "GW method and Bethe–Salpeter equation for calculating electronic excitations," Wiley Interdiscip. Rev. Comput. Mol. Sci. **6**, and references therein, 532 (2016).

[69] Z. Ergönenc, B. Kim, P. Liu, G. Kresse, and C. Franchini, "Converged GW quasiparticle energies for transition metal oxide perovskites," Phys. Rev. Materials **2**, 024601 (2018).

[70] X. Blase, I. Duchemin, and D. Jacquemin, "The Bethe–Salpeter equation in chemistry: relations with TD-DFT, applications and challenges," Chem. Soc. Rev. **47**, 1022 (2018).

[71] P. M. Zimmerman, F. Bell, D. Casanova, and M. Head-Gordon, "Mechanism for singlet fission in pentacene and tetracene: From single exciton to two triplets," J. Am. Chem. Soc. **133**, 19944 (2011).

[72] D. Beljonne, H. Yamagata, J. L. Brédas, F. C. Spano, and Y. Olivier, "Charge-transfer excitations steer the Davydov splitting and mediate singlet exciton fission in pentacene," Phys. Rev. Lett. **110**, 226402 (2013).

[73] T. C. Berkelbach, M. S. Hybertsen, and D. R. Reichman, "Microscopic theory of singlet exciton fission. I. General formulation," J. Chem. Phys. **138**, 114102 (2013).

[74] N. Renaud, P. A. Sherratt, and M. A. Ratner, "Mapping the relation between stacking geometries and singlet fission yield in a class of organic crystals," J. Phys. Chem. Lett. **4**, 1065 (2013).

[75] P. M. Zimmerman, C. B. Musgrave, and M. Head-Gordon, "A correlated electron view of singlet fission," Acc. Chem. Res. **46**, 1339 (2013).

[76] P. B. Coto, S. Sharifzadeh, J. B. Neaton, and M. Thoss, "Low-lying electronic excited states of pentacene oligomers: A comparative electronic structure study in the context of singlet fission," J. Chem. Theory Comput. **11**, 147 (2015).

[77] M. L. Tiago, J. E. Northrup, and S. G. Louie, "*Ab initio* calculation of the electronic and optical properties of solid pentacene," Phys. Rev. B **67** (2003) 10.1103/PhysRevB.67.115212.

[78] K. Hummer, P. Puschnig, and C. Ambrosch-Draxl, "*Ab initio* study of anthracene under high pressure," Phys. Rev. B **67**, 184105 (2003).

[79] K. Hummer, P. Puschnig, and C. Ambrosch-Draxl, "Lowest optical excitations in molecular crystals: Bound excitons versus free electron-hole pairs in anthracene," Phys. Rev. Lett. **92**, 147402 (2004).

[80] K. Hummer and C. Ambrosch-Draxl, "Electronic properties of oligoacenes from first principles," Phys. Rev. B **72**, 205205 (2005).

[81] J. B. Neaton, M. S. Hybertsen, and S. G. Louie, "Renormalization of molecular electronic levels at metal-molecule interfaces," Phys. Rev. Lett. **97**, 216405 (2006).

[82] C. Ambrosch-Draxl, D. Nabok, P. Puschnig, and C. Meisenbichler, "The role of polymorphism in organic thin films: Oligoacenes investigated from first principles," New J. Phys. **11**, 125010 (2009).

[83] S. Sharifzadeh, A. Biller, L. Kronik, and J. B. Neaton, "Quasiparticle and optical spectroscopy of the organic semiconductors pentacene and PTCDA from first principles," Phys. Rev. B **85**, 125307 (2012).

[84] P. Cudazzo, M. Gatti, and A. Rubio, "Excitons in molecular crystals from first-principles many-body perturbation theory: Picene versus pentacene," Phys. Rev. B **86**, 195307 (2012).

[85] P. Cudazzo, M. Gatti, A. Rubio, and F. Sottile, "Frenkel versus charge-transfer exciton dispersion in molecular crystals," Phys. Rev. B **88**, 195152 (2013).

[86] S. Refaely-Abramson, S. Sharifzadeh, M. Jain, R. Baer, J. B. Neaton, and L. Kronik, "Gap renormalization of molecular crystals from density-functional theory," Phys. Rev. B **88**, 081204 (2013).

[87] S. Refaely-Abramson, M. Jain, S. Sharifzadeh, J. B. Neaton, and L. Kronik, "Solid-state optical absorption from optimally tuned time-dependent range-separated hybrid density functional theory," Phys. Rev. B **92**, 081204 (2015).

[88] P. Cudazzo, F. Sottile, A. Rubio, and M. Gatti, "Exciton dispersion in molecular solids," J. Phys. Condens. Matter **27**, 113204 (2015).

[89] B. Schatschneider, J.-J. Liang, A. M. Reilly, N. Marom, G.-X. Zhang, and A. Tkatchenko, "Electrodynamic response and stability of molecular crystals," Phys. Rev. B **87**, 060104(R) (2013).

[90] A. M. Reilly and A. Tkatchenko, "Understanding the role of vibrations, exact exchange, and many-body van der Waals interactions in the cohesive properties of molecular crystals," J. Chem. Phys. **139**, 024705 (2013).

[91] I. Fedorov, F. Marsusi, T. Fedorova, and Y. Zhuravlev, "First principles study of the electronic structure and phonon dispersion of naphthalene under pressure," J. Phys. Chem. Solids **83**, 24 (2015).

[92] M. Abdulla, K. Refson, R. H. Friend, and P. D. Haynes, "A first-principles study of the vibrational properties of crystalline tetracene under pressure," J. Phys. Condens. Matter **27**, 375402 (2015).

[93] K. Hannewald and P. A. Bobbert, "*Ab initio* theory of charge-carrier conduction in ultrapure organic crystals," Appl. Phys. Lett. **85**, 1535 (2004).

[94] A. Troisi, D. L. Cheung, and D. Andrienko, "Charge transport in semiconductors with multiscale conformational dynamics," Phys. Rev. Lett. **102**, 116602 (2009).

[95] A. Girlando, L. Grisanti, M. Masino, I. Bilotti, A. Brillante, R. G. Della Valle, and E. Venuti, "Peierls and Holstein carrier-phonon coupling in crystalline rubrene," Phys. Rev. B **82**, 035208 (2010).

[96] F. Ortmann, F. Bechstedt, and K. Hannewald, "Charge transport in organic crystals: Interplay of band transport, hopping and electron–phonon scattering," New J. Phys. **12**, 023011 (2010).

[97] J. E. Northrup, "Two-dimensional deformation potential model of mobility in small molecule organic semiconductors," Appl. Phys. Lett. **99**, 062111 (2011).

[98] J. Xi, M. Long, L. Tang, D. Wang, and Z. Shuai, "First-principles prediction of charge mobility in carbon and organic nanomaterials," Nanoscale **4**, 4348 (2012).

[99] H. Kobayashi, N. Kobayashi, S. Hosoi, N. Koshitani, D. Murakami, R. Shirasawa, Y. Kudo, D. Hobara, Y. Tokita, and M. Itabashi, "Hopping and band mobilities of pentacene, rubrene, and 2,7-dioctyl[1]benzothieno[3,2-b][1]benzothiophene (C8-BTBT) from first principle calculations," J. Chem. Phys. **139**, 014707 (2013).

[100] A. Heck, J. J. Kranz, T. Kubař, and M. Elstner, "Multi-scale approach to non-adiabatic charge transport in high-mobility organic semiconductors," J. Chem. Theory Comput. **11**, 5068 (2015).

[101] O. Ostroverkhova, "Organic optoelectronic materials: Mechanisms and applications," Chem. Rev. **116**, 13279 (2016).

[102] H. Ishii, N. Kobayashi, and K. Hirose, "Charge transport calculations by a wave-packet dynamical approach using maximally localized Wannier functions based on density functional theory: Application to high-mobility organic semiconductors," Phys. Rev. B **95**, 035433 (2017).

[103] H. Oberhofer, K. Reuter, and J. Blumberger, "Charge transport in molecular materials: An assessment of computational methods," Chem. Rev. **117**, 10319 (2017).

[104] V. Stehr, R. F. Fink, C. Deibel, and B. Engels, "Charge carrier mobilities in organic semiconductor crystals based on the spectral overlap," J. Comput. Chem. **37**, 2146 (2016).

[105] H. Ishii, J.-i. Inoue, N. Kobayashi, and K. Hirose, "Quantitative mobility evaluation of organic semiconductors using quantum dynamics based on density functional theory," Phys. Rev. B **98**, 235422 (2018).

[106] M. Casula, M. Calandra, and F. Mauri, "Local and nonlocal electron-phonon couplings in K_3 picene and the effect of metallic screening," Phys. Rev. B **86**, 075445 (2012).

[107] N. Vukmirović, C. Bruder, and V. M. Stojanović, "Electron-phonon coupling in crystalline organic semiconductors: Microscopic evidence for nonpolaronic charge carriers," Phys. Rev. Lett. **109**, 126407 (2012).

[108] B. Monserrat, E. A. Engel, and R. J. Needs, "Giant electron-phonon interactions in molecular crystals and the importance of nonquadratic coupling," Phys. Rev. B **92**, 140302(R) (2015).

[109] N.-E. Lee, J.-J. Zhou, L. A. Agapito, and M. Bernardi, "Charge transport in organic molecular semiconductors from first principles: The bandlike hole mobility in a naphthalene crystal," Phys. Rev. B **97**, 115203 (2018).

[110] C. Fiolhais, F. Nogueira, and M. A. L. Marques, eds., *A primer in density functional theory*, Lecture Notes in Physics (Springer-Verlag, Berlin Heidelberg, 2003).

[111] P. Hohenberg and W. Kohn, "Inhomogeneous electron gas," Phys. Rev. **136**, B864 (1964).

[112] W. Kohn and L. J. Sham, "Self-consistent equations including exchange and correlation effects," Phys. Rev. **140**, A1133 (1965).

[113] J. P. Perdew and W. Yue, "Accurate and simple density functional for the electronic exchange energy: Generalized gradient approximation," Phys. Rev. B **33**, 8800 (1986).

[114] J. P. Perdew, K. Burke, and M. Ernzerhof, "Generalized gradient approximation made simple," Phys. Rev. Lett. **77**, 3865 (1996).

[115] K. E. Riley, M. Pitoňák, P. Jurečka, and P. Hobza, "Stabilization and structure calculations for noncovalent interactions in extended molecular systems based on wave function and density functional theories," Chem. Rev. **110**, 5023 (2010).

[116] J.-L. Calais and E. S. Kryachko, eds., *Conceptual perspectives in quantum chemistry* (Springer Netherlands, 1997).

[117] S. Grimme, "Accurate description of van der Waals complexes by density functional theory including empirical corrections," J. Comput. Chem. **25**, 1463 (2004).

[118] E. R. Johnson and A. D. Becke, "A post-Hartree–Fock model of intermolecular interactions," J. Chem. Phys. **123**, 024101 (2005).

[119] S. Grimme, "Semiempirical GGA-type density functional constructed with a long-range dispersion correction," J. Comput. Chem. **27**, 1787 (2006).

[120] A. Tkatchenko and M. Scheffler, "Accurate molecular van der Waals interactions from ground-state electron density and free-atom reference data," Phys. Rev. Lett. **102**, 073005 (2009).

[121] S. Grimme, J. Antony, S. Ehrlich, and H. Krieg, "A consistent and accurate *ab initio* parametrization of density functional dispersion correction (DFT-D) for the 94 elements H-Pu," J. Chem. Phys. **132**, 154104 (2010).

[122] A. Otero-de-la-Roza and E. R. Johnson, "Non-covalent interactions and thermochemistry using XDM-corrected hybrid and range-separated hybrid density functionals," J. Chem. Phys. **138**, 204109 (2013).

[123] C. Corminboeuf, "Minimizing density functional failures for non-covalent interactions beyond van der Waals complexes," Acc. Chem. Res. **47**, 3217 (2014).

[124] S. Grimme, S. Ehrlich, and L. Goerigk, "Effect of the damping function in dispersion corrected density functional theory," J. Comput. Chem. **32**, 1456 (2011).

[125] D. C. Langreth, B. I. Lundqvist, S. D. Chakarova-Käck, V. R. Cooper, M. Dion, P. Hyldgaard, A. Kelkkanen, J. Kleis, L. Kong, S. Li, P. G. Moses, E. Murray, A. Puzder, H. Rydberg, E. Schröder, and T. Thonhauser, "A density functional for sparse matter," J. Phys. Condens. Matter **21**, 084203 (2009).

[126] P. Hyldgaard, K. Berland, and E. Schröder, "Interpretation of van der Waals density functionals," Phys. Rev. B **90**, 075148 (2014).

[127] K. Berland, V. R. Cooper, K. Lee, E. Schröder, T. Thonhauser, P. Hyldgaard, and B. I. Lundqvist, "Van der Waals forces in density functional theory: A review of the vdW-DF method," Rep. Prog. Phys. **78**, 066501 (2015).

[128] M. Dion, H. Rydberg, E. Schröder, D. C. Langreth, and B. I. Lundqvist, "Van der Waals density functional for general geometries," Phys. Rev. Lett. **92**, 246401 (2004).

[129] K. Lee, É. D. Murray, L. Kong, B. I. Lundqvist, and D. C. Langreth, "Higher-accuracy van der Waals density functional," Phys. Rev. B **82**, 081101(R) (2010).

[130] O. A. Vydrov and T. Van Voorhis, "Nonlocal van der Waals density functional: The simpler the better," J. Chem. Phys. **133**, 244103 (2010).

[131] K. Berland and P. Hyldgaard, "Exchange functional that tests the robustness of the plasmon description of the van der Waals density functional," Phys. Rev. B **89**, 035412 (2014).

[132] F. Bloch, "Über die Quantenmechanik der Elektronen in Kristallgittern," Z. Physik **52**, 555 (1929).

[133] C. Kittel, *Quantum theory of solids* (Wiley, 1987).

[134] N. W. Ashcroft and N. D. Mermin, *Solid state physics*, 1st ed. (Saunders College, 1976).

[135] M. L. Cohen and S. G. Louie, *Fundamentals of condensed matter physics*, 1st ed. (Cambridge University Press, 2016).

[136] H. Hellmann, *Einführung in die Quantenchemie* (F. Deuticke, Leipzig und Wien, 1937).

[137] R. P. Feynman, "Forces in molecules," Phys. Rev. **56**, 340 (1939).

[138] J. H. Lloyd-Williams and B. Monserrat, "Lattice dynamics and electron-phonon coupling calculations using nondiagonal supercells," Phys. Rev. B **92**, 184301 (2015).

[139] B. Monserrat, "Electron–phonon coupling from finite differences," J. Phys. Condens. Matter **30**, 083001 (2018).

[140] S. Baroni, S. de Gironcoli, A. Dal Corso, and P. Giannozzi, "Phonons and related crystal properties from density-functional perturbation theory," Rev. Mod. Phys. **73**, 515 (2001).

[141] P. Ghosez, E. Cockayne, U. V. Waghmare, and K. M. Rabe, "Lattice dynamics of $BaTiO_3$, $PbTiO_3$, and $PbZrO_3$: A comparative first-principles study," Phys. Rev. B **60**, 836 (1999).

[142] "Nuclear scattering by crystals," in G. L. Squires, *Introduction to the Theory of Thermal Neutron Scattering*, 3rd ed. (Cambridge University Press, 2012), pp. 25–60.

[143] A. Schindlmayr, T. J. Pollehn, and R. W. Godby, "Spectra and total energies from self-consistent many-body perturbation theory," Phys. Rev. B **58**, 12684 (1998).

[144] F. Bruneval, N. Vast, and L. Reining, "Effect of self-consistency on quasiparticles in solids," Phys. Rev. B **74**, 045102 (2006).

[145] M. van Schilfgaarde, T. Kotani, and S. Faleev, "Quasiparticle self-consistent GW theory," Phys. Rev. Lett. **96**, 226402 (2006).

[146] C. Rostgaard, K. W. Jacobsen, and K. S. Thygesen, "Fully self-consistent GW calculations for molecules," Phys. Rev. B **81**, 085103 (2010).

[147] N. Marom, F. Caruso, X. Ren, O. T. Hofmann, T. Körzdörfer, J. R. Chelikowsky, A. Rubio, M. Scheffler, and P. Rinke, "Benchmark of GW methods for azabenzenes," Phys. Rev. B **86**, 245127 (2012).

[148] S. Körbel, P. Boulanger, I. Duchemin, X. Blase, M. A. L. Marques, and S. Botti, "Benchmark many-body GW and Bethe–Salpeter calculations for small transition metal molecules," J. Chem. Theory Comput. **10**, 3934 (2014).

[149] F. Giustino, S. G. Louie, and M. L. Cohen, "Electron-phonon renormalization of the direct band gap of diamond," Phys. Rev. Lett. **105**, 265501 (2010).

[150] S. Poncé, Y. Gillet, J. Laflamme Janssen, A. Marini, M. Verstraete, and X. Gonze, "Temperature dependence of the electronic structure of semiconductors and insulators," J. Chem. Phys. **143**, 102813 (2015).

[151] S. Poncé, G. Antonius, Y. Gillet, P. Boulanger, J. Laflamme Janssen, A. Marini, M. Côté, and X. Gonze, "Temperature dependence of electronic eigenenergies in the adiabatic harmonic approximation," Phys. Rev. B **90**, 214304 (2014).

[152] F. Giustino, "Electron-phonon interactions from first principles," Rev. Mod. Phys. **89**, 015003 (2017).

[153] P. B. Allen and V. Heine, "Theory of the temperature dependence of electronic band structures," J. Phys. C: Solid State Phys. **9**, 2305 (1976).

[154] A. Eiguren and C. Ambrosch-Draxl, "Wannier interpolation scheme for phonon-induced potentials: Application to bulk MgB_2, W, and the 1×1 H-covered W(110) surface," Phys. Rev. B **78**, 045124 (2008).

[155] C. Verdi and F. Giustino, "Fröhlich electron-phonon vertex from first principles," Phys. Rev. Lett. **115**, 176401 (2015).

[156] X. Gonze, P. Boulanger, and M. Côté, "Theoretical approaches to the temperature and zero-point motion effects on the electronic band structure," Ann. Phys. **523**, 168 (2011).

[157] G. Antonius, S. Poncé, E. Lantagne-Hurtubise, G. Auclair, X. Gonze, and M. Côté, "Dynamical and anharmonic effects on the electron-phonon coupling and the zero-point renormalization of the electronic structure," Phys. Rev. B **92**, 085137 (2015).

[158] T. Rangel, K. Berland, S. Sharifzadeh, F. Brown-Altvater, K. Lee, P. Hyldgaard, L. Kronik, and J. B. Neaton, "Structural and excited-state properties of oligoacene crystals from first principles," Phys. Rev. B **93**, 115206 (2016).

[159] D. Faltermeier, B. Gompf, M. Dressel, A. Tripathi, and J. Pflaum, "Optical properties of pentacene thin films and single crystals," Phys. Rev. B **74** (2006).

[160] C. C. Mattheus, A. B. Dros, J. Baas, A. Meetsma, J. L. de Boer, and T. T. M. Palstra, "Polymorphism in pentacene," Acta Cryst. C **57**, 939 (2001).

[161] E. Venuti, R. G. Della Valle, L. Farina, A. Brillante, M. Masino, and A. Girlando, "Phonons and structures of tetracene polymorphs at low temperature and high pressure," Phys. Rev. B **70**, 104106 (2004).

[162] R. G. D. Valle, A. Brillante, L. Farina, E. Venuti, M. Masino, and A. Girlando, "Organic semiconductors: Polymorphism, phonon dynamics and carrier-phonon coupling in pentacene," Mol. Cryst. Liq. Cryst. **416**, 145 (2004).

[163] T. Kakudate, N. Yoshimoto, and Y. Saito, "Polymorphism in pentacene thin films on SiO_2 substrate," Appl. Phys. Lett. **90**, 081903 (2007).

[164] L. Farina, A. Brillante, R. G. Della Valle, E. Venuti, M. Amboage, and K. Syassen, "Pressure-induced phase transition in pentacene," Chem. Phys. Lett. **375**, 490 (2003).

[165] C. C. Mattheus, A. B. Dros, J. Baas, G. T. Oostergetel, A. Meetsma, J. L. de Boer, and T. T. M. Palstra, "Identification of polymorphs of pentacene," Synth. Met. **138**, 475 (2003).

[166] D. Nabok, P. Puschnig, and C. Ambrosch-Draxl, "Cohesive and surface energies of π-conjugated organic molecular crystals: A first-principles study," Phys. Rev. B **77**, 245316 (2008).

[167] K. Berland and P. Hyldgaard, "Structure and binding in crystals of cagelike molecules: Hexamine and platonic hydrocarbons," J. Chem. Phys. **132**, 134705 (2010).

[168] K. Berland, Ø. Borck, and P. Hyldgaard, "Van der Waals density functional calculations of binding in molecular crystals," Comput. Phys. Commun. **182**, 1800 (2011).

[169] A. Otero-de-la-Roza and E. R. Johnson, "A benchmark for non-covalent interactions in solids," J. Chem. Phys. **137**, 054103 (2012).

[170] W. A. Al-Saidi, V. K. Voora, and K. D. Jordan, "An assessment of the vdW-TS method for extended systems," J. Chem. Theory Comput. **8**, 1503 (2012).

[171] T. Bučko, S. Lebègue, J. Hafner, and J. G. Ángyán, "Tkatchenko-Scheffler van der Waals correction method with and without self-consistent screening applied to solids," Phys. Rev. B **87**, 064110 (2013).

[172] L. Kronik and A. Tkatchenko, "Understanding molecular crystals with dispersion-inclusive density functional theory: Pairwise corrections and beyond," Acc. Chem. Res. **47**, 3208 (2014).

[173] D. Lu, Y. Li, D. Rocca, and G. Galli, "*Ab initio* calculation of van der Waals bonded molecular crystals," Phys Rev Lett **102**, 206411 (2009).

[174] R. A. DiStasio, V. V. Gobre, and A. Tkatchenko, "Many-body van der Waals interactions in molecules and condensed matter," J. Phys. Condens. Matter **26**, 213202 (2014).

[175] A. M. Reilly and A. Tkatchenko, "Van der Waals dispersion interactions in molecular materials: beyond pairwise additivity," Chem. Sci. **6**, 3289 (2015).

[176] S. Yanagisawa, K. Okuma, T. Inaoka, and I. Hamada, "Recent progress in predicting structural and electronic properties of organic solids with the van der Waals density functional," J. Electron. Spectros. Relat. Phenomena, Organic Electronics **204**, 159 (2015).

[177] C. Sutton, C. Risko, and J.-L. Brédas, "Noncovalent intermolecular interactions in organic electronic materials: Implications for the molecular packing vs electronic properties of acenes," Chem. Mater. **28**, 3 (2016).

[178] K. Berland, C. A. Arter, V. R. Cooper, K. Lee, B. I. Lundqvist, E. Schröder, T. Thonhauser, and P. Hyldgaard, "Van der Waals density functionals built upon the electron-gas tradition: Facing the challenge of competing interactions," J. Chem. Phys. **140**, 18A539 (2014).

[179] R. B. Campbell, J. M. Robertson, and J. Trotter, "The crystal structure of hexacene, and a revision of the crystallographic data for tetracene," Acta. Cryst. **15**, 289 (1962).

[180] D. Holmes, S. Kumaraswamy, A. J. Matzger, and K. P. C. Vollhardt, "On the nature of nonplanarity in the [N]phenylenes," Chem. – Eur. J. **5**, 3399 (1999).

[181] I. R. Thomas, I. J. Bruno, J. C. Cole, C. F. Macrae, E. Pidcock, and P. a. Wood, "WebCSD: the online portal to the Cambridge Structural Database," J. Appl. Crystallogr. **43**, 362 (2010); *Cambridge Structural Database*, `http://webcsd.ccdc.cam.ac.uk/`.

[182] J. Kalinowski and R. Jankowiak, "Pressure dependence of the Davydov splitting in tetracene single crystals," Chem. Phys. Lett. **53**, 56 (1978).

[183] D. D. Kolendritskii, M. V. Kurik, and Y. P. Piryatinskii, "Exciton reflection spectra of tetracene single crystals," Phys. Status Solidi B **91**, 741 (1979).

[184] Z. Rang, A. Haraldsson, D. M. Kim, P. P. Ruden, M. I. Nathan, R. J. Chesterfield, and C. D. Frisbie, "Hydrostatic-pressure dependence of the photoconductivity of single-crystal pentacene and tetracene," Appl. Phys. Lett. **79**, 2731 (2001).

[185] U. Sondermann, A. Kutoglu, and H. Bassler, "X-ray diffraction study of the phase transition in crystalline tetracene," J. Phys. Chem. **89**, 1735 (1985).

[186] M. Oehzelt, A. Aichholzer, R. Resel, G. Heimel, E. Venuti, and R. G. Della Valle, "Crystal structure of oligoacenes under high pressure," Phys. Rev. B **74**, 104103 (2006).

[187] S. C. Capelli, A. Albinati, S. a. Mason, and B. T. M. Willis, "Molecular motion in crystalline naphthalene: Analysis of multi-temperature X-ray and neutron diffraction data," J. Phys. Chem. A **110**, 11695 (2006).

[188] W. I. F. David, R. M. Ibberson, G. A. Jeffrey, and J. R. Ruble, "The crystal structure analysis of deuterated benzene and deuterated nitromethane by pulsed-neutron powder diffraction: A comparison with single crystal neutron diffraction analysis," Physica B Condens. Matter **180-181**, 597 (1992).

[189] S. L. Chaplot, N. Lehner, and G. S. Pawley, "The structure of anthracene-d10 at 16 K using neutron diffraction," Acta Crystallogr. Sect. B **38**, 483 (1982).

[190] S. Schiefer, M. Huth, A. Dobrinevski, and B. Nickel, "Determination of the crystal structure of substrate-induced pentacene polymorphs in fiber structured thin films," J. Am. Chem. Soc. **129**, 10316 (2007).

[191] M. Watanabe, Y. J. Chang, S.-W. Liu, T.-H. Chao, K. Goto, M. M. Islam, C.-H. Yuan, Y.-T. Tao, T. Shinmyozu, and T. J. Chow, "The synthesis, crystal structure and charge-transport properties of hexacene," Nat. Chem. **4**, 574 (2012).

[192] J. S. Chickos and W. E. Acree, "Enthalpies of sublimation of organic and organometallic compounds. 1910–2001," J. Phys. Chem. Ref. Data **31**, 537 (2002).

[193] É. D. Murray, K. Lee, and D. C. Langreth, "Investigation of exchange energy density functional accuracy for interacting molecules," J. Chem. Theory Comput. **5**, 2754 (2009).

[194] K. Berland and P. Hyldgaard, "Analysis of van der Waals density functional components: Binding and corrugation of benzene and C_{60} on boron nitride and graphene," Phys. Rev. B **87**, 205421 (2013).

[195] Y. Zhang and J. Singh, "Use of Kubo formalism to study transport beyond the Born approximation: Application to low-temperature transport in Si metal–oxide–semiconductor field-effect transistors," Appl. Phys. Lett. **73**, 1577 (1998).

[196] I. Hamada, "Van der Waals density functional made accurate," Phys. Rev. B **89**, 121103 (2014).

[197] G. E. Bacon, N. A. Curry, and S. A. Wilson, "A crystallographic study of solid benzene by neutron diffraction," Proc. R. Soc. Lond. A **279**, 98 (1964).

[198] N. Sato, K. Seki, and H. Inokuchi, "Polarization energies of organic solids determined by ultraviolet photoelectron spectroscopy," J. Chem. Soc., Faraday Trans. 2 **77**, 1621 (1981).

[199] J. P. Doering, "Electronic energy levels of benzene below 7 eV," J. Chem. Phys. **67**, 4065 (1977).

[200] K. Hummer and C. Ambrosch-Draxl, "Oligoacene exciton binding energies: Their dependence on molecular size," Phys. Rev. B **71**, 081202 (2005).

[201] P. Swiderek, M. Michaud, G. Hohlneicher, and L. Sanche, "Electron energy loss spectroscopy of solid naphthalene and acenaphthene: Search for the low-lying triplet states," Chem. Phys. Lett. **175**, 667 (1990).

[202] O. Schnepp, "Electronic spectra of molecular crystals," Annu. Rev. Phys. Chem. **14**, 35 (1963).

[203] E. M. Grumstrup, J. C. Johnson, and N. H. Damrauer, "Enhanced triplet formation in polycrystalline tetracene films by femtosecond optical-pulse shaping," Phys. Rev. Lett. **105**, 257403 (2010).

[204] J. Burgos, M. Pope, C. E. Swenberg, and R. R. Alfano, "Heterofission in pentacene-doped tetracene single crystals," Phys. Status Solidi B **83**, 249 (1977).

[205] Hexacene S_1 is extracted from the position of first bright excitation in Refs. [55, 191, 283] and T_1 is extrapolated from shorter acenes in Ref. [4].

[206] J. Helzel, S. Jankowski, M. E. Helou, G. Witte, and W. Heimbrodt, "Temperature dependent optical properties of pentacene films on zinc oxide," Appl. Phys. Lett. **99**, 211102 (2011).

[207] M. W. B. Wilson, A. Rao, K. Johnson, S. Gélinas, R. di Pietro, J. Clark, and R. H. Friend, "Temperature-independent singlet exciton fission in tetracene," J. Am. Chem. Soc. **135**, 16680 (2013).

[208] S. Sharifzadeh, P. Darancet, L. Kronik, and J. B. Neaton, "Low-energy charge-transfer excitons in organic solids from first-principles: The case of pentacene," J. Phys. Chem. Lett. **4**, 2197 (2013).

[209] S. Sharifzadeh, C. Y. Wong, H. Wu, B. L. Cotts, L. Kronik, N. S. Ginsberg, and J. B. Neaton, "Relating the physical structure and optoelectronic function of crystalline TIPS-pentacene," Adv. Funct. Mater. **25**, 2038 (2015).

[210] F. Brown-Altvater, T. Rangel, and J. B. Neaton, "*Ab initio* phonon dispersion in crystalline naphthalene using van der Waals density functionals," Phys. Rev. B **93**, 195206 (2016).

[211] J. Lee, P. Jadhav, P. D. Reusswig, S. R. Yost, N. J. Thompson, D. N. Congreve, E. Hontz, T. Van Voorhis, and M. A. Baldo, "Singlet exciton fission photovoltaics," Acc. Chem. Res. **46**, 1300 (2013).

[212] F. Ortmann, F. Bechstedt, and K. Hannewald, "Charge transport in organic crystals: Theory and modelling," Phys. Status Solidi B **248**, 511 (2011).

[213] T. M. K. Nedungadi, "Analysis of the Raman spectrum of single crystals of naphthalene," Proc. Indian Acad. Sci. - Sect. A **15**, 376 (1942).

[214] G. C. Pimentel and A. L. McClellan, "The infrared spectra of naphthalene crystals, vapor, and solutions," J. Chem. Phys. **20**, 270 (1952).

[215] J. Hollas, "The fluorescence spectrum of naphthalene vapor in the 3100A region," J. Mol. Spectrosc. **9**, 138 (1962).

[216] M. Suzuki, T. Yokoyama, and M. Ito, "Polarized Raman spectra of naphthalene and anthracene single crystals," Spectrochim. Acta Part Mol. Spectrosc. **24**, 1091 (1968).

[217] D. M. Hanson, "Phosphorescence spectrum, vibronic analysis, and lattice frequencies of the naphthalene molecule in a deuteronaphthalene crystal," J. Chem. Phys. **51**, 5063 (1969).

[218] G. A. Mackenzie, G. S. Pawley, and O. W. Dietrich, "Phonon measurements and model calculations for naphthalene-d_8," J. Phys. C Solid State Phys. **10**, 3723 (1977).

[219] I. Natkaniec, E. L. Bokhenkov, B. Dorner, J. Kalus, G. A. Mackenzie, G. S. Pawley, U. Schmelzer, and E. F. Sheka, "Phonon dispersion in d_8-naphthalene crystal at 6K," J. Phys. C Solid State Phys. **13**, 4265 (1980).

[220] E. L. Bokhenkov, A. I. Kolesnikov, T. A. Krivenko, E. F. Shek, V. A. Dementjev, and I. Natkaniec, "Neutron spectroscopy of internal phonons of naphthalene and anthracene crystals," J. Phys. Colloq. **42**, {C6-605} (1981).

[221] J. Lielmezs, F. Bennett, and D. McFee, "Thermodynamic functions for naphthalene," Thermochim. Acta **47**, 287 (1981).

[222] E. F. Sheka, E. L. Bokhenkov, B. Dorner, J. Kalus, G. A. Mackenzie, I. Natkaniec, G. S. Pawley, and U. Schmelzer, "Anharmonicity of phonons in crystalline naphthalene," J. Phys. C Solid State Phys. **17**, 5893 (1984).

[223] A. Srivastava and V. B. Singh, "Theoretical and experimental studies of vibrational spectra of naphthalene and its cation," Indian J. Pure Ap. Phy. **45**, 7 (2007).

[224] K. P. Meletov, "Phonon spectrum of a naphthalene crystal at a high pressure: Influence of shortened distances on the lattice and intramolecular vibrations," Phys. Solid State **55**, 581 (2013).

[225] E. Huler and A. Warshel, "On the consistent calculation of lattice dynamics using semiempirical potential functions," Chem. Phys. **8**, 239 (1975).

[226] V. K. Jindal and J. Kalus, "A calculation of the anharmonic phonon frequencies in solid deuterated naphthalene-d_8," J. Phys. C Solid State Phys. **16**, 3061 (1983).

[227] R. G. Della Valle, E. Venuti, and A. Brillante, "Pressure and temperature effects in lattice dynamics: The case of naphthalene," Chem. Phys. **198**, 79 (1995).

[228] G. M. Day, S. L. Price, and M. Leslie, "Atomistic calculations of phonon frequencies and thermodynamic quantities for crystals of rigid organic molecules," J. Phys. Chem. B **107**, 10919 (2003).

[229] V. Coropceanu, R. S. Sánchez-Carrera, P. Paramonov, G. M. Day, and J.-L. Brédas, "Interaction of charge carriers with lattice vibrations in organic molecular semiconductors: Naphthalene as a case study," J. Phys. Chem. C **113**, 4679 (2009).

[230] G. S. Pawley, "A model for the lattice dynamics of naphthalene and anthracene," Phys. Status Solidi B **20**, 347 (1967).

[231] G. S. Pawley and S. J. Cyvin, "Lattice vibrations in crystals with deformable molecules; a calculation for naphthalene," J. Chem. Phys. **52**, 4073 (1970).

[232] R. Righini, S. Califano, and S. Walmsley, "Calculated phonon dispersion curves for fully deuterated naphthalene crystals at low temperature," Chem. Phys. **50**, 113 (1980).

[233] V. Schettino and S. Califano, "Lattice dynamics and interaction potentials in molecular crystals," J. Mol. Struct. **100**, 459 (1983).

[234] N. Rougeau, J. Flament, P. Youkharibache, H. Gervais, and G. Berthier, "Vibrational modelling in large polycyclic aromatic hydrocarbons," J. Mol. Struct. THEOCHEM **254**, 405 (1992).

[235] F. Pauzat, D. Talbi, M. D. Miller, D. J. DeFrees, and Y. Ellinger, "Theoretical IR spectra of ionized naphthalene," J. Phys. Chem. **96**, 7882 (1992).

[236] E. Cebe and G. Grampp, "Detailed quantummechanical calculations of molecular vibration frequencies of benzene, naphthalene, anthracene and phenanthrene. Comparison of several quantumchemical methods," Z. Phys. Chem. **187**, 15 (1994).

[237] S. R. Langhoff, "Theoretical infrared spectra for polycyclic aromatic hydrocarbon neutrals, cations, and anions," J. Phys. Chem. **100**, 2819 (1996).

[238] C. W. Bauschlicher and S. R. Langhoff, "The calculation of accurate harmonic frequencies of large molecules: the polycyclic aromatic hydrocarbons, a case study," Spectrochim. Acta. A. Mol. Biomol. Spectrosc. **53**, 1225 (1997).

[239] E. F. C. Byrd, G. E. Scuseria, and C. F. Chabalowski, "An *ab initio* study of solid nitromethane, HMX, RDX, and CL20: Successes and failures of DFT," J. Phys. Chem. B **108**, 13100 (2004).

[240] D. W. J. Cruickshank, "A detailed refinement of the crystal and molecular structure of naphthalene," Acta Crystallogr. **10**, 504 (1957).

[241] G. S. Pawley and E. A. Yeats, "A neutron diffraction study of perdeuteronaphthalene," Acta Crystallogr. B **25**, 2009 (1969).

[242] A. Warshel and S. Lifson, "Consistent force field calculations. II. Crystal structures, sublimation energies, molecular and lattice vibrations, molecular conformations, and enthalpies of alkanes," J. Chem. Phys. **53**, 582 (1970).

[243] B. P. van Eijck, "*Ab initio* crystal structure predictions for flexible hydrogen-bonded molecules. Part III. Effect of lattice vibrations," J. Comput. Chem. **22**, 816 (2001).

[244] P. Hao, Y. Fang, J. Sun, G. I. Csonka, P. H. T. Philipsen, and J. P. Perdew, "Lattice constants from semilocal density functionals with zero-point phonon correction," Phys. Rev. B **85**, 014111 (2012).

[245] C. Wang, H. Dong, L. Jiang, and W. Hu, "Organic semiconductor crystals," Chem. Soc. Rev. **47**, 422 (2018).

[246] A. Marini, "Ab initio finite-temperature excitons," Phys. Rev. Lett. **101**, 106405 (2008).

[247] H. Kawai, K. Yamashita, E. Cannuccia, and A. Marini, "Electron-electron and electron-phonon correlation effects on the finite-temperature electronic and optical properties of zinc-blende GaN," Phys. Rev. B **89**, 085202 (2014).

[248] J. P. Nery and P. B. Allen, "Influence of Fröhlich polaron coupling on renormalized electron bands in polar semiconductors: Results for zinc-blende GaN," Phys. Rev. B **94**, 115135 (2016).

[249] G. Antonius, S. Poncé, P. Boulanger, M. Côté, and X. Gonze, "Many-body effects on the zero-point renormalization of the band structure," Phys. Rev. Lett. **112**, 215501 (2014).

[250] S. Ciuchi, R. C. Hatch, H. Höchst, C. Faber, X. Blase, and S. Fratini, "Molecular fingerprints in the electronic properties of crystalline organic semiconductors: From experiment to theory," Phys. Rev. Lett. **108**, 256401 (2012).

[251] F. Bussolotti, J. Yang, T. Yamaguchi, K. Yonezawa, K. Sato, M. Matsunami, K. Tanaka, Y. Nakayama, H. Ishii, N. Ueno, and S. Kera, "Hole-phonon coupling effect on the band dispersion of organic molecular semiconductors," Nat. Commun. **8**, 173 (2017).

[252] A. S. Davydov, "The theory of molecular excitons," Sov. Phys. Uspekhi **7**, 145 (1964).

[253] E. F. Sheka, "Davydov splitting in the absorption spectra of molecular crystals," Mol. Cryst. Liq. Cryst. **29**, 323 (1975).

[254] A. Troisi and G. Orlandi, "Charge-transport regime of crystalline organic semiconductors: Diffusion limited by thermal off-diagonal electronic disorder," Phys. Rev. Lett. **96**, 086601 (2006).

[255] L. Wang and D. Beljonne, "Flexible surface hopping approach to model the crossover from hopping to band-like transport in organic crystals," J. Phys. Chem. Lett. **4**, 1888 (2013).

[256] X. Xie, A. Santana-Bonilla, and A. Troisi, "Nonlocal electron–phonon coupling in prototypical molecular semiconductors from first principles," J. Chem. Theory Comput. **14**, 3752 (2018).

[257] C. L. Braun and G. M. Dobbs, "Intrinsic photoconductivity in naphthalene single crystals," J. Chem. Phys. **53**, 2718 (1970).

[258] S. Poncé, E. R. Margine, and F. Giustino, "Towards predictive many-body calculations of phonon-limited carrier mobilities in semiconductors," Phys. Rev. B **97**, 121201 (2018).

[259] A. A. Mostofi, J. R. Yates, G. Pizzi, Y.-S. Lee, I. Souza, D. Vanderbilt, and N. Marzari, "An updated version of wannier90: A tool for obtaining maximally-localised Wannier functions," Comput. Phys. Commun. **185**, 2309 (2014).

[260] O. Madelung, U. Rössler, and M. Schulz, eds., *Ternary compounds, organic semiconductors*, Vol. 41E, Landolt-Börnstein - Group III Condensed Matter (Springer-Verlag, Berlin/Heidelberg, 2000).

[261] L. B. Schein, C. B. Duke, and A. R. McGhie, "Observation of the band-hopping transition for electrons in naphthalene," Phys. Rev. Lett. **40**, 197 (1978).

[262] L. B. Schein and A. R. McGhie, "Band-hopping mobility transition in naphthalene and deuterated naphthalene," Phys. Rev. B **20**, 1631 (1979).

[263] W. Warta and N. Karl, "Hot holes in naphthalene: High, electric-field-dependent mobilities," Phys. Rev. B **32**, 1172 (1985).

[264] J. P. Nery, P. B. Allen, G. Antonius, L. Reining, A. Miglio, and X. Gonze, "Quasiparticles and phonon satellites in spectral functions of semiconductors and insulators: Cumulants applied to the full first-principles theory and the Fröhlich polaron," Phys. Rev. B **97**, 115145 (2018).

[265] D. Dunn, "Electron-phonon interactions in an insulator," Can. J. Phys. **53**, 321 (1975).

[266] E. Cannuccia and A. Marini, "Zero point motion effect on the electronic properties of diamond, trans-polyacetylene and polyethylene," Eur. Phys. J. B **85**, 320 (2012).

[267] S. Ciuchi and S. Fratini, "Band dispersion and electronic lifetimes in crystalline organic semiconductors," Phys. Rev. Lett. **106**, 166403 (2011).

[268] A. Eiguren and C. Ambrosch-Draxl, "Complex quasiparticle band structure induced by electron-phonon interaction: Band splitting in the 1×1 H/W(110) surface," Phys. Rev. Lett. **101**, 036402 (2008).

[269] S. M. Story, J. J. Kas, F. D. Vila, M. J. Verstraete, and J. J. Rehr, "Cumulant expansion for phonon contributions to the electron spectral function," Phys. Rev. B **90**, 195135 (2014).

[270] B. Gumhalter, V. Kovač, F. Caruso, H. Lambert, and F. Giustino, "On the combined use of GW approximation and cumulant expansion in the calculations of quasiparticle spectra: The paradigm of Si valence bands," Phys. Rev. B **94**, 035103 (2016).

[271] N.-E. Lee, J.-J. Zhou, H.-Y. Chen, and M. Bernardi, "Next-to-leading order *ab initio* electron-phonon scattering," preprint (2019), arXiv:1903.08261 [cond-mat].

[272] M. Lazzeri, C. Attaccalite, L. Wirtz, and F. Mauri, "Impact of the electron-electron correlation on phonon dispersion: Failure of LDA and GGA DFT functionals in graphene and graphite," Phys. Rev. B **78**, 081406 (2008).

[273] A. Rao, M. W. B. Wilson, S. Albert-Seifried, R. Di Pietro, and R. H. Friend, "Photophysics of pentacene thin films: The role of exciton fission and heating effects," Phys. Rev. B **84**, 195411 (2011).

[274] H. Tamura, M. Huix-Rotllant, I. Burghardt, Y. Olivier, and D. Beljonne, "First-principles quantum dynamics of singlet fission: Coherent versus thermally activated mechanisms governed by molecular π stacking," Phys. Rev. Lett. **115**, 107401 (2015).

[275] Y. Yao, "Coherent dynamics of singlet fission controlled by nonlocal electron-phonon coupling," Phys. Rev. B **93**, 115426 (2016).

[276] S. Refaely-Abramson, F. H. da Jornada, S. G. Louie, and J. B. Neaton, "Origins of singlet fission in solid pentacene from an *ab initio* Green's function approach," Phys. Rev. Lett. **119**, 267401 (2017).

[277] S. R. Ellis, D. R. Dietze, T. Rangel, F. Brown-Altvater, J. B. Neaton, and R. A. Mathies, "Resonance Raman characterization of tetracene monomer and nanocrystals: Excited state lattice distortions with implications for efficient singlet fission," J. Phys. Chem. A **123**, 3863 (2019).

[278] D. Christiansen, M. Selig, G. Berghäuser, R. Schmidt, I. Niehues, R. Schneider, A. Arora, S. M. de Vasconcellos, R. Bratschitsch, E. Malic, and A. Knorr, "Phonon sidebands in monolayer transition metal dichalcogenides," Phys. Rev. Lett. **119**, 187402 (2017).

[279] G. Antonius and S. G. Louie, "Theory of the exciton-phonon coupling," preprint (2017), arXiv:1705.04245 [cond-mat].

[280] S. Shree, M. Semina, C. Robert, B. Han, T. Amand, A. Balocchi, M. Manca, E. Courtade, X. Marie, T. Taniguchi, K. Watanabe, M. M. Glazov, and B. Urbaszek, "Observation of exciton-phonon coupling in $MoSe_2$ monolayers," Phys. Rev. B **98**, 035302 (2018).

[281] J. Haber, S. Refaely-Abramson, G. Antonius, F. H. da Jornada, S. G. Louie, and J. B. Neaton, "Exciton-phonon interactions in organic crystals from first principles many-body perturbation theory," talk at APS March Metting 2019.

[282] A. M. Reilly, R. I. Cooper, C. S. Adjiman, S. Bhattacharya, A. D. Boese, J. G. Brandenburg, P. J. Bygrave, R. Bylsma, J. E. Campbell, R. Car, D. H. Case, R. Chadha, J. C. Cole, K. Cosburn, H. M. Cuppen, F. Curtis, G. M. Day, R. A. DiStasio Jr, A. Dzyabchenko, B. P. van Eijck, D. M. Elking, J. A. van den Ende, J. C. Facelli, M. B. Ferraro, L. Fusti-Molnar, C.-A. Gatsiou, T. S. Gee, R. de Gelder, L. M. Ghiringhelli, H. Goto, S. Grimme, R. Guo, D. W. M. Hofmann, J. Hoja, R. K. Hylton, L. Iuzzolino, W. Jankiewicz, D. T. de Jong, J. Kendrick, N. J. J. de Klerk, H.-Y. Ko, L. N. Kuleshova, X. Li, S. Lohani, F. J. J. Leusen, A. M. Lund, J. Lv, Y. Ma, N. Marom, A. E. Masunov, P. McCabe, D. P. McMahon, H. Meekes, M. P. Metz, A. J. Misquitta, S. Mohamed, B. Monserrat, R. J. Needs, M. A. Neumann, J. Nyman, S. Obata, H. Oberhofer, A. R. Oganov, A. M. Orendt, G. I. Pagola, C. C. Pantelides, C. J. Pickard, R. Podeszwa, L. S. Price, S. L. Price, A. Pulido, M. G. Read, K. Reuter, E. Schneider, C. Schober, G. P. Shields, P. Singh, I. J. Sugden, K. Szalewicz, C. R. Taylor, A. Tkatchenko, M. E. Tuckerman, F. Vacarro, M. Vasileiadis, A. Vazquez-Mayagoitia, L. Vogt, Y. Wang, R. E. Watson, G. A. de Wijs, J. Yang, Q. Zhu, and C. R. Groom, "Report on the sixth blind test of organic crystal structure prediction methods," Acta Cryst. B **72**, 439 (2016).

[283] A. Chernikov, O. Yaffe, B. Kumar, Y. Zhong, C. Nuckolls, and T. F. Heinz, "Spectroscopic study of anisotropic excitons in single crystal hexacene," J. Phys. Chem. Lett. **5**, 3632 (2014).

[284] P. Giannozzi, S. Baroni, N. Bonini, M. Calandra, R. Car, C. Cavazzoni, D. Ceresoli, G. L. Chiarotti, M. Cococcioni, I. Dabo, A. Dal Corso, S. de Gironcoli, S. Fabris, G. Fratesi, R. Gebauer, U. Gerstmann, C. Gougoussis, A. Kokalj, M. Lazzeri, L. Martin-Samos, N. Marzari, F. Mauri, R. Mazzarello, S. Paolini, A. Pasquarello, L. Paulatto, C. Sbraccia, S. Scandolo, G. Sclauzero, A. P. Seitsonen, A. Smogunov, P. Umari, and R. M. Wentzcovitch, "QUANTUM ESPRESSO: A modular and open-source software project for quantum simulations of materials," J. Phys. Condens. Matter **21**, 395502 (2009).

[285] H. J. Monkhorst and J. D. Pack, "Special points for Brillouin-zone integrations," Phys. Rev. B **13**, 5188 (1976).

[286] M. Fuchs and M. Scheffler, "*Ab initio* pseudopotentials for electronic structure calculations of poly-atomic systems using density-functional theory," Comput. Phys. Commun. **119**, 67 (1999).

[287] M. Callsen and I. Hamada, "Assessing the accuracy of the van der Waals density functionals for rare-gas and small molecular systems," Phys. Rev. B **91**, 195103 (2015).

[288] J. P. Perdew, A. Ruzsinszky, G. I. Csonka, O. A. Vydrov, G. E. Scuseria, L. A. Constantin, X. Zhou, and K. Burke, "Restoring the density-gradient expansion for exchange in solids and surfaces," Phys. Rev. Lett. **100**, 136406 (2008).

[289] I. Hamada and S. Yanagisawa, "Pseudopotential approximation in van der Waals density functional calculations," Phys. Rev. B **84**, 153104 (2011).

[290] `http://www.quantum-espresso.org/`.

[291] K. F. Garrity, J. W. Bennett, K. M. Rabe, and D. Vanderbilt, "Pseudopotentials for high-throughput DFT calculations," Comput. Mater. Sci. **81**, 446 (2014).

[292] G. Kresse and D. Joubert, "From ultrasoft pseudopotentials to the projector augmented-wave method," Phys. Rev. B **59**, 1758 (1999).

[293] J. Deslippe, G. Samsonidze, D. A. Strubbe, M. Jain, M. L. Cohen, and S. G. Louie, "BerkeleyGW: A massively parallel computer package for the calculation of the quasiparticle and optical properties of materials and nanostructures," Comput. Phys. Commun. **183**, 1269 (2012).

[294] X. Gonze, B. Amadon, P. Anglade, J. Beuken, F. Bottin, P. Boulanger, F. Bruneval, D. Caliste, R. Caracas, M. Côté, T. Deutsch, L. Genovese, P. Ghosez, M. Giantomassi, S. Goedecker, D. R. Hamann, P. Hermet, F. Jollet, G. Jomard, S. Leroux, M. Mancini, S. Mazevet, M. J. T. Oliveira, G. Onida, Y. Pouillon, T. Rangel, G.-M. Rignanese, D. Sangalli, R. Shaltaf, M. Torrent, M. J. Verstraete, G. Zerah, and J. W. Zwanziger, "ABINIT: First-principles approach to material and nanosystem properties," Comput. Phys. Commun. **180**, 2582 (2009).

[295] R. Mason, "The crystallography of anthracene at 95 °K and 290 °K," Acta Cryst. **17**, 547 (1964).

[296] S. B. Zhang, D. Tománek, M. L. Cohen, S. G. Louie, and M. S. Hybertsen, "Evaluation of quasiparticle energies for semiconductors without inversion symmetry," Phys. Rev. B **40**, 3162 (1989).

[297] C. J. Craven, P. D. Hatton, C. J. Howard, and G. S. Pawley, "The structure and dynamics of solid benzene. I. A neutron powder diffraction study of deuterated benzene from 4 K to the melting point," J. Chem. Phys. **98**, 8236 (1993).

[298] T. Siegrist, C. Besnard, S. Haas, M. Schiltz, P. Pattison, D. Chernyshov, B. Batlogg, and C. Kloc, "A polymorph lost and found: The high-temperature crystal structure of pentacene," Adv. Mater. **19**, 2079 (2007).

[299] S. Haas, "Crystal structure analysis and trap spectroscopy in organic semiconducting crystals," (Eidgenössische Technische Hochschule ETH Zürich, 2006).

[300] A. Santoro and A. D. Mighell, "Determination of reduced cells," Acta Cryst A **26**, 124 (1970).

[301] N. Marzari and D. Vanderbilt, "Maximally localized generalized Wannier functions for composite energy bands," Phys. Rev. B **56**, 12847 (1997).

[302] WanT code by A. Ferretti, B. Bonferroni, A. Calzolari, and M. Buongiorno Nardelli, (http://www.wannier-transport.org).

[303] A. Calzolari, N. Marzari, I. Souza, and M. Buongiorno Nardelli, "*Ab initio* transport properties of nanostructures from maximally localized Wannier functions," Phys. Rev. B **69**, 035108 (2004).

[304] W. Setyawan and S. Curtarolo, "High-throughput electronic band structure calculations: Challenges and tools," Comput. Mater. Sci. **49**, 299 (2010).

Appendix A

Appendix for Electronic structure of acenes

A.1 Computational parameters

Our DFT calculations in Chapter 3 are performed with the Quantum ESPRESSO (QE) package [284], unless otherwise indicated. Γ-centered Monkhorst-Pack **k**-point grids are used for all calculations [285]. For geometry optimizations, where Hellmann-Feynman forces and stress tensor components are minimized, we use a number of **k**-points along each crystallographic direction corresponding to a spacing of $\sim$3.3 Bohr^{-1} between neighboring points in reciprocal space. All Hellmann-Feynman forces are converged to 1×10^{-5} Ry/Bohr and total energies are converged to 1×10^{-5} Ry. We use a plane wave basis with a kinetic energy cutoff of 55 Ry. Taken together, these choices lead to total energies converged to 1 meV per atom.

For calculations with vdW-DF functionals, we use the ultrasoft pseudopotentials (USPPs) given in Ref. [131]; for vdW approaches based on interatomic pairwise potentials, we use Fritz-Haber-Institut (FHI) normconserving (NC) pseudopotentials (PPs) [286] because these corrections are not compatible with USPPs in the present version of QE. Following a prior successful approach with vdW density functionals [287], we use Perdew-Burke-Ernzerhof (PBE) [114] PPs for DF2 and DF and PBEsol [288] PPs for DF-cx [127]. (In principle, native vdW-PPs have begun to be explored with vdW-DFs, and we relegate the evaluation of such pseudopotentials for acenes to future work [289].) The latter choice is based on the fact that the exchange functional of DF-cx is much closer in form to PBEsol than to PBE. A test study reveals that the results are not significantly affected by this choice: for naphthalene, the lattice parameters (and volume) obtained using DF-cx with PBE PPs differ by no more than 1.2 % (0.2 %) from standard DF-cx calculations.

To test the reliability of our PP choice, we benchmarked our calculations of solid naphthalene (see section 3.2.1 for details) against other codes and pseudopotentials. The lattice parameters obtained with our USPPs, the FHI NC PPs available from the QE website [290],

and Garrity-Bennett-Rabe-Vanderbilt (GBRV) [291] USPPs agree within 0.3 %. Additionally, we relaxed the structure of benzene with the VASP code, using projector-augmented waves [292] with vdW-DF2, obtaining lattice parameters in agreement with those obtained from QE to within 0.4 %. Note that a higher, 110 Ry cutoff was used for the FHI NC PPs calculations. The GBRV USPPs were constructed to be exceptionally hard and required a plane-wave cutoff of 350 Ry to achieve a convergence threshold of 1 meV/atom.

Our MBPT calculations are performed with the BerkeleyGW package [293]. Capitalizing on its efficient and highly parallel diagonalization techniques, Kohn-Sham starting-point wave functions and eigenenergies for input into MBPT are generated with the ABINIT software suite [294].

In some of the calculations, we deliberately use experimental lattice constants to study the accuracy of the *GW*-BSE approach independent of geometry. For consistency, we use room-temperature experimental data for all acenes [179, 187, 190, 197, 295] except for hexacene, where crystallographic data are only available at $T = 123\,\mathrm{K}$ [191]. For pentacene, we consider the thin-film polymorph (denoted below as P3) because it is the one most commonly measured in experiment (see section 3.2.1). In other calculations, where we explore the impact of the geometry, we use the optimized geometry obtained from the DFT calculation.

We note that BerkeleyGW requires NC PPs as input, but we use USPPs for lattice optimizations. Prior to the MBPT calculations, we relaxed the internal coordinates using NC PPs within PBE, with the lattice parameters held fixed at their optimized value. This was found to result in negligible differences for both geometry and excited-state properties. We followed the same internal relaxation procedure when using experimental lattice vectors, following Ref. [83].

Our *GW* calculations involve a number of convergence parameters, which are set to assure that quasiparticle gaps, highest-occupied molecular orbital (HOMO) energies, and band-edge energies for crystals and gas-phase molecules are converged to ∼0.1 eV. Our dielectric function is extended to finite frequency using the generalized plasmon-pole (GPP) model of Hybertsen and Louie [58], modified to handle non-centrosymmetric systems by Zhang et al. [296]. We use an energy cutoff of 10 Ry to truncate the sums in $\mathbf{G}$ space used for the calculation of the polarizability. We sum over a number of unoccupied bands equivalent to an energy range of 30 eV. Response functions and Σ are evaluated on $\mathbf{k}$-point meshes selected to lead to a spacing of $\sim 1.6\,\mathrm{Bohr}^{-1}$ in reciprocal space.

For our BSE calculations, the BSE coupling matrix is constructed with 8 valence × 8 conduction bands, sufficient to converge the transition energies involving the lowest states, as shown explicitly in Fig. A.3. Two $\mathbf{k}$-point meshes are used: a coarse $\mathbf{k}$-point mesh for the BSE kernel and a fine $\mathbf{k}$-point mesh to calculate the low-lying excited states. Coarse $\mathbf{k}$-meshes are chosen to be the same as those used in the *GW* step, while fine meshes are the same as in the geometry optimization. These $\mathbf{k}$-meshes are explicitly provided in Table A.3.

A.2 Structural properties: Benchmarking of vdW functionals

In this Appendix, we provide detailed information on the structural data obtained with different methods for the acene family of crystals. As in the main text, we consider standard DFT methods (LDA and PBE) and different vdW methods: D2, TS, DF1, DF2, and DF-cx.

Throughout, we make use of CSD [181] data to benchmark our results. For the smallest acenes, low-temperature data ($T \leq 14\,\mathrm{K}$) are available in the CSD under the entries BENZEN14, NAPHTA31, and ANTCEN16, from Refs. [187–189]. Reference [297] also reports low-temperature data for benzene, consistent with the data of Ref. [188]. For tetracene-P_1 and pentacene-P_2, we extrapolate experimental data from Refs. [298, 299] to 0 K, as shown in Fig. A.1. Note that we assign the tetracene structures of Ref. [299] to its P_1 polymorph.[1] For other pentacene polymorphs and hexacene, in the absence of sufficient low-temperature data that would allow for extrapolation to 0 K, we compare to the lowest-temperature experimental data available from Refs. [179, 190, 191], also found in the CSD as PENCEN, PENCEN10, and ZZZDKE01. We emphasize that only by extrapolating experimental data to 0 K do we observe consistent trends in the comparison of our relaxed geometries for the various DFT methods used here. In the main text, we have also compared our data to experimental cohesive energies. These are taken from Ref. [90], in which temperature contributions have been removed. A complete set of experimental and calculated lattice parameters and cohesive energies is given in Tables A.1 and A.2, respectively. Lattice parameters are usually found in literature following old conventions. However, recent data use the so-called Niggli [300] (or reduced) lattice parameters. For completeness, we present both conventions in Table A.2. Finally, in Fig. A.2 we present a comparison of theory and experiment for the angles that characterize the herringbone structure in the three pentacene polymorphs. Here, all DF approximations predict angles in good agreement with experiment. At the experimental resolution and temperature, we cannot conclude definitively which DF version performs best for angle prediction, but see no reason for trends different from those reported in the main text.

[1] The tetracene lattice parameters reported in the Ph.D. thesis of Haas [299] at 175 K almost perfectly match P_1 at 180 K as reported in Ref. [161] (the volumes agree within 0.5 %). Further, by cooling the sample from 175 to 106 K, Haas reports a slight reduction in volume, as shown in Fig. A.1 of our paper. Hence, we can assign Haas's structures to the P_1 polymorph. Note that the P_2 polymorph has an appreciably smaller c lattice vector (12.3 Å) than the P_1 phase (∼12.5 Å).

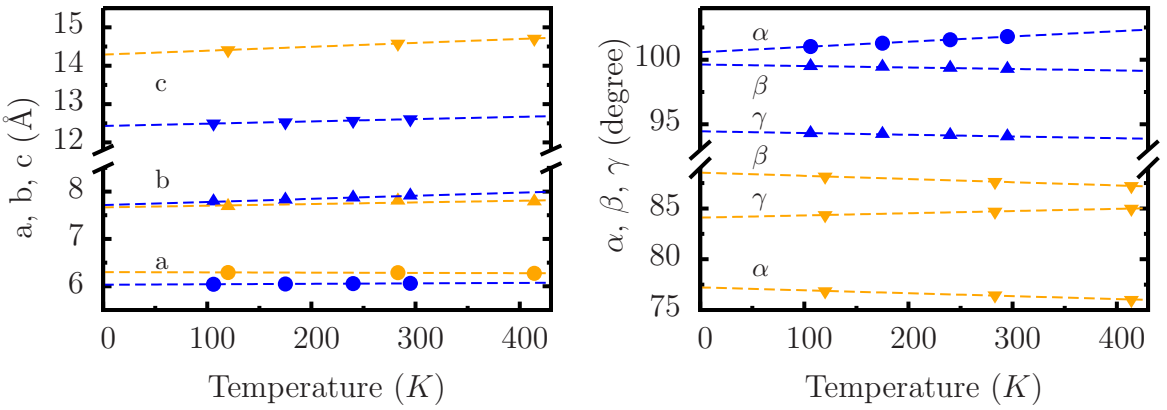

Figure A.1: Extrapolation of unit-cell geometry to 0 K: Experimental lattice parameters and angles of tetracene P_1 (blue) are extracted from Ref. [299], and those of pentacene P_2 (orange) are extracted from Ref. [298], also labeled as PENCEN06-PENCEN08 in the CSD. These are fitted to linear functions of the temperature (dashed lines). The fits possess an average root mean square of 7×10^{-3} Å and 0.05 Å and 0.02° and 0.05° for tetracene P_1 and pentacene P_2 , respectively.

Table A.1: Cohesive energies of the acenes. Calculated ($E_{\text{coh.}}$) and experimental ($E_{\text{coh.}}^{\text{Exp.}}$) cohesive energies are tabulated. Experimental cohesive energies are taken from Ref. [90]. Mean average error (MAE) and mean average percent error (MA%E) are shown for all functionals: $\text{MAE} = \sum_i^{N_m} \left| E_{\text{coh.},i}^{\text{Exp.}} - E_{\text{coh.},i} \right| / N_m$ and $\text{MA\%E} = \sum_i^{N_m} \left| E_{\text{coh.},i}^{\text{Exp.}} - E_{\text{coh.},i} \right| / E_{\text{coh.},i} / N_m \times 100$, where N_m is the total number of crystals. The asterisk indicates that TS data are taken from Ref. [90]. All energies in eV.

	PBE	LDA	D2	TS*	DF1	DF2	DF-cx	Exp.
Benzene	0.12	0.59	0.73	0.69	0.64	0.60	0.61	0.52
Naphthalene	0.15	0.76	1.16	1.04	0.93	0.86	0.92	0.82
Anthracene	0.19	0.97	1.61	1.39	1.24	1.16	1.23	1.13
Tetracene	0.25	1.21	2.10		1.56	1.42	1.56	
Pentacene P_1	0.30	1.46	2.61		1.88	1.76	1.87	
Pentacene P_2	0.30	1.48	2.63		1.88	1.76	1.92	
Pentacene P_3	0.31	1.42	2.61		1.88	1.79	1.87	
Hexacene	0.36	1.82	2.18		2.21	2.09	2.30	
MAE	0.66	0.09	0.35	0.22	0.11	0.05	0.10	
MA%E	80	11	42	28	16	8	13	

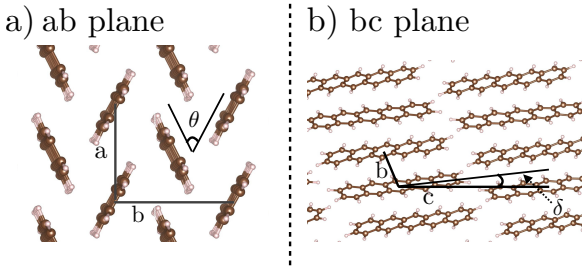

Pentacene:

		DF1	DF2	DF-cx	Exp.
P_1	θ	50	47	47	53
	δ	12	12	12	12
P_2	θ	53	51	50	51
	δ	15	14	16	14
P_3	θ	55	55	53	54
	δ	5	4	4	4

Figure A.2: Angles characterizing the pentacene herringbone structure: (a) Along the *ab* plane, the herringbone angle θ is the angle between the two distinct molecules. (b) Along the *bc* plane, δ is the angle between the c axis and the long axis of the molecule. (Right table) Angles calculated by different DF methods are compared to experimental data from Refs. [179, 190, 298], labeled as PENCEN, PENCEN06, and PENCEN10 in the CSD, and measured at 205 K, 120 K, and 293 K for pentacene P_1, P_2, and P_3, respectively. While θ is almost constant for all polymorphs ($\theta \sim 50^\circ - 54^\circ$), δ is not. 50°–54° We use Niggli unit-cell conventions and all angles are in degrees.

Table A.2: Structural parameters for the acene crystal series. Lattice parameters (using old conventions) a, b, and c (in Å), lattice angles α, β, and γ (in degrees), and unit-cell volumes (in Å^3) are calculated from force and stress relaxation within different DFT approximations. Niggli lattice parameters (denoted by a prime) are also shown wherever they differ from old-convention ones. Experimental lattice parameters measured at low temperature T are also shown. For pentacene, three different polymorphs are considered, labeled as P_1, P_2 , and P_3. The asterisk denotes the following: where possible, lattice parameters are extrapolated to 0 K (see text for details). Mean absolute errors (MAE) and mean absolute percentage errors (MA%E) with respect to experimental lattice parameters are also shown: In the error evaluation, we only considered experimental data with $T \leq 16$ K or data extrapolated to 0 K. For brevity, symmetry-imposed angles are omitted. TS data taken from Ref. [169] for benzene and from Refs. [89, 187–189] for longer acenes. Experimental data are taken from Refs. [179, 187–191, 299].

	PBE	LDA	D2	TS*	DF1	DF2	DF-cx	Exp.
Benzene								$T=4$ K
a	7.46	6.37	6.43	6.95	7.01	6.87	6.73	6.70
b	8.11	7.06	7.12	7.58	7.49	7.39	7.40	7.36
c	9.93	8.96	9.05	9.51	9.89	9.41	9.49	9.37
Ω	601.1	403.0	414.4	500.8	518.4	477.9	473.0	461.8
Naphthalene								$T=5$ K
a	8.99	7.74	7.79	8.12	8.48	8.22	8.06	8.08
b	6.31	5.76	5.79	5.90	6.06	5.97	5.91	5.93
c	9.13	8.37	8.44	8.65	8.79	8.57	8.75	8.63
β	122.1	125.5	125.3	124.2	123.3	122.9	124.4	124.7
Ω	438.9	304.0	310.4	342.2	377.9	353.3	344.4	340.4
a'	6.31	5.76	5.79	5.90	6.06	5.97	5.91	5.93
b'	8.77	7.40	7.47	7.85	8.21	8.03	7.87	7.78
c'	8.99	7.74	8.44	8.12	8.48	8.22	8.06	8.08
α'	118.1	112.9	121.7	114.5	116.4	116.4	113.4	114.1
Ω'	438.9	304.0	310.4	342.2	377.9	353.3	344.4	340.4
Anthracene								$T=16$ K
a	9.63	8.10	8.13	8.40	8.75	8.56	8.38	8.37
b	6.35	5.80	5.85	5.91	6.12	6.02	5.96	6.00
c	10.14	10.82	10.89	11.12	11.11	11.07	11.23	11.12
β	109.7	126.5	126.5	125.2	123.4	124.2	125.6	125.4
Ω	584.4	408.9	416.6	451.0	496.7	471.2	456.5	455.2
a'	6.35	5.80	5.85	5.91	6.12	6.02	5.96	6.00
b'	9.63	8.10	8.13	8.40	8.75	8.56	8.38	8.37
c'	10.14	8.86	8.91	9.31	9.65	9.44	9.32	9.26
α'	109.7	100.9	100.7	102.4	105.9	104.3	101.4	102.0
Ω'	584.4	408.9	416.6	451.0	496.7	471.2	456.5	455.2

Table A.2 (continued)

	PBE	LDA	D2	TS*	DF1	DF2	DF-cx	Exp.	
Tetracene								$T=0\,\mathrm{K}^*$	$T=106\,\mathrm{K}$
a	6.35	5.89	5.93	6.05	6.15	6.05	6.05	6.03	6.04
b	9.26	7.43	7.43	7.71	8.21	7.92	7.69	7.71	7.79
c	13.60	12.45	12.55	13.03	13.34	13.16	12.93	12.88	12.95
α	72.6	78.4	78.7	77.7	75.1	75.6	78.0	77.6	77.3
β	71.5	72.8	72.5	71.9	71.2	72.0	72.6	72.1	72.1
γ	86.2	85.1	85.1	85.7	86.4	86.0	85.5	85.5	85.7
Ω	723.2	510.0	516.6	564.1	616.1	579.9	561.3	557.7	566.1
a'	6.35	5.89	5.93	6.05	6.15	6.05	6.05	6.03	6.04
b'	9.26	7.43	7.43	7.71	8.21	7.92	7.69	7.71	7.68
c'	13.06	12.09	12.16	12.53	12.76	12.67	12.53	12.43	12.50
α'	106.2	99.5	99.2	100.7	103.8	103.0	100.2	100.6	101.0
β'	99.0	100.5	100.2	99.2	98.3	99.0	100.1	99.6	99.5
γ'	93.8	94.9	94.9	94.3	93.6	94.0	94.5	94.5	94.3
Ω'	723.2	510.0	516.6	564.1	616.1	579.9	561.3	557.7	566.1
Pentacene P_1								$T=295\,\mathrm{K}$	
a	9.14	7.37	7.36	7.66	8.17	7.90	7.59	7.90	
b	6.33	5.97	6.00	6.04	6.16	6.08	6.07	6.06	
c	16.13	15.54	15.64	15.85	15.99	15.83	15.98	16.01	
α	101.6	103.8	103.5		100.7	101.1	102.0	101.9	
β	110.6	113.9	114.0		111.2	111.8	112.5	112.6	
γ	86.2	84.7	84.7		85.8	86.1	85.7	85.8	
Ω	856.1	607.0	613.5	664.1	736.8	692.7	666.0	692.4	
a'	6.33	5.97	6.00		6.16	6.08	6.07	6.06	
b'	9.14	7.37	7.36		8.17	7.90	7.59	7.90	
c'	15.49	14.23	14.33		15.09	14.84	14.84	14.88	
α'	102.9	83.5	94.0		99.1	97.9	95.7	96.7	
β'	99.8	78.1	102.0		99.0	99.7	100.7	100.5	
γ'	93.8	84.7	95.3		94.2	93.9	94.3	94.2	
Ω'	856.1	607.0	613.5	664.1	736.8	692.7	666.0	692.4	
Pentacene P_2								$T=0\,\mathrm{K}^*$	$T=120\,\mathrm{K}$
a	6.52	6.18	6.25	6.13	6.45	6.33	6.29	6.30	6.29
b	8.91	7.27	7.24	7.68	8.07	7.81	7.52	7.67	7.69
c	15.16	13.80	13.85	14.53	14.69	14.49	14.35	14.29	14.41
α	71.4	78.1	78.5	77.3	74.7	76.2	77.8	77.2	76.9
β	87.6	89.4	89.3	87.4	88.5	88.1	88.7	88.5	88.2
γ	84.9	83.7	83.5	84.7	84.8	84.6	84.1	84.1	84.4
Ω	830.7	603.0	609.8	663.9	734.0	693.5	660.3	669.4	674.7
Pentacene P_3								$T=293\,\mathrm{K}$	
a	6.16	5.71	5.78	6.65	6.04	5.88	5.92	5.96	
b	8.87	7.05	7.01	6.92	7.94	7.76	7.36	7.60	

Table A.2 (continued)

	PBE	LDA	D2	TS*	DF1	DF2	DF-cx	Exp.
c	15.95	15.29	15.41	16.27	15.54	15.53	15.68	15.61
α	81.4	82.5	82.8		81.9	80.8	81.8	81.2
β	87.7	89.8	90.0		87.4	87.9	87.2	86.6
γ	90.0	90.0	90.0		89.4	89.7	89.7	89.8
Ω	861.1	610.9	619.2	746.3	737.2	699.0	675.9	697.0
Hexacene								$T = 123\,\mathrm{K}$
a	6.60	6.47	6.48		6.43	6.34	6.61	6.31
b	9.10	6.85	6.85		8.04	7.84	7.05	7.70
c	17.30	15.64	15.71		16.79	16.49	16.14	16.48
α	75.1	95.2	95.1		101.1	99.9	95.8	98.8
β	85.4	92.0	92.1		90.6	91.3	91.5	91.2
γ	84.9	97.1	97.2		95.4	95.5	96.8	95.8
Ω	998.4	684.0	688.8		848.3	803.3	743.3	785.9
MAE [Å]	0.76	0.29	0.25	0.09	0.28	0.11	0.06	
MA%E	9	3	3	1	3	1	1	

Table A.3: **k**-point mesh size used in the BSE calculations for the acene crystals.

	k-grid size	
	coarse	fine
Benzene	$4 \times 3 \times 5$	$8 \times 6 \times 9$
Naphthalene	$4 \times 5 \times 4$	$7 \times 10 \times 7$
Anthracene	$4 \times 5 \times 3$	$7 \times 10 \times 5$
Tetracene	$5 \times 4 \times 2$	$10 \times 8 \times 5$
Pentacene-P1	$5 \times 4 \times 2$	$10 \times 8 \times 4$
Pentacene-P2	$4 \times 4 \times 2$	$10 \times 8 \times 4$
Pentacene P3	$5 \times 4 \times 2$	$10 \times 8 \times 4$
Hexacene	$5 \times 4 \times 2$	$9 \times 9 \times 4$

A.3 Convergence parameters of GW-BSE calculations

In Table A.3, we show the size of the coarse and fine **k**-point grids used in the BSE calculations for the acene crystals. These are generated as:

$$N_k^i = a_0/|a_i|d, \tag{A.1}$$

where the index i indicates the crystallographic direction, a_i is the lattice vector along i, $a_0 = 11.3\,\text{Å}$ and d equals 5 and 10 for the coarse and fine grids, respectively. The **k**-point meshes shown here correspond to the structures relaxed within DF-cx, when relaxing with other functionals the number of **k**-points may change according to Eq. (A.1)

In Fig. A.3 we show convergence tests on the number of conduction/valence bands in the BSE Hamiltonian. We find that a BSE Hamiltonian of 8×8 valence and conduction bands assures a convergence of better than 0.1 eV for the low-lying excited state energies of the acene crystals considered in this work.

A.4 Electronic band structures of acenes

In Figs. A.4 and A.5, DFT and G_0W_0 band structures for the acenes are shown. As explained in Chapter 3 G_0W_0 is the method of choice for small to medium size acenes. For the longest acenes: hexacene and probably pentacene, eigenvalue–self-consistent GW (evGW) gives more accurate band structures [158]. Hence, for these crystals, their corresponding evGW band structures are shown as well. All band structures are interpolated using Maximally-Localized Wannier Functions (MLWFs) [301] with the WanT package [302, 303]. DOS are also interpolated with MLWFs to a dense mesh of $40 \times 40 \times 40$ **k**-points for benzene and $40 \times 40 \times 20$ **k**-points for the rest of acenes.

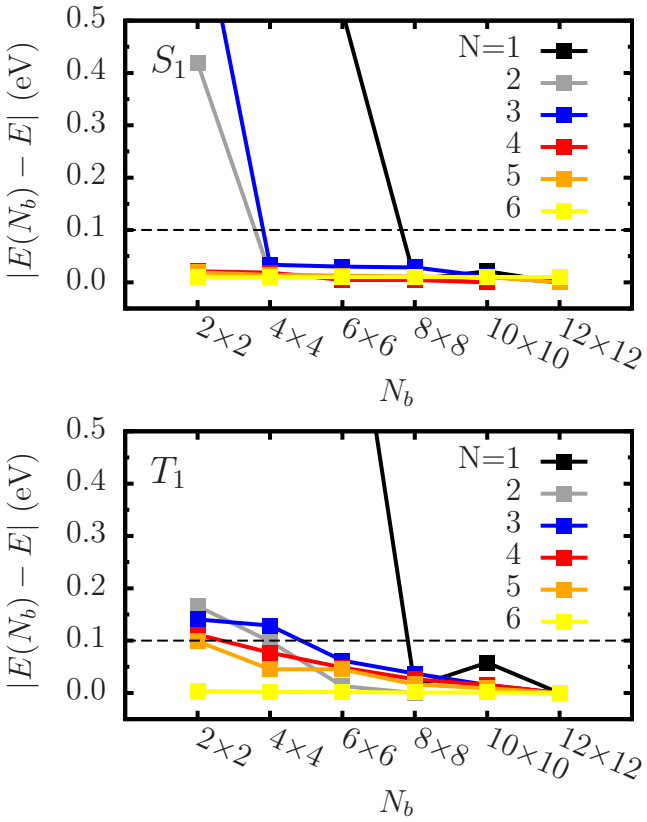

Figure A.3: Convergence on the number of bands in the BSE calculations of the singlet (left panel) and the triplet (right panel) energies of the acene crystals, from benzene $N = 1$ to hexacene $N = 6$. A number of valence $\times$ conduction bands (N_b) is set to construct the BSE Hamiltonian, and after a full-diagonalization the singlet/triplet eigenvalues $E(N_b)$ are obtained. The excitation energy obtained with $N_b = 12 \times 12$ is set as the reference (E), and the energy difference of the BSE eigenvalues with respect to the reference is plotted for increasing N_b. Our convergence threshold of 0.1 eV is shown in a dashed horizonal black-line, as a guide to the eyes. Here we use the geometries relaxed with DF-cx.

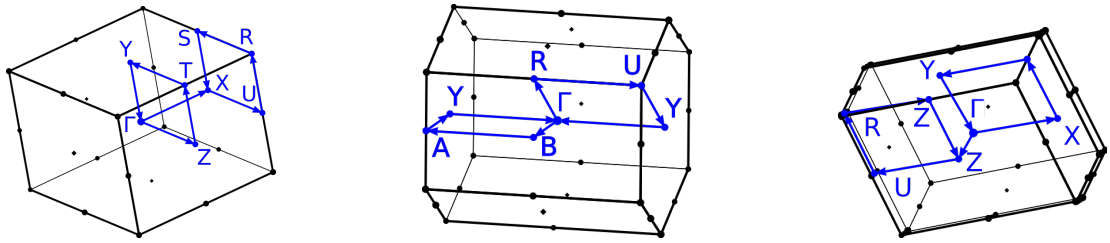

(a) Orthorhombic *Pbca* (b) Monoclinic $P2_1/a$ (c) Triclinic $P\bar{1}$

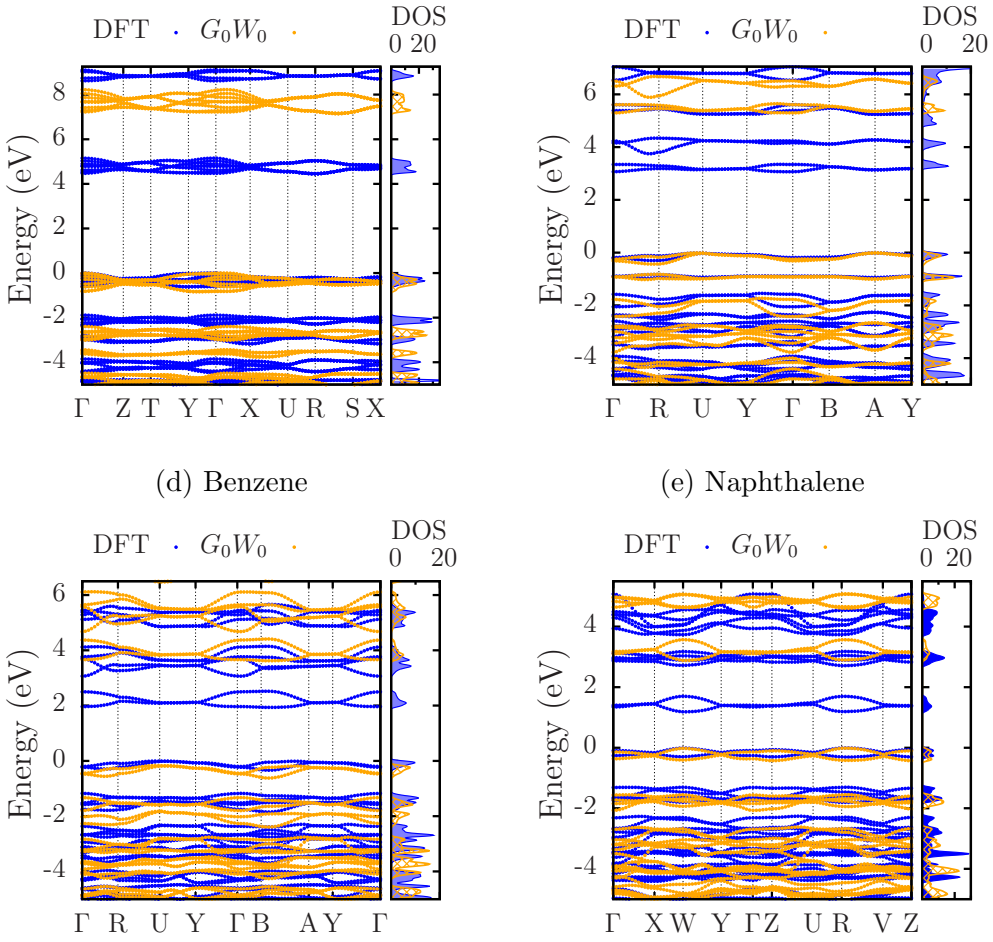

(d) Benzene (e) Naphthalene

(f) Anthracene (g) Tetracene

Figure A.4: Calculated energy band structures for small to medium-sized acenes. (a-c) Brillouin zones for the three different space groups are indicated: Benzene is orthorhombic *Pbca*, Naphthalene and Anthracene are monoclinic $P2_1/a$, and longer acenes are Triclinic $P\bar{1}$. (d-g) Calculated DFT (in blue) and G_0W_0 (in orange) band structures and DOS in $2e^-$/cell units. Fermi levels are at 0 eV.

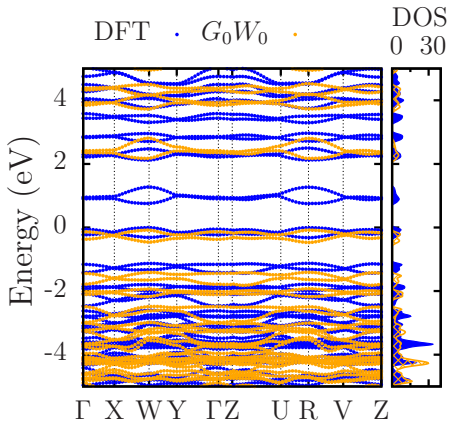

(a) Pentacene-P_1

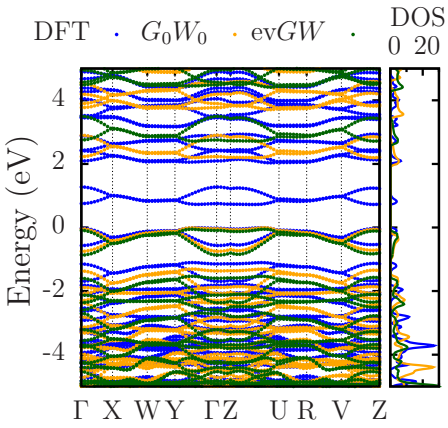

(b) Pentacene-P_3

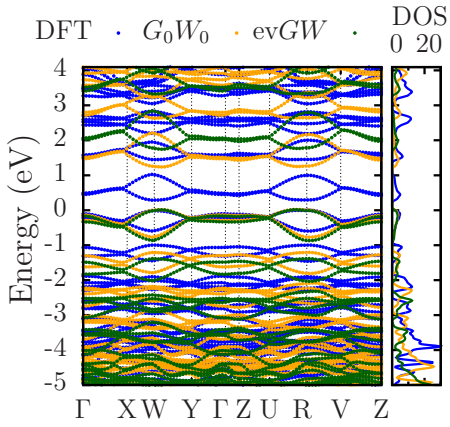

(d) Hexacene

Figure A.5: Calculated energy band structures for pentacene and hexacene. Band structures and DOS in units of $2e^-$/cell. obtained with two GW flavors are shown: standard G_0W_0 (in orange) and evGW (in green). As discussed in Ref. [158], for hexacene, and probably for pentacene, evGW gives QP band structures in agreement to experimental data, while G_0W_0 slightly underestimates fundamental gaps. The Brillouin zones are shown in Fig. A.4. Fermi levels are at 0 eV.

Appendix B

Appendix for Lattice vibrations of naphthalene

B.1 Computational parameters

For all phonon calculations in Chapter 4, we use density functional theory with a plane wave basis and norm-conserving Troullier-Martins pseudopotentials [286], employing the software suite Quantum ESPRESSO v5.1.1 [284]. We perform calculations with the LDA, PBE, and vdW-DF-cx functionals. A kinetic energy cutoff of 110 Ry converges the total energy for all three functionals to within 1 meV/atom. Calculations with vdW-DF-cx use the PBE pseudopotentials.

As starting geometry we use the experimental crystal structure of naphthalene measured at 5 K [187], available at the Cambridge Structural Database [181] (ID: NAPHTHA31). Naphthalene belongs to the $P2_1/a$ space group, and contains two molecules per unit cell, each of which are situated at inversion centers. The molecules form a layered herringbone structure, with layers stacked in the c-direction. The naphthalene unit cell is depicted in Fig. 4.1.

Prior to the phonon calculations, all internal coordinates are relaxed again, while keeping the lattice parameters fixed and the symmetry constrained, using a smaller Monkhorst-Pack grid of $2 \times 4 \times 2$ (corresponding to the mesh used in our phonon calculations; see below). The Hellmann-Feynman forces are converged to 2×10^{-5} Ry/Bohr and the total energy to 10^{-8} Ry. To ensure accurate forces, the convergence threshold for all self-consistent calculations is 10^{-12} Ry.

Phonon band structures are calculated within a harmonic approximation via a finite-differences (FD) approach with a 2×4×2 supercell, using Γ-point sampling. For zone-center phonon calculations, a single primitive cell with a centered Monkhorst-Pack **k**-grid of 2×4×2 is used, commensurate with the supercell size above. We displace each atom by 0.001 25 Å to generate the force constants in our FD approach. The frequency spectrum at each **q**-point is obtained by diagonalizing the Fourier transform of the real-space force-constant matrix.

The acoustic sum rule is enforced. For LDA and PBE, our FD approach is in quantitative agreement with density-functional perturbation theory. Mode numbering throughout this work includes the three acoustic modes, i.e., the first non-zero mode at Γ is designated as "mode 4". We use 1.007 94 u for the mass of the hydrogen atoms in perprotonated (d0) naphthalene or 2.014 10 u for those in perdeuterated (d8) naphthalene, depending on the hydrogen isotope present in the experiment we compare to. In plotting our phonon band structures, we follow Ref. [219] for our high-symmetry points and lines in **q**-space; however, the labels are adopted from the more contemporary Ref. [304]. As the experimental spectrum by Natkaniec et al. [219] was obtained at 6 K, we assume anharmonic effects are negligible, and our comparison with the FD method within the harmonic approximation is valid.

Table B.1: Crystal coordinates of the unique sites in crystalline naphthalene after relaxation of internal coordinates with DF-cx and LDA at relaxed, and PBE at experimental lattice parameters. Lattice and relaxation parameters are given in the text.

	DF-cx@$\Omega_{\text{DF-cx}}$			PBE@Ω_{PBE}			LDA@Ω_{LDA}		
C	0.0813	0.0191	0.3236	0.0869	0.0213	0.3302	0.0820	0.0214	0.3359
C	0.1122	0.1643	0.2192	0.1153	0.1648	0.2225	0.1136	0.1691	0.2280
C	0.0482	0.1065	0.0370	0.0484	0.1062	0.0369	0.0489	0.1091	0.0387
C	0.0770	0.2528	0.9260	0.0743	0.2508	0.9222	0.0779	0.2581	0.9241
C	0.9858	0.8087	0.2504	0.9912	0.8117	0.2573	0.9855	0.8059	0.2594
H	0.1306	0.0675	0.4632	0.1382	0.0702	0.4719	0.1324	0.0729	0.4825
H	0.1851	0.3272	0.2745	0.1883	0.3265	0.2777	0.1880	0.3379	0.2863
H	0.1507	0.4150	0.9830	0.1477	0.4119	0.9787	0.1532	0.4260	0.9847
H	0.9608	0.6947	0.3335	0.9686	0.6993	0.3429	0.9596	0.6885	0.3459

B.2 Phonon frequencies

Table B.2: All calculated frequencies for protonated naphthalene at Γ compared to experimental infrared (IR) and Raman spectra taken from Ref. [216]. The calculated mode symmetries in the second column inform the matching to the IR and Raman frequencies (X_u for IR and X_g for Raman). The LDA and PBE frequencies have been ordered to correspond to the respective DF-cx mode with the largest projection (and hence same symmetry). All frequencies are in cm^{-1}.

mode	sym.	DF-cx @$\Omega_{\text{DF-cx}}$	IR	Raman	LDA @Ω_{LDA}	PBE @Ω_{exp}
4	B_g	53.7	–	56	49.5	62.8
5	A_u	54.2	–	–	57.6	68.5
6	A_g	63.1	–	69	58.4	78.0
7	B_u	72.9	–	–	75.4	91.0
8	B_g	78.7	–	81	81.9	94.1
9	A_g	82.4	–	88	86.1	102.1
10	A_u	100.5	–	–	110.7	122.5
11	A_g	121.2	–	120	113.6	128.8
12	B_g	139.7	–	141	135.6	153.4
13	B_u	177.1	176	–	177.3	181.7
14	A_u	195.1	–	–	196.6	199.2
15	A_u	213.1	–	–	211.1	224.7
16	B_u	216.3	–	–	214.5	222.0
17	B_u	357.8	362	–	358.5	360.4
18	A_u	360.2	400	–	361.4	365.0
19	B_g	387.5	–	390	388.9	392.4
20	A_g	393.1	–	–	393.8	396.8
21	A_g	464.4	–	467	468.0	469.9
22	A_u	469.7	–	–	473.2	473.8
23	B_g	470.0	–	–	473.9	474.6
24	B_u	480.1	478	–	482.5	486.4
25	B_g	505.2	–	–	508.3	512.0
26	A_g	506.4	–	–	509.4	513.6
27	B_g	508.8	–	509	512.0	516.5
28	A_g	509.6	–	514	513.3	518.3
29	B_u	615.5	581	–	619.2	621.2
30	A_u	617.7	618	–	621.2	623.7
31	A_u	624.1	–	–	629.0	635.3
32	B_u	629.2	–	–	633.6	640.2
33	A_g	715.0	–	–	720.9	712.6

Table B.2 (continued)

mode	sym.	DF-cx @$\Omega_{\text{DF-cx}}$	IR	Raman	LDA @Ω_{LDA}	PBE @Ω_{exp}
34	B_g	718.1	–	725	723.6	715.8
35	B_g	760.1	–	–	763.7	773.1
36	A_g	760.9	–	765	764.9	776.2
37	A_g	772.2	–	–	778.3	784.4
38	B_u	773.2	780	–	779.0	771.4
39	B_g	775.4	–	786	781.4	789.7
40	A_u	787.1	–	–	793.0	786.9
41	A_u	791.6	–	–	795.2	799.5
42	B_u	793.3	810	–	797.2	802.1
43	A_u	839.5	841	–	845.0	838.8
44	B_u	843.2	–	–	849.8	844.0
45	A_g	878.6	–	878	885.8	885.6
46	B_g	893.0	–	–	900.4	901.0
47	A_g	926.8	–	–	930.2	931.4
48	B_g	930.8	–	933	934.6	935.4
49	B_g	942.1	–	–	949.9	947.7
50	A_g	947.2	–	953	955.6	950.4
51	B_u	957.0	955	–	965.1	961.5
52	A_u	957.0	–	–	966.6	961.2
53	A_u	975.2	970	–	984.1	978.7
54	A_g	981.0	–	980	989.3	986.5
55	B_u	981.5	–	–	991.0	985.2
56	B_g	984.7	–	–	993.1	989.7
57	B_u	1011.8	1008	–	1018.4	1021.6
57	B_u	1011.8	1008	–	1018.4	1021.6
58	A_u	1012.1	–	–	1018.7	1023.4
59	A_g	1018.6	–	–	1025.3	1025.9
60	B_g	1022.8	–	1021	1028.9	1029.3
61	A_u	1118.1	–	–	1122.9	1111.1
62	B_u	1118.1	1125	–	1123.1	1112.4
63	A_g	1138.6	–	–	1143.5	1125.8
64	B_g	1141.0	–	–	1146.3	1131.5
65	A_u	1145.6	1144	–	1150.3	1130.1
66	A_g	1148.8	–	1148	1152.8	1132.5
67	B_u	1152.5	–	–	1158.3	1139.8
68	B_g	1156.8	–	1168	1161.7	1141.2
69	A_u	1215.1	1209	–	1221.6	1225.1
70	B_u	1216.1	–	–	1222.0	1224.6

Table B.2 (continued)

mode	sym.	DF-cx @$\Omega_{\text{DF-cx}}$	IR	Raman	LDA @Ω_{LDA}	PBE @Ω_{exp}
71	B_g	1239.2	–	1240	1245.1	1233.3
72	A_g	1241.6	–	–	1247.9	1237.7
73	A_u	1259.4	–	–	1264.6	1256.6
74	B_u	1263.9	1265	–	1269.2	1260.2
75	A_u	1380.1	1361	–	1386.4	1413.3
76	B_u	1381.1	–	–	1386.8	1374.1
77	A_u	1382.7	–	–	1388.5	1372.4
78	B_u	1383.1	1389	–	1389.6	1414.7
79	B_g	1391.2	–	1380	1395.6	1420.8
80	A_g	1392.0	–	–	1396.3	1424.5
81	B_g	1448.3	–	1446	1454.0	1449.3
82	B_g	1451.6	–	–	1457.6	1457.0
83	A_g	1453.6	–	–	1459.6	1460.0
84	A_g	1456.1	–	1465	1461.8	1455.3
85	B_u	1508.5	1509	–	1515.7	1523.1
86	A_u	1511.1	–	–	1518.1	1526.0
87	A_g	1568.7	–	–	1575.2	1593.4
88	B_g	1571.4	–	1579	1577.9	1596.5
89	A_u	1591.2	–	–	1598.4	1610.9
90	B_u	1591.8	1595	–	1598.9	1611.2
91	B_g	1623.9	–	–	1630.4	1651.4
92	A_g	1624.2	–	1636	1630.7	1651.6
93	A_u	3057.1	3022	–	3101.0	3047.2
94	A_g	3057.4	–	2980	3101.7	3049.6
95	B_u	3058.2	–	–	3102.8	3048.9
96	B_g	3059.0	–	3058	3103.8	3051.0
97	A_u	3070.1	3029	–	3112.9	3060.5
98	B_u	3070.7	3029	–	3112.7	3059.9
99	A_g	3070.8	–	–	3113.6	3059.3
100	B_g	3071.1	–	–	3113.5	3057.9
101	A_u	3077.5	3056	–	3122.7	3066.8
102	B_u	3077.7	3056	–	3122.5	3065.5
103	B_g	3077.9	–	–	3121.9	3066.7
104	A_g	3078.2	–	–	3122.8	3067.0
105	B_u	3083.2	3076	–	3125.8	3074.4
106	A_g	3084.0	–	–	3129.1	3074.1
107	B_g	3084.3	–	–	3127.7	3074.4
108	A_u	3084.6	–	–	3127.4	3073.8

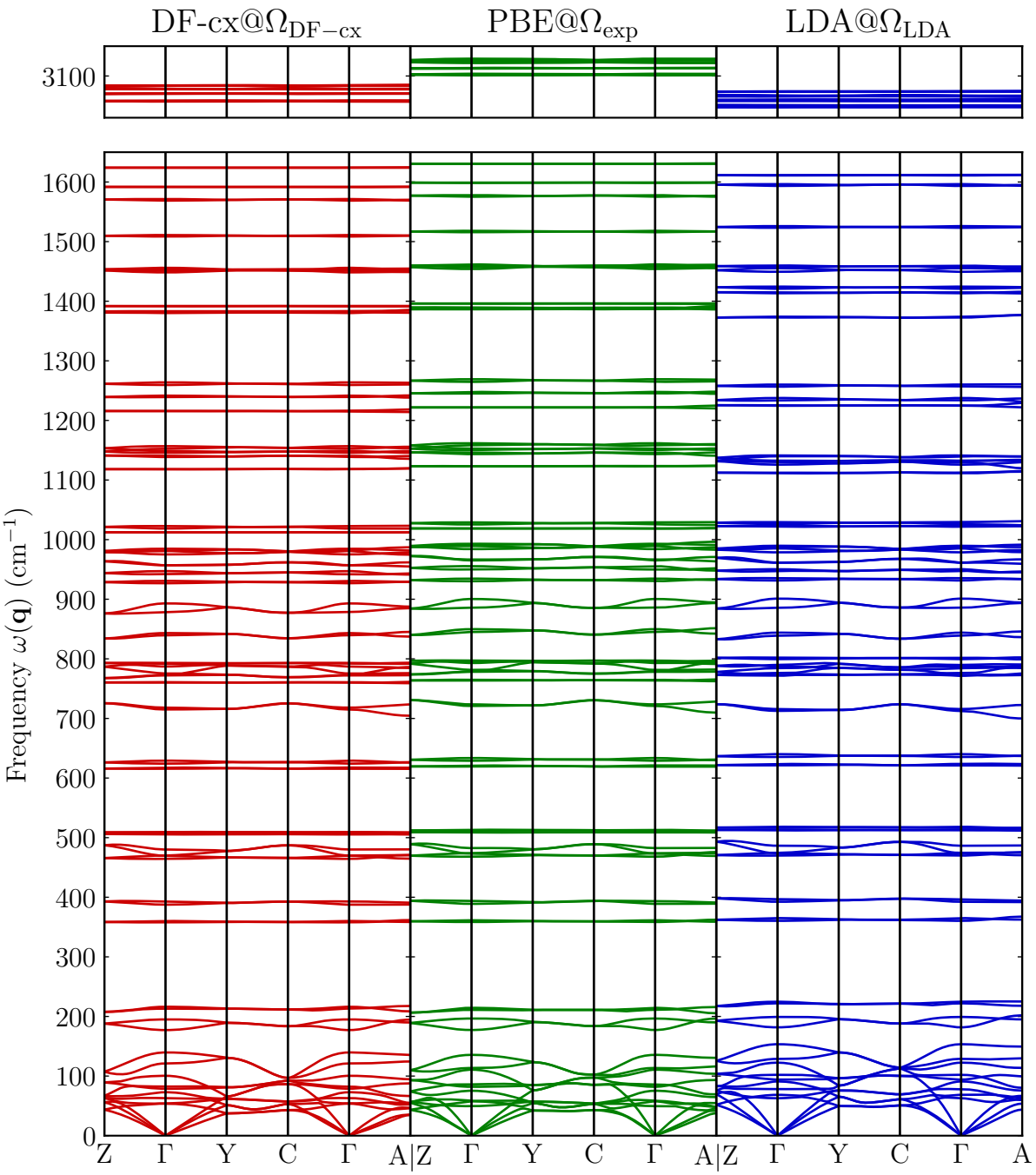

Figure B.1: Full phonon band structures of solid d0-naphthalene calculated with DF-cx, LDA, and PBE. The DF-cx and LDA unit cells are relaxed prior to the phonon calculation. PBE frequencies are calculated with experimental lattice parameters, and only the internal coordinates are relaxed.

Table B.3: Comparing frequencies calculated with DF-cx@$\Omega_{\text{DF-cx}}$ at Γ of fully deuterated naphthalene (ω_{D}) with protonated naphthalene (ω_{H}). The respective mode numbers highlight the reordering caused by the isotope change. All frequencies are in cm^{-1}.

n_{D}	ω_{D}	n_{H}	ω_{H}	$\omega_{\text{H}}/\omega_{\text{D}}$
4	50.2	4	53.7	1.070
5	52.5	5	54.2	1.032
6	59.0	6	63.1	1.069
7	70.7	7	72.9	1.031
8	74.2	8	78.7	1.061
9	77.2	9	82.4	1.067
10	97.4	10	100.5	1.032
11	112.2	11	121.2	1.080
12	128.8	12	139.7	1.084
13	163.0	13	177.1	1.087
14	179.6	14	195.1	1.086
15	193.7	15	213.1	1.100
16	195.8	16	216.3	1.105
17	326.1	17	357.8	1.097
18	328.4	18	360.2	1.097
19	342.4	19	387.5	1.132
20	347.3	20	393.1	1.132
21	397.7	22	469.7	1.181
22	406.8	24	480.1	1.180
23	411.5	21	464.4	1.129
24	417.9	23	470.0	1.125
25	488.3	27	508.8	1.042
26	488.9	26	506.4	1.036
27	489.7	25	505.2	1.032
28	491.5	28	509.6	1.037
29	537.9	33	715.0	1.329
30	540.2	34	718.1	1.329
31	540.5	31	624.1	1.155
32	547.6	32	629.2	1.149
33	589.2	29	615.5	1.045
34	591.8	30	617.7	1.044
35	622.5	38	773.2	1.242
36	630.5	40	787.1	1.248
37	643.5	37	772.2	1.200
38	649.0	39	775.4	1.195
39	654.0	43	839.5	1.284
40	655.7	44	843.2	1.286
41	688.4	35	760.1	1.104
42	689.9	36	760.9	1.103
43	732.8	41	791.6	1.080
44	734.0	42	793.3	1.081
45	753.3	49	942.1	1.251
46	755.2	50	947.2	1.254
47	761.0	45	878.6	1.155
48	765.7	56	984.7	1.286
49	787.6	51	957.0	1.215
50	788.0	52	957.0	1.215
51	798.8	53	975.2	1.221
52	801.2	55	981.5	1.225
53	818.2	63	1138.6	1.392
54	819.6	57	1011.8	1.235
55	820.3	58	1012.1	1.234
56	822.6	64	1141.0	1.387
57	824.8	66	1148.8	1.393
58	826.1	65	1145.6	1.387
59	829.7	68	1156.8	1.394
60	832.7	67	1152.5	1.384
61	834.4	54	981.0	1.176
62	835.3	46	893.0	1.069
63	854.1	59	1018.6	1.193
64	857.8	60	1022.8	1.192
65	869.1	61	1118.1	1.286
66	870.0	47	926.8	1.065
67	871.0	62	1118.1	1.284
68	872.0	48	930.8	1.067
69	1011.9	71	1239.2	1.225
70	1012.2	72	1241.6	1.227
71	1033.9	74	1263.9	1.222
72	1035.3	73	1259.4	1.216
73	1093.0	69	1215.1	1.112
74	1093.7	70	1216.1	1.112
75	1246.3	77	1382.7	1.109
76	1250.7	76	1381.1	1.104
77	1286.8	81	1448.3	1.125
78	1290.3	84	1456.1	1.128
79	1352.2	75	1380.1	1.021
80	1352.5	78	1383.1	1.023
81	1358.1	82	1451.6	1.069
82	1360.1	83	1453.6	1.069
83	1394.1	79	1391.2	0.998
84	1394.8	80	1392.0	0.998
85	1445.6	85	1508.5	1.044
86	1446.0	86	1511.1	1.045
87	1543.1	87	1568.7	1.017
88	1544.5	88	1571.4	1.017
89	1547.4	89	1591.2	1.028
90	1547.5	90	1591.8	1.029
91	1597.7	91	1623.9	1.016
92	1597.8	92	1624.2	1.017
93	2254.1	94	3057.4	1.356
94	2254.8	93	3057.1	1.356
95	2255.3	96	3059.0	1.356
96	2255.4	95	3058.2	1.356
97	2264.7	98	3070.7	1.356
98	2264.8	97	3070.1	1.356
99	2265.9	100	3071.1	1.355
100	2266.0	99	3070.8	1.355
101	2278.1	103	3077.9	1.351
102	2278.7	104	3078.2	1.351
103	2278.8	102	3077.7	1.351
104	2279.4	101	3077.5	1.350
105	2285.8	105	3083.2	1.349
106	2286.0	106	3084.0	1.349
107	2286.3	107	3084.3	1.349
108	2286.8	108	3084.6	1.349

Appendix C

Appendix for Electron-phonon coupling in naphthalene

C.1 Computational parameters

Ground state DFT calculations are performed with the ABINIT code [294] using norm-conserving pseudopotentials, and setting the plane waves kinetic energy cutoff to 45 Ha. We use the Perdew-Burke-Ernzerhof (PBE) functional in combination with the Grimme-D3 correction [121, 124] to account for London dispersion forces. To obtain the electronic ground state density, we sample the Brillouin zone on a Monkhorst-Pack **k**-grid of $2\times4\times2$. All electronic energies in this paper are given relative to the Fermi level.

The phonons and associated potential derivatives are calculated with DFPT, using a coarse Monkhorst-Pack **q**-grid of 4×6×4. This **q**-grid gives well converged phonon frequencies and displacements after interpolation of the dynamical matrix, as shown in our previous work [210]. The phonon potentials and self-energy are calculated explicitly with $6\times8\times6$ **q**-grid, and interpolated onto a $12\times14\times12$ **q**-grid, which converges the renormalization and broadening values within a few meV (see Fig. C.4 in the Appendix).

C.2 Lattice parameters

Table C.1: Lattice parameters used in this work. Experimental crystal structures are available at the Cambridge Structural Database [181]. The identifiers for the structures measured at 5 K and 295 K are NAPHTA31 and NAPHTA36, respectively, and published in association with [187]. (Lengths in Å, angles in degrees, volumes Ω in Å^3.)

	a	b	c	β	Ω
PBE-D3 (Ω_{DFT})	8.077	5.900	8.620	124.35	339.14
Exp. 5 K	8.080	5.933	8.632	124.65	340.41
Exp. 295 K ($\Omega_{295\mathrm{K}}$)	8.256	5.983	8.677	122.73	360.56

C.3 Phonon frequencies

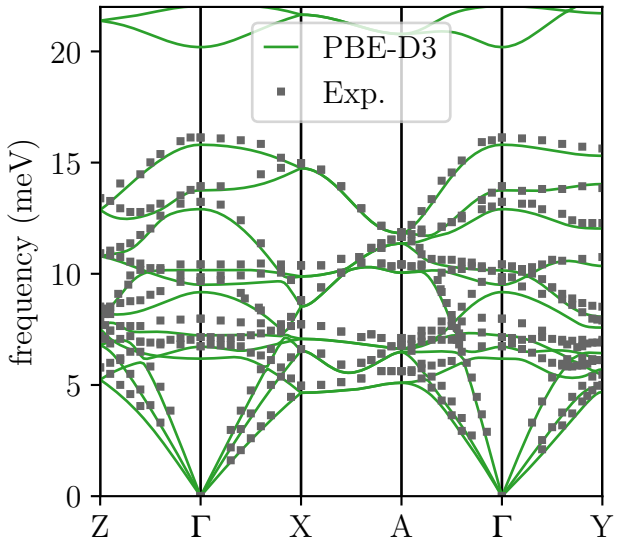

Figure C.1: Phonon band structure of intermolecular bands of perdeuterated naphthalene calculated with PBE-D3 at Ω_{DFT}. Experimental neutron scattering frequencies are taken from Ref. [219].

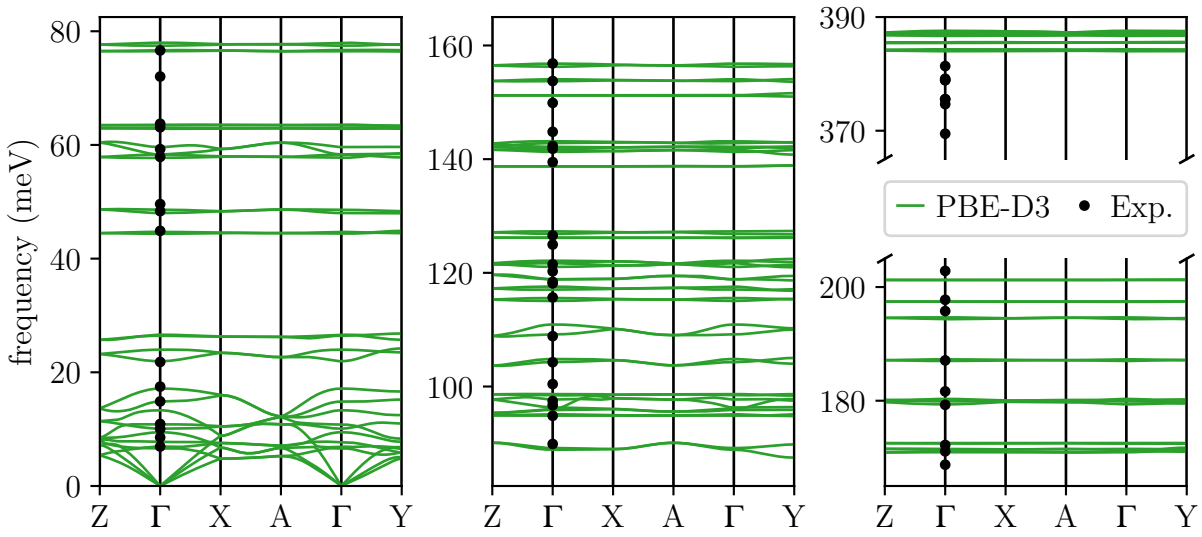

Figure C.2: Phonon band structure of naphthalene calculated with PBE-D3 at Ω_{DFT}. Experimental Raman and IR frequencies are taken from Ref. [216].

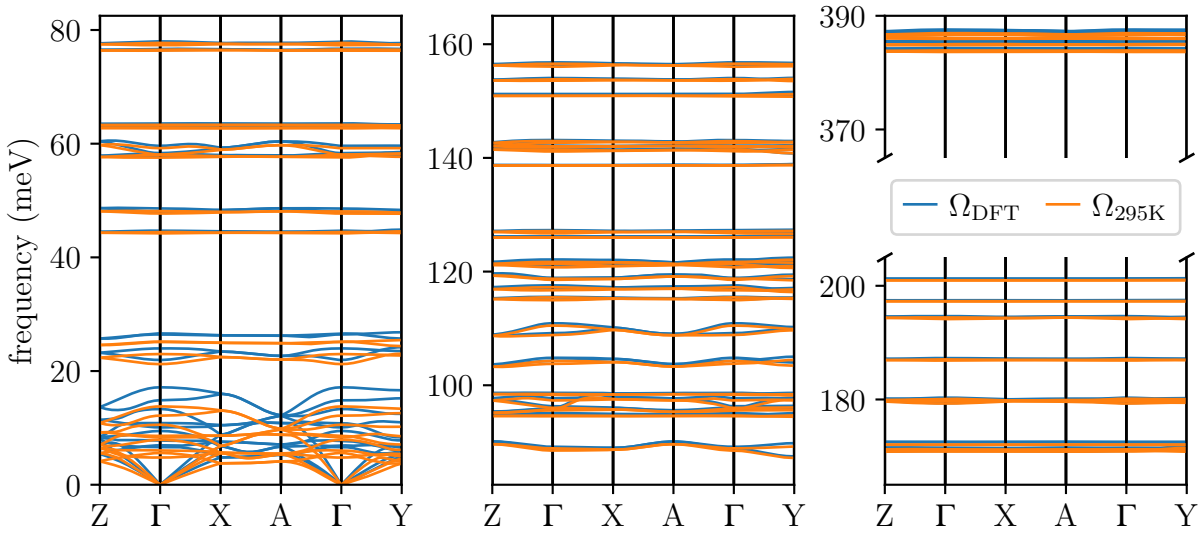

Figure C.3: Comparison of phonon band structures calculated with lattice parameters relaxed with PBE-D3 (Ω_{DFT}) and with fixed experimental room temperature lattice parameters ($\Omega_{295\mathrm{K}}$). Both calculations are done with PBE-D3. The lattice parameters mainly affect the soft intermolecular modes below 20 meV.

C.4 Convergence of self-energy

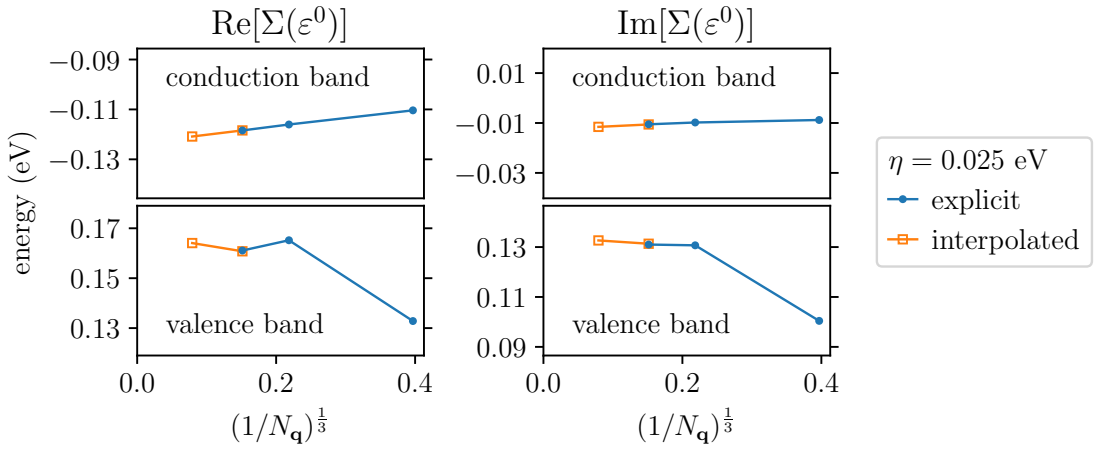

Figure C.4: Convergence w.r.t. **q**-grid spacing of the electron-phonon self-energy of the highest valence and lowest conduction band at Γ. The four **q** grids used from right to left are (2×4×2), (4×6×4), (6×8×6), and (12×14×12). Interpolated grids use square markers. Notable is the much smoother convergence of the conduction band, which is the absolute minimum at Γ. The valence band at Γ is 0.23 eV below the valence band maximum.

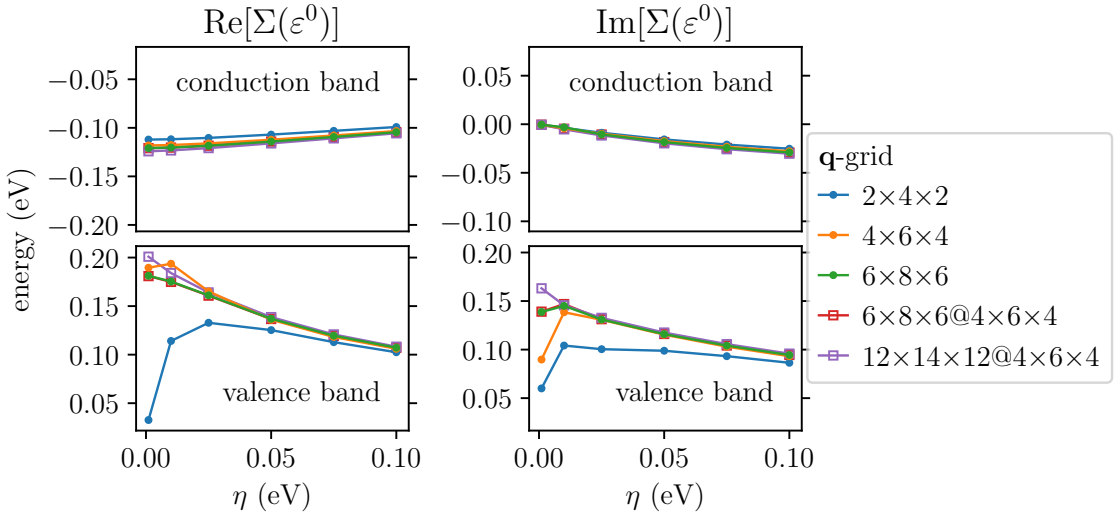

Figure C.5: Convergence w.r.t. the smearing value η of the electron-phonon self-energy of the highest valence and lowest conduction band at Γ. Interpolated grids use square markers and are labeled as "fine@coarse" to indicate the **q**-grids used. Notable is the much smoother convergence of the conduction band, which is the absolute minimum at Γ. The valence band at Γ is 0.23 eV below the valence band maximum.

C.5 Phonon decomposition of ZPR

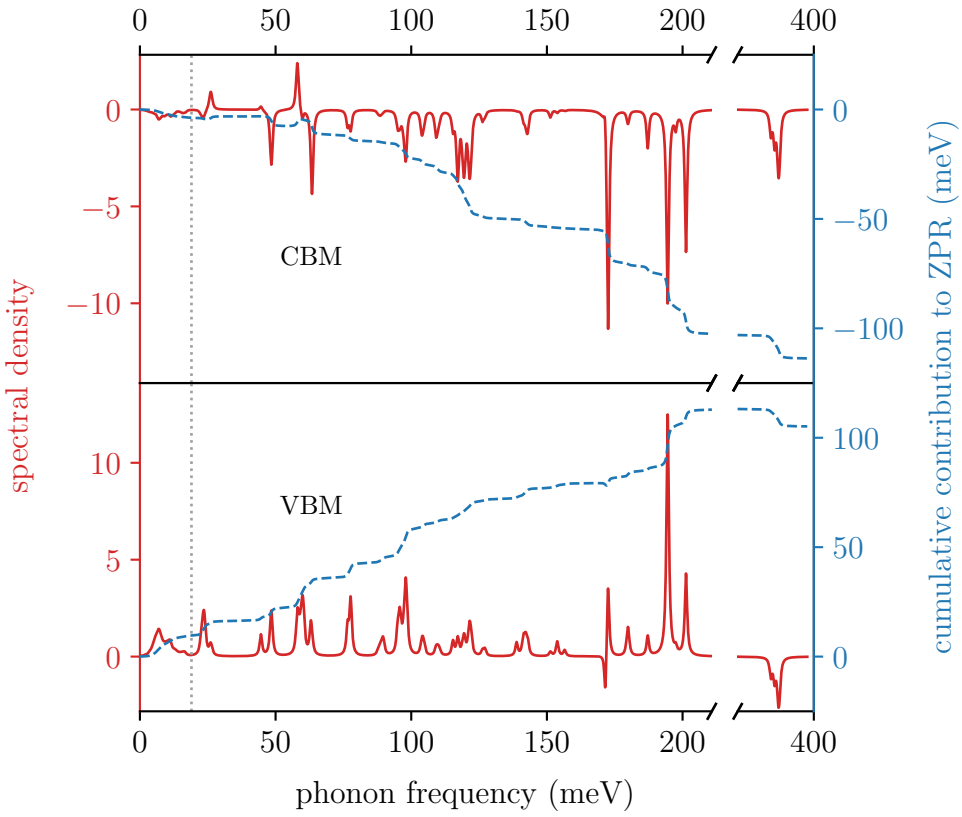

Figure C.6: Individual contributions of the phonon modes to the renormalization of the CBM plotted against frequency, with a Lorentzian smearing of 1 meV (red solid line). The grey dotted line at 19 meV indicates the separation of inter- from intramolecular modes. The blue dashed line shows the cumulative integral of the individual contributions.

For a more detailed analysis of the ZPR and temperature dependence we now look at the individual phonon contributions to the renormalization.

Reorganizing Eq. (2.27) we can write

$$\Sigma^{\mathrm{ep}}_{n\mathbf{k}}(\omega) = \sum_{\nu\mathbf{q}} \Sigma^{\mathrm{Fan}}_{n\mathbf{k},\nu\mathbf{q}}(\omega) + \Sigma^{\mathrm{DW}}_{n\mathbf{k},\nu\mathbf{q}} = \sum_{\nu\mathbf{q}} \Sigma^{\mathrm{ep}}_{n\mathbf{k},\nu\mathbf{q}}(\omega) \tag{C.1}$$

to obtain the self-energy for each phonon. For this analysis we calculate the self-energy on a $\mathbf{q}$-grid of 6×8×6 without interpolation. In Fig. C.6 we plot the real part of each $\Sigma^{\mathrm{ep}}_{n\mathbf{k},\nu\mathbf{q}}(\varepsilon^0_{n\mathbf{k}})$ at 0 K, i.e., each phonon's contribution to the ZPR. To account for finite sampling of reciprocal space we used a Lorentzian smearing of 1 meV.

The immediate take-away from this plot is that intramolecular phonon modes around 0.19 eV have the largest individual contributions, which is in agreement with previous stud-

ies [107, 109]. Overall however, the contribution as a function of phonon frequency is distributed relatively equally over the frequency range, especially for the VBM, as can be seen from the integral of the spectral density (blue line in Fig. C.6). The intermolecular modes situated below 19 meV (gray dashed line in Fig. C.6) contribute comparably little to the ZPR. Only these weakly coupling intermolecular and few soft intramolecular modes are populated at ambient temperatures, and contribute to the further reduction of the gap at finite temperatures.

C.6 k-independence of self-energy

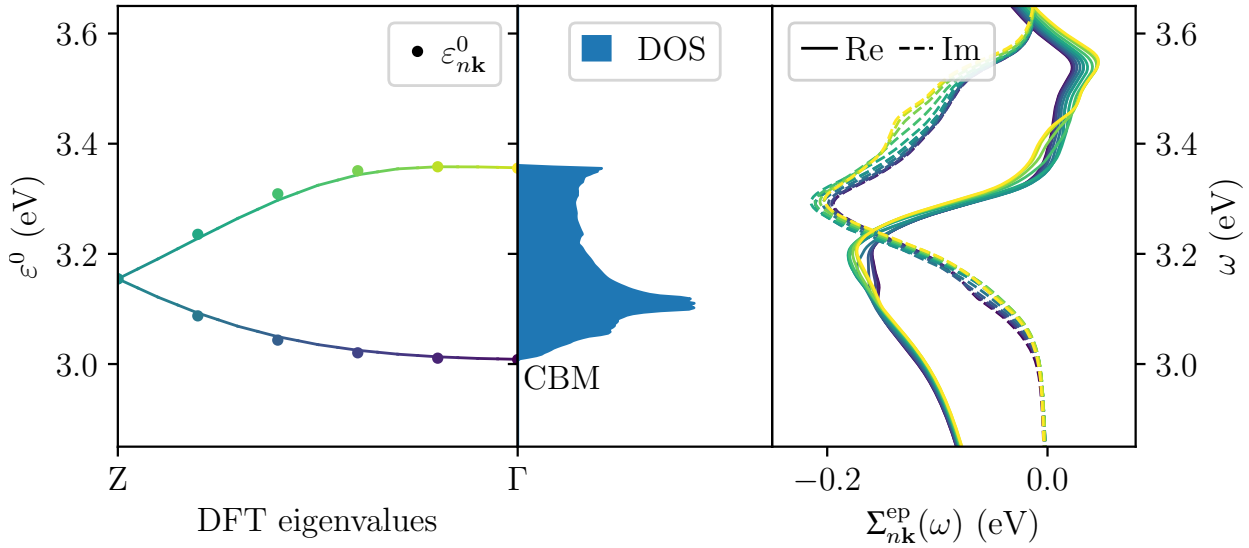

Figure C.7: (Left) Electronic band structure of the two lowest conduction bands along $\Gamma \to Z$ in the BZ. Each circle indicates an electronic state $n\mathbf{k}$ for which we explicitly calculated the self-energy $\Sigma^{\mathrm{ep}}_{n\mathbf{k}}$. (Middle) The density of states in the middle is plotted to highlight the correlation to the self-energy as discussed in the main text. (Right) The real and imaginary part of the electron-phonon self-energy of naphthalene for the states circled in the band structure plot on the left. The color of each self-energy matches the corresponding circle.

Here we test the **k**-independence approximation of the electron-phonon self-energy used in the main text. In Fig. C.7 we compare the frequency-dependent self-energy along the $\Gamma \to Z$ path, the direction of the largest dispersion for the conduction bands. Even along this relatively dispersive **k**-path, the real and imaginary parts of the self-energy show very little variation, validating the **k**-independence approximation. Additionally, we can also see that the frequency-dependent self-energy varies very little across the two bands. The combined **k**- and n-independence leads to the excellent agreement between the mobilities calculated with Eq. (5.2) and Eq. (5.5).

As laid out in the main text, the electronic states of Davydov pairs around the band gap (for example HOMO and HOMO-1, or LUMO and LUMO+1) interact only very weakly with their neighboring Davydov pairs, since they are energetically far enough apart. Since the resulting wave functions retain their gas-phase-like character throughout the Brillouin zone, the electron-phonon matrix elements become largely independent of $\mathbf{k}$. Additionally, this separation of bands is on the order of 0.3–0.4 eV, and thus at the upper end of our phonon spectrum. Hence, significant contributions to the self-energy, i.e., terms with small denominators in Eq. (2.25), will only come from scattering within these Davydov pairs. These two factors lead to the $\mathbf{k}$- and n-independence of the frequency-dependent self-energy. Since both these properties are very typical for organic crystals, we expect to see this approximation to hold for other systems as well.

C.7 Mobility as function of energy

Table C.2: Mobility values calculated with $\Omega_{295\mathrm{K}}$ at 300 K, comparing the values μ_{Boltz} obtained with the self-energy relaxation time approximation Eq. (5.2), with $\mu(\varepsilon)$ from Eq. (5.5), where we express the mobility as product of four independent functions of energy $\mu_\alpha^{\mathrm{e,h}} \propto \int \mathrm{d}\varepsilon\, D(\varepsilon) f'(\varepsilon) v_\alpha^2(\varepsilon) \tau(\varepsilon)$. Mobility values are given in $\mathrm{cm}^2/\mathrm{Vs}$.

	hole			electron		
	μ_a^{h}	μ_b^{h}	μ_{c*}^{h}	μ_a^{e}	μ_b^{e}	μ_{c*}^{e}
μ_{Boltz}	1.198	2.735	0.239	0.667	0.313	0.209
$\mu(\varepsilon)$	1.213	2.769	0.241	0.663	0.323	0.209
relative error	0.013	0.012	0.008	0.005	0.033	0.003

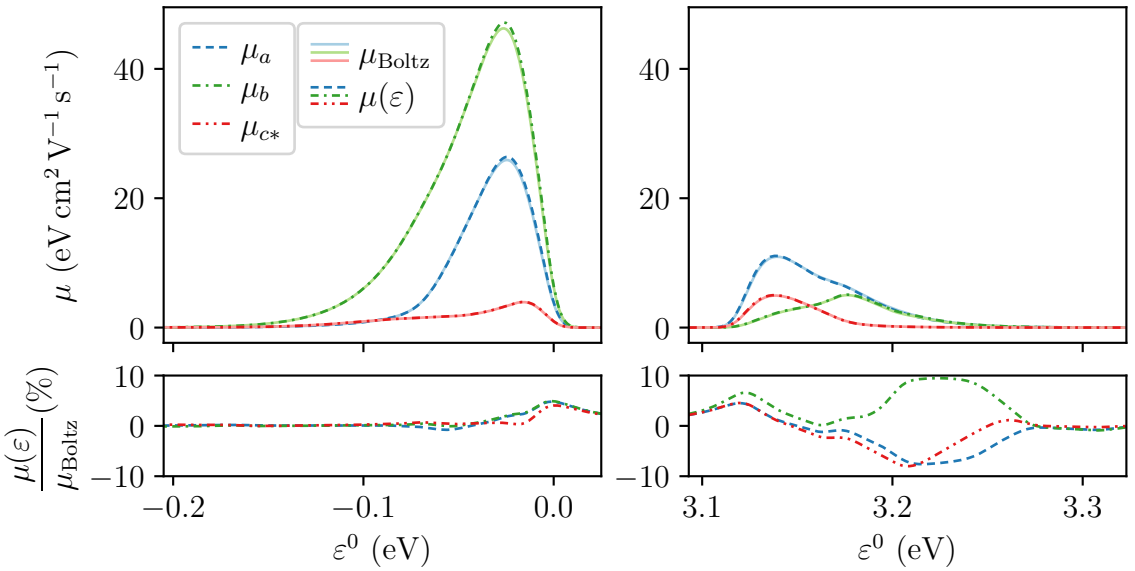

Figure C.8: Comparing the integrand of the mobility from the explicit summation over $n\mathbf{k}$ in the self-energy relaxation time approximation in Eq. (5.2) (μ_{Boltz}, solid transparent line) with the product of the four independent functions $D(\varepsilon)$, $f'(\varepsilon)$, $v_\alpha^2(\varepsilon)$, and $\tau(\varepsilon)$ from Eq. (5.5) ($\mu(\varepsilon)$, dashed lines).

C.8 Eigenvalue–self-consistent self-energy

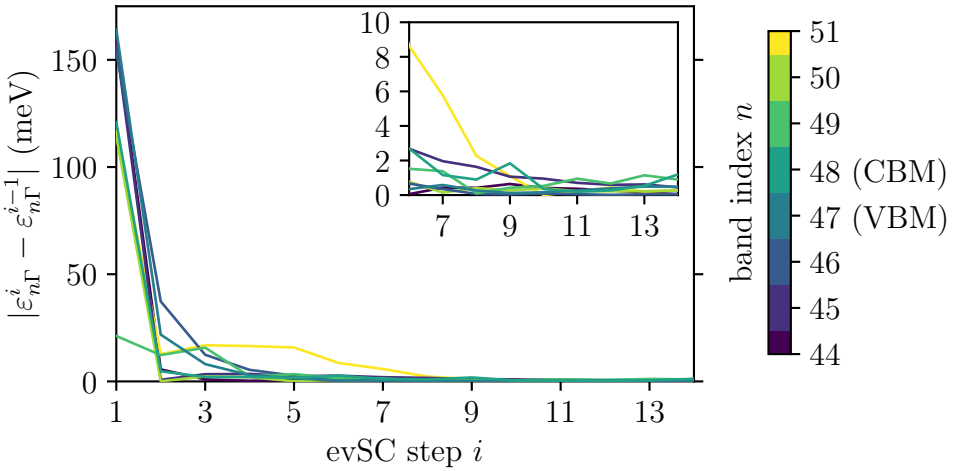

Figure C.9: Convergence of the electronic energies using the eigenvalue–self-consistent electron-phonon approach for bands around the band gap. The energy difference at the first step is equal to the renormalization obtained from the on-the-mass-shell approximation.

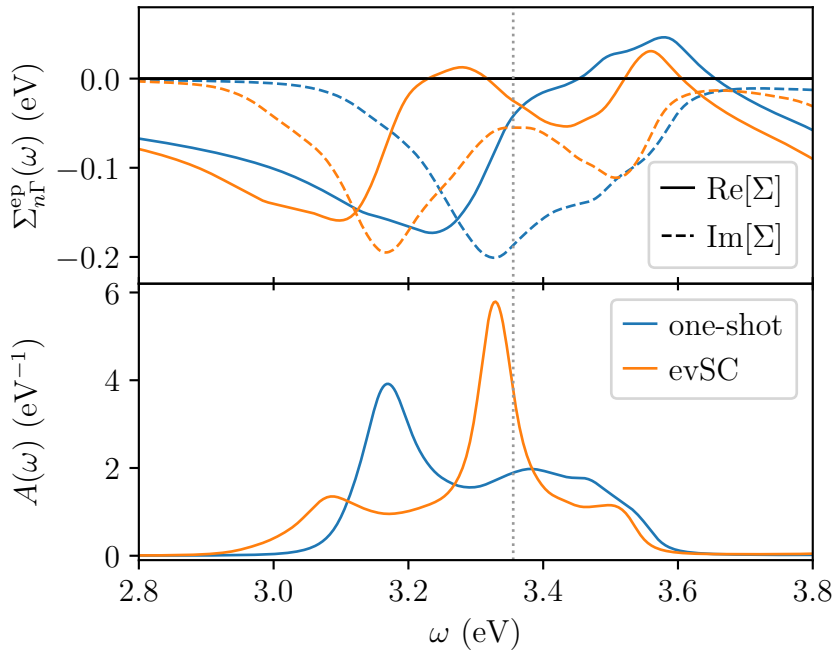

Figure C.10: Comparing the self-energy (top) and spectral function (bottom) of the one-shot with the eigenvalue–self-consistent (evSC) self-energy calculation for the second lowest conduction band (LUMO+1) at Γ. The energy of the DFT eigenvalue is marked with a gray dotted line.

In Fig. C.10 we compare the eigenvalue–self-consistent (evSC) with the one-shot approach by looking at the self-energy and spectral function of the second lowest conduction band (LUMO+1) at Γ. The changes in the self-energy and spectral function are quite significant. The main peaks of the real and imaginary parts are red-shifted by almost 0.2 eV, and a second peak develops at around 3.5 eV, above which the self-energy is mostly unchanged in comparison. This directly correlates with the renormalized density of states (DOS), where the lower energy states are renormalized by 0.1-0.2 eV, and the higher states remain unshifted.

This change in the self-energy has a large impact on the spectral function. Both the position of the main quasiparticle peak as well as the shape of the spectral function are altered. The renormalization of the main quasiparticle peak changes from −0.17 eV for the one-shot calculation to −0.03 eV for evSC. Furthermore, instead of the one broad phonon satellite in the one-shot calculation, the evSC spectral function shows two satellites, one at higher, and one at lower energies. The satellite at 3.1 eV actually becomes the main quasiparticle peak at other **k**-points. A similar transition can be clearly seen in Fig. 5.6 for the valence band. About half-way between Γ and Z, the quasiparticle peak shifts its weight from 0.3 eV to 0 eV. The same transition in the conduction bands is less visible because the bands are much more broadened out.

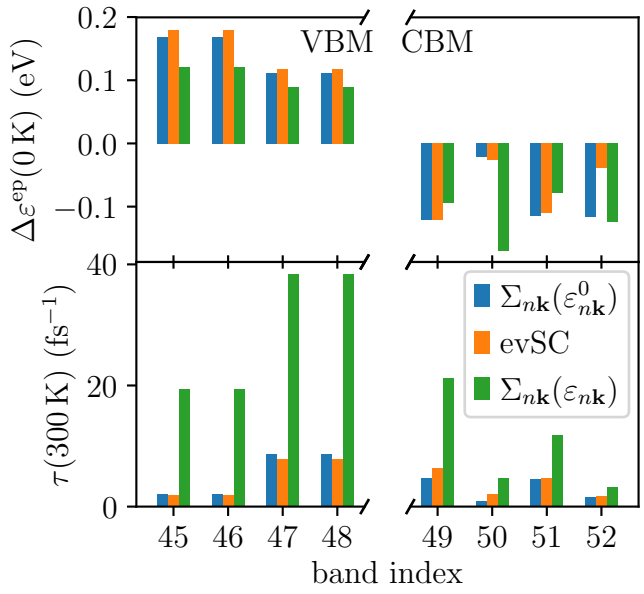

Figure C.11: Comparing the renormalizations and lifetimes of the evSC calculation with the on-the-mass-shell approximation ($\mathbf{\Sigma}(\varepsilon^0)$) and the quasiparticle solution ($\mathbf{\Sigma}(\varepsilon)$). Valence bands are at $\mathbf{k} = \mathrm{A}$, and conduction bands at Γ, coinciding with the VBM and CBM, respectively. The renormalizations (top) are calculated at 0 K using Ω_{DFT} lattice parameters. For the lifetimes (bottom) at 300 K we used $\Omega_{295\mathrm{K}}$ to account for lattice expansion. Overall, the on-the-mass-shell approximation agrees better with the evSC approach.

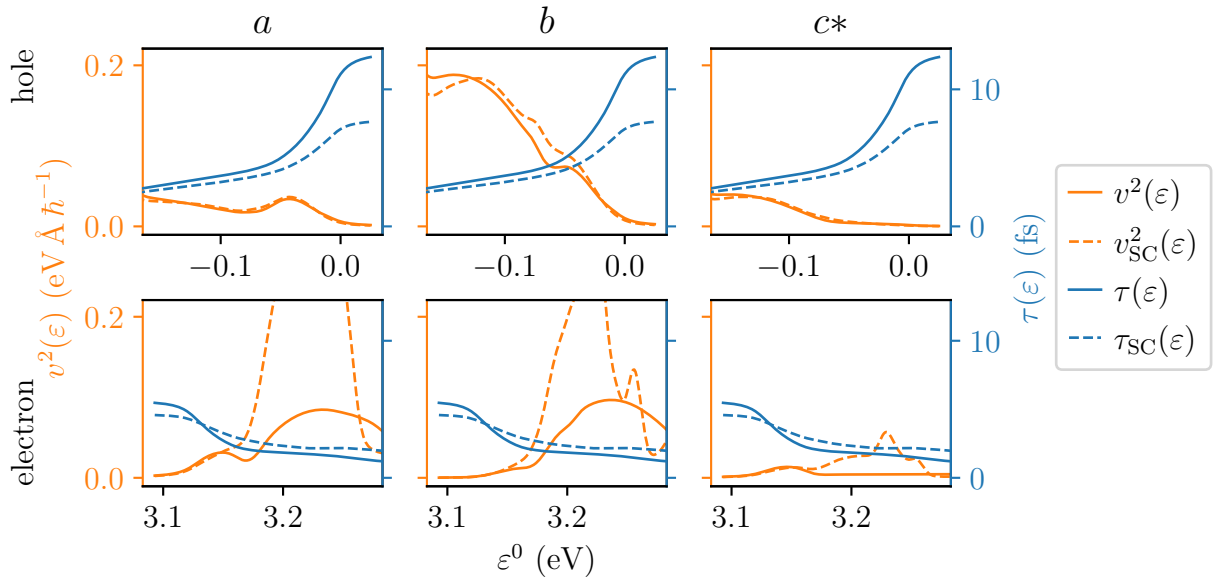

Figure C.12: Comparing the energy dependent velocities (Eq. (5.6)) and lifetimes (Eq. (5.7)) of the hole (top) and electron (bottom) carriers at 300 K (Ω_{DFT}) between the one-shot (solid) and evSC (dashed) calculations. The high electron velocities around 3.2 eV are an artifact caused by the breakdown of the quasiparticle picture near the band splitting.